

Proceedings of the Workshop of the Collaboration on Forward Calorimetry at ILC

22-23 September 2008
Vinča Institute of Nuclear Sciences
Belgrade, Serbia

Editor
Ivanka Božović – Jelisavčić

PROCEEDINGS OF THE WORKSHOP
OF THE COLLABORATION
ON FORWARD CALORIMETRY AT ILC

22-23 September 2008, Vinča Institute of Nuclear Sciences, Belgrade, Serbia

Publisher: **Vinča Institute of Nuclear Sciences
M. Petrovića Alasa 12-14
11001 Belgrade, Serbia**

For the publisher: **Jovan Nedeljković**

Editor: **Ivanka Božović – Jelisavčić**

ISBN: **978-86-7306-095-8**

**Ministry of Science and Technological Development of the Republic of
Serbia supported the publication of this book**

**Copyright © Vinča Institute of Nuclear Sciences – HEP Group Vinča
<http://www.vinca.rs/hep/>**

Belgrade, 2008

Preface

In the series of traditional meetings, the Workshop of the Collaboration on Forward Calorimetry at International Linear Collider took place at the Vinča Institute of Nuclear Sciences (INN VINČA), Belgrade, Serbia, from 22nd to 23th September 2008. The Workshop was organized by the HEP group at INN VINČA with the support from the Ministry of Science and Technological Development of the Republic of Serbia.

This is an international workshop of the ILC community developing the physics case and detector designs for the forward region of the future International Linear Collider (FCAL): 37 physicists from 10 countries participated in this workshop. We wish to thank the representatives of external collaborations, CLIC, SuperBelle and ATLAS for their participation.

Lying before you are the Proceedings of the FCAL Workshop, which has been published in partial fulfillment of contract no. 451-03-00540/2008-02 with the Ministry of Science and Technological Development of the Republic of Serbia. You will find here 24 papers out of 25 which have been presented at the Workshop, either in person at the conference venue, or at a distance, by means of electronic teleconferencing devices. The papers are divided into groups in accord with the Workshop schedule. These Proceedings are also available online, at http://www.vinca.rs/hep/pub/FCAL_Belgrade.pdf.

It gives us pleasure to thank the Ministry of Science and Technological Development of the Republic of Serbia for financing this workshop, the Director General of INN VINČA for logistic help during the Workshop, and the Publishing Advisory Board of the Scientific Council of INN VINČA for their help with the publication of these Proceedings.

We would also like to thank all the authors who contributed to these Proceedings, as well as all of the Workshop attendants for their enthusiasm and contributions to a successful meeting.

On behalf of the Organizing Committee,
Ivanka Božović – Jelisavčić

List of Committee Members

International Advisory Committee

Aharon Levy, Tel Aviv University, Israel
Wolfgang Lohmann, DESY, Germany
Klaus Moenig, DESY, Germany
Ivanka Božović - Jelisavčić, INN Vinča, Serbia

Local Organizing Committee:

Ivanka Božović - Jelisavčić, INN Vinča, Serbia
Ivan Smiljanić, INN Vinča, Serbia
Mila Pandurović, INN Vinča, Serbia
Mihajlo Mudrinić, INN Vinča, Serbia
Veljko Dmitrašinović, INN Vinča, Serbia
Stevan Jokić, INN Vinča, Serbia
Snežana Milosavljević (secretary), INN Vinča, Serbia

Table of Contents

Preface	III
List of Committee Members	IV
Introduction	2
Wolfgang Lohmann, INTRODUCTION TO THE WORKSHOP ON FORWARD CALORIMETRY AT THE ILC	3
Invited talks	7
Klaus Mönig, WITH ACCELERATORS TO THE PLAN OF THE UNIVERSE - THE FUTURE OF TERASCALE PHYSICS	8
Veljko Dmitrašinović, A VARIATIONAL ESTIMATE OF THE HIGGS MASS	14
Forward region at ILC and other experiments	18
Wolfgang Lange, FAST BEAM CONDITIONS MONITORING (BCM1F) FOR CMS	19
Hans Henschel, BEAMCAL READOUT SYSTEM REQUIREMENTS	24
Leszek Zawiejski, LASER ALIGNMENT SYSTEM FOR LUMINOSITY DETECTOR LUMICAL	28
Lucie Linssen, CLIC FORWARD REGION STUDIES STATUS REPORT	32
Ljiljana Simić, LUMINOSITY MEASUREMENT AND FORWARD PHYSICS AT ATLAS	36
Peter Križan, VERY FORWARD REGION IN BELLE: PHYSICS IMPACT AND OPPORTUNITIES	40
Luminosity Calorimeter	44
Wojciech Wierba, LUMICAL DESIGN OVER VIEW	45
Bogdan Pawlik, ASPECTS OF LUMICAL INTEGRATION WITH ILD	50
Ivan Smiljanić, TOWARDS A FINAL SELECTION FOR LUMINOSITY MEASUREMENT	52
Iftach Sadeh, INFLUENCE OF THE SHAPE OF THE BEAMPIPE ON THE LUMINOSITY MEASUREMENT AT THE ILC	58
Wojciech Wierba, SILICON SENSORS FOR LUMICAL	64
Krzysztof Swientek, STATUS OF LUMICAL READOUT ELECTRONICS	67
Beam Calorimeter and pair monitoring	71
Alexandr Ignatenko, DEVELOPMENT OF CHARGED PARTICLE DETECTORS ON THE BASE OF MONOCRYSTALLINE DIAMOND OF MINSK PRODUCTION	72
Alexandr Ignatenko, CHARACTERIZATION OF GaAs Cr DOPED SENSOR SAMPLES	77
Sergej Schuwalow, SEARCH FOR NEW BEAMCAL SENSOR MATERIALS	81
Sergej Schuwalow, BEAMCAL MECHANICS	85
Yosuke Takubo, DEVELOPMENT OF PAIR MONITOR	88
Kazutoshi Ito, PERFORMANCE STUDY OF PAIR MONITOR	91
Yutaro Sato, STUDY OF PAIR-MONITOR FOR ILD	95
Angel Abusleme, BEAMCAL FRONT-END ELECTRONICS: DESIGN AND SIMULATION	99
Conclusion	105
Wolfgang Lohmann, CONCLUSIONS OF THE WORKSHOP ON FORWARD CALORIMETRY AT THE ILC	106

Introduction

INTRODUCTION TO THE WORKSHOP ON FORWARD CALORIMETRY AT THE ILC

By

Wolfgang LOHMANN

DESY, Platanenalle 6, D-15738 Zeuthen

THE ADVENT OF LHC PHYSICS

To open a workshop of particle physicists these days is impossible without a tribute to LHC. We all were aware of the start of the LHC machine September 11. First beams were circulating in opposite directions, and in the detectors signals from beam halo were recorded, showing their readiness for physics data taking. LHC is a discovery machine. It will allow us to scan a new range in energy for expected particles, like the Higgs boson, and, even more interesting, for unexpected phenomena.

THE ILC PROJECT

The ILC will be a machine complementary to LHC. A well known initial state, a tunable energy and clear and fully reconstructed events will allow for exploring in detail e.g. electroweak symmetry breaking and the possibly reach world of new phenomena and particles. In the first stage ILC will reach a centre-of-mass energy of 500 GeV, and an upgrade to 1 TeV is foreseen.

A “Global Design Effort”, GDE, was established several years ago for the ILC project. Its mission is to work out a design of the ILC, including performance benchmarks, costing, site evaluation, industrialization for major components, and to coordinate the worldwide prioritized R&D for the machine. Under the leadership of a director, regional directors, and structured in several task and R&D groups, nearly 500 physicists worldwide are included. In 2007 the Reference Design Report for the ILC and detector concepts, RDR, was released by the GDE.

The R&D effort in the near future is subdivided in two stages: Up to 2010 prioritized R&D will be pursued in critical areas, first of all to reduce risks. In a second phase the technical design, including costs, will be completed with the goal of an Engineering Design Report (EDR) ready in 2012.

Detector R&D is performed world wide on a similar time-line. The International Linear Collider Steering Committee, ILCSC, appointed a research director for guiding the global detector R&D effort and devising procedures that will result in contrasting and complementary detector designs.

The latter will be based on “Letter of Intends”, LoI, worked out and submitted by groups of physicists with a certain level of commitment. The LoI must comprise a description of the detector, the list of participants and an explanation of the resources, simulation studies to demonstrate the physics performance, the critical R&D areas and the plan for the completion of the technical design. The LoIs for the detectors must be submitted before March 31, 2009.

A review committee, IDAG, will then critically review the LoIs, validate the detector designs and give guidance for an advanced development.

THE FCAL COLLABORATION

The goal of the FCAL collaboration is to design the very forward sub-detectors of an ILC detector and to develop the technologies for their construction. Currently, two calorimeters are foreseen in the very forward region near the interaction point - LumiCal for the precise measurement of the luminosity and BeamCal for the fast estimate of the luminosity and to improve the hermeticity of the detector. A third calorimeter, GamCal, about 100 m downstream of the detector, will assist beam-tuning. Also for beam-tuning a pair monitor is foreseen, positioned just in front of BeamCal.

LumiCal and BeamCal face several challenges. BeamCal is positioned just outside the beam-pipe. A large amount of low energy electron-positron pairs originating from beamstrahlung will deposit their energy in BeamCal. These depositions, useful for a bunch-by-bunch luminosity estimate, may lead, however, to a radiation dose of several MGy per year at lower polar angles. Hence radiation hard sensors are needed to instrument BeamCal. LumiCal will be used to measure precisely the luminosity, with an accuracy of better than 10^{-3} , and is hence a precision device. The requirements on the mechanical precision, stability and position control are a challenge.

Both calorimeters must be compact and finely segmented. A small Moliere radius is of invaluable importance. It ensures an excellent electron veto capability for BeamCal even at small polar angles,

being essential to suppress background in new particle searches where the signatures are large missing energy and momentum. In LumiCal the precise reconstruction of electron and positron showers of the Bhabha process is facilitated and background processes will be rejected efficiently.

THE CURRENT STATUS OF THE VERY FORWARD REGION R&D

A sketch of the very forward region of the ILD detector, as an example, is shown in Figure 1. LumiCal and BeamCal are cylindrical electromagnetic calorimeters, centered around the outgoing beam. LumiCal is positioned inside and aligned with the forward electromagnetic calorimeter. BeamCal is placed just in front of the final focus quadrupole.

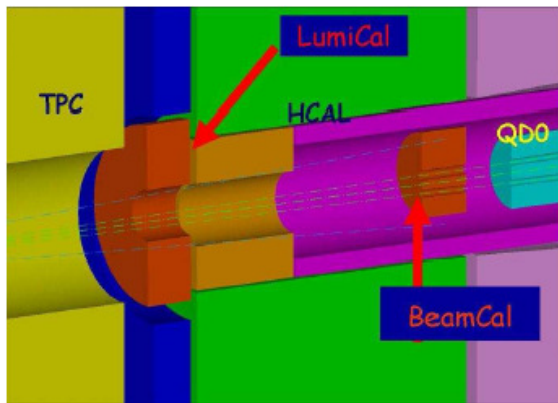


Figure 1. The very forward region of the ILD detector. LumiCal and BeamCal are positioned aligned with the electromagnetic calorimeter ECAL and just in front of the final focus quadrupole QD0, respectively. LumiCal, BeamCal and QD0 are carried by the support tube. TPC denotes the central track chamber and HCAL the hadron calorimeter.

LUMICAL

The gauge process for the measurement of the luminosity is Bhabha scattering, $e^+e^- \rightarrow e^+e^- (\gamma)$. Monte Carlo studies have shown that a compact silicon-tungsten sandwich calorimeter is a proper technology for LumiCal. A small Moliere radius and finely radially segmented silicon pad sensors ensure an efficient selection of Bhabha events. The luminosity, \mathcal{L} , is obtained from

$$\mathcal{L} = N/\sigma \quad (1)$$

where N is the number of Bhabha events counted in certain polar angle range and σ is the Bhabha scattering cross section in the same angular range calculated from theory. The most critical quantity to control when counting Bhabha scattering events is the inner acceptance radius of the calorimeter, defined as the lower cut in the polar angle, as

illustrated in Figure 2. Since the angular distribution is very steep, a small bias in the polar angle acceptance will shift the measured value of the luminosity. From Monte Carlo studies of the given design a tolerance of a few μm is estimated for the inner acceptance radius. Since there is bremsstrahlung radiation in Bhabha scattering, also cuts on the shower energy will be applied. The criteria to define good Bhabha events will define requirements on the energy resolution and, more challenging, on the control of the energy scale of the calorimeter.

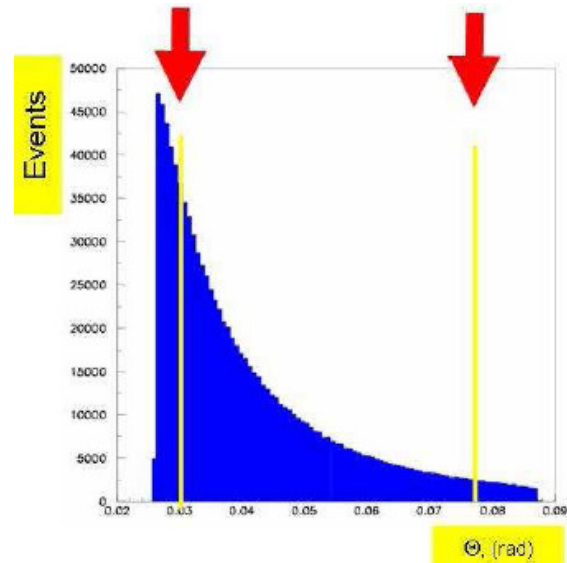


Figure 2. The polar angle distribution of Bhabha events in the LumiCal. The arrows indicate the acceptance region in the polar angle θ used for the luminosity determination.

Following the design optimization of sensors for LumiCal, we made substantial progress in the preparation of prototypes. Recently an agreement with Hamamatsu was obtained for the production of the first batch of sensor. These sensors will be available at the end of the year. At the first stage these sensors will be studied in the laboratories. In a later stage, the sensors will be instrumented with Front-End (FE) electronics for investigations in the test-beam.

Impressive progress was made in the design of the FE Asics. Last year we obtained the first prototypes of the analog and ADC Asics. The performance of the FE Asics is under study. The ADCs needed improvements, and a second submission is done just recently.

Provided, the performances of the sensors and the Asics will be satisfactory, tests of a full system in the beam will be the next major step.

BEAMCAL

The major challenge of BeamCal is the detection of high energy electrons on top of the

wider spread background from a large amount of e^+e^- pairs from beamstrahlung. The distribution of these depositions from one bunch crossing on the front face of BeamCal is shown in Figure 3. Superimposed is the local deposition of one high energy electron (the red spot at the bottom). Using an appropriate background subtraction and a shower finding algorithm which takes into account the longitudinal shower profile, the deposition of the high energy electron can be detected with high efficiency and modest energy resolution.

The amount of energy and the shape of energy distribution on the front face of BeamCal depends strongly on the beam parameters and can be used for a fast luminosity estimate and beam parameter determination on a bunch-by-bunch basis. Hence, these are valuable information for a fast feedback system to optimize the luminosity.

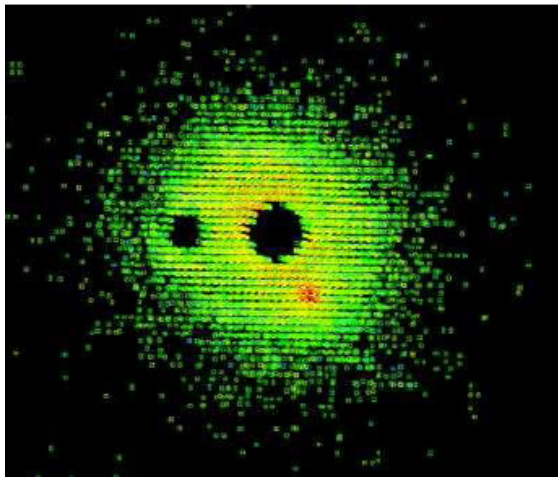


Figure 3. The distribution of depositions of beamstrahlung pairs created in one bunch crossing on the front face of BeamCal (in yellow and green). Superimposed is the deposition of a single high energy electron (red spot in the bottom part). The black hole in the center corresponds to the outgoing beam-pipe, the black hole on the left to the incoming one.

The challenges for BeamCal are radiation hard sensors, surviving up to 10 MGy of dose per year. So far we have studied polycrystalline CVD diamond sensors of 1 cm² size, and larger sectors of GaAs pad sensors. GaAs sensors are found to tolerate nearly 2 MGy. Polycrystalline CVD diamond sensors are irradiated up to 7 MGy and are still operational. Also single crystal CVD diamond sensors are studied. Large area CVD diamond sensors are extremely expensive, and may be used only at the innermost part of BeamCal. At larger radii GaAs sensors seem to be a reasonable option. These studies will be continued in future for a better understanding of the damage mechanisms in these sensor materials.

The FE Asic development for BeamCal, including a fast analog summation for the beam

feedback system and an on-chip digital memory for readout in between two bunch trains is in good shape, and we may expect first prototypes next year.

THE PAIR MONITOR

The pair monitor consists of one layer of silicon pixel sensors just in front of BeamCal, as shown in Figure 4, and measures the distribution of the number of beamstrahlung pairs. Monte Carlo simulation has shown that the pair monitor will give essential additional information for beam tuning. In addition, averaging over several bunch crossings, e.g. the beam sizes might be reconstructed with per cent precision.

A special Asic is developed for the pair monitor and prototypes are under study. In a later stage, the pixel sensor and the Asic are foreseen to be embedded in the same wafer.

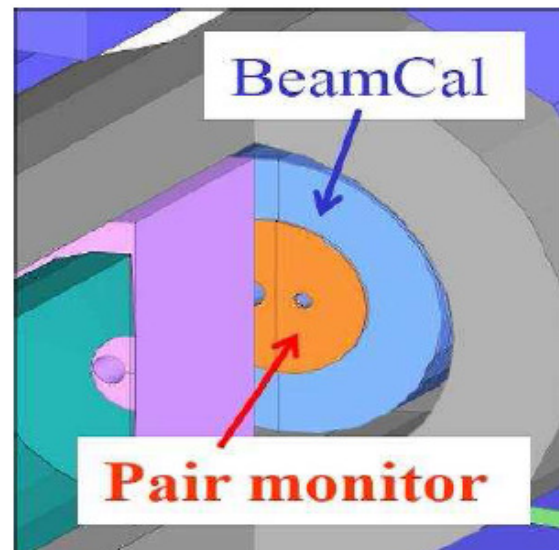


Figure 4: The pair monitor installed just in front of BeamCal.

GAMCAL

GamCal is supposed to exploit the photons from beamstrahlung for fast beam diagnostics. Near the nominal luminosity the energy of beamstrahlung photons supplements the data from BeamCal and Pair Monitor improving the precision of beam parameter measurements and reducing substantially the correlations between several parameters. At low luminosity the amount of depositions on BeamCal will drop dramatically, however GamCal will still give robust information for beam tuning.

To measure the beamstrahlung spectrum a small fraction of photons will be converted by a thin diamond foil or a gas-jet target about 100 m downstream of the interaction point. The created

electrons or positrons will be measured by an electromagnetic calorimeter as sketched in Figure 5. For the time being we have a rough design of GamCal. More detailed Monte Carlo studies are necessary to fully understand the potential of GamCal for beam tuning and beam parameter determination.

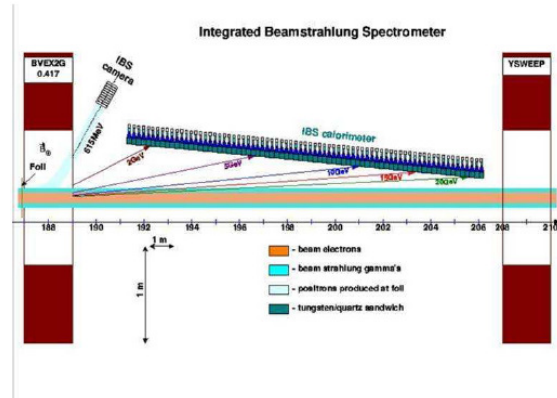


Figure 5. The GamCal consists of electromagnetic calorimeter modules (denotes as IBS) to measure electrons from photon conversions. The calorimeter is placed just downstream of a dipole magnet allowing the measure also the energy spectrum of the electrons.

CLIC AND sBELLE

At CERN R&D for the “Compact Linear Collider”, CLIC, is pursued. The centre-of-mass energy range may reach 3 TeV, making this machine of particular interest when new physics phenomena would be discovered at LHC in the energy range of 1 TeV and above. The schedule foresees a CDR both for the machine and the detector at 2010 and a TDR in 2014. First beams might be available in 2023. ILC-CLIC working groups for several fields in machine R&D and also for detector R&D are established, and FCAL might be an interesting field for joint R&D effort together with people from CLIC.

SuperBelle is an upgrade project for Belle at KEK. The luminosity will be enhanced to $2 \cdot 10^{35}$ in the first phase in 2013, and to $8 \cdot 10^{35}$ in a later stage. To improve the hermeticity of the sBelle detector silicon pad disks similar to the ones developed for LumiCal are foreseen to instrument the very forward regions. To obtain commitments here would be a nice opportunity to apply the silicon pad detectors under development for LumiCal in an experiment in an intermediate-term timescale.

PRIORITY R&D TOPICS FOR FCAL

The current research work covers several fields of high priority for the preparation of the LoI and at a longer timescale, for the EDR. The major topics I see are:

- Refine and complete the simulation studies for all calorimeters and the pair monitor.

The results obtained here will be essential input for the LoI.

- Development of radiation hard and precise sensors for BeamCal and LumiCal, respectively. The feasibility of BeamCal depends essentially on large area radiation hard sensors.
- Prototyping of a laser position monitoring system for LumiCal. In particular the control of the inner acceptance radius with μm accuracy is a challenge and must be demonstrated.
- Development and prototyping of FE Asics, both for the calorimeters and the pair monitor. There are challenging requirements on the readout speed, the dynamic range, the buffering depth and the power dissipation.
- Development of fast data transmission units.
- Design and prototyping of elements for the fast feedback using very forward detectors.
- Consideration of the requirement and chances of new projects like CLIC and sBelle.

Let's use the time of this workshop to discuss these items, to make changes if appropriate, and to find the best ways how to proceed.

Invited Talks

WITH ACCELERATORS TO THE PLAN OF THE UNIVERSE - THE FUTURE OF TERASCALE PHYSICS

By

Klaus MÖNIG

DESY, Platanenalle 6, D-15738 Zeuthen

Although the standard models of particle physics and cosmology describe the data with a very good precision there are still many unsolved problems requiring new physics. The next generation of colliders, the LHC and a possible linear collider like the ILC have the potential to answer many of the open questions.

INTRODUCTION

The Standard Model of particle physics describes the interactions between fermions by the interchange of gauge bosons. Strong and electroweak interactions are described by the gauge group $SU(3) \times SU(2) \times U(1)$, where the $SU(3)$ from strong interactions acts only on quarks. The $SU(2)$ acts only on left handed particles and the $SU(2) \times U(1)$ mix to generate the weak force and electromagnetism. In the unbroken theory all particles are massless and the Higgs mechanism is needed to give mass to the electroweak gauge bosons and the fermions. The Higgs mechanism requires a neutral scalar particle, the Higgs boson, which isn't found yet.

In the Standard Model of cosmology, the universe originates from a big bang about 15 billion years ago and expands and cools down since then. However, cosmic observations show that the universe consists only to 4% of ordinary matter, the rest is dark matter (22%) and dark energy (74%), the physical nature of which is unknown.

The combination of these two models describes a vast amount of data, although a couple of serious problems remain:

- The Higgs isn't found yet. Direct searches and fits to precision data suggest a range of $115 \text{ GeV} < m_H < 200 \text{ GeV}$ [1]
- The Standard Model requires a light Higgs, ($O(100 \text{ GeV})$), radiative corrections however make the Higgs heavy ($O(m_{pl}) \sim 10^{19} \text{ GeV}$). This problem is known as the hierarchy problem.
- The Standard Model has about 20 free parameters

- CP violation, which is needed to explain the matter-antimatter asymmetry exists in the Standard Model, however it turns out not to be sufficient.
- The physical nature of the dark matter and dark energy is unknown.
- There is no explanation for the size of the fermion masses.

For the most of these problems solutions can be expected if the physics at the TeV scale is known. For this reason the LHC [2], a proton-proton collider with a centre of mass energy of 14 TeV, has been built and will start data taking soon. It is a general consensus that the LHC should be complemented by an e^+e^- linear collider at the TeV scale like the ILC [3].

LHC AND ILC

Protons are heavy and thus basically don't radiate synchrotron radiation. For this reason they can be accelerated to very high energy in synchrotrons, limited only by the achievable magnetic field in the dipoles. On the other hand they are composite particles consisting of quarks and gluons so that the typical energy of the colliding partons is much lower than the proton energy and for a given event the underlying reaction at the parton level is unknown. The proton remnants disappear in the beampipe so that the event kinematics cannot be used for reconstruction. In addition to that quarks and gluons have strong interactions giving rise to a huge QCD background which can hide interesting processes. In this sense hadron colliders are generally considered as discovery machines.

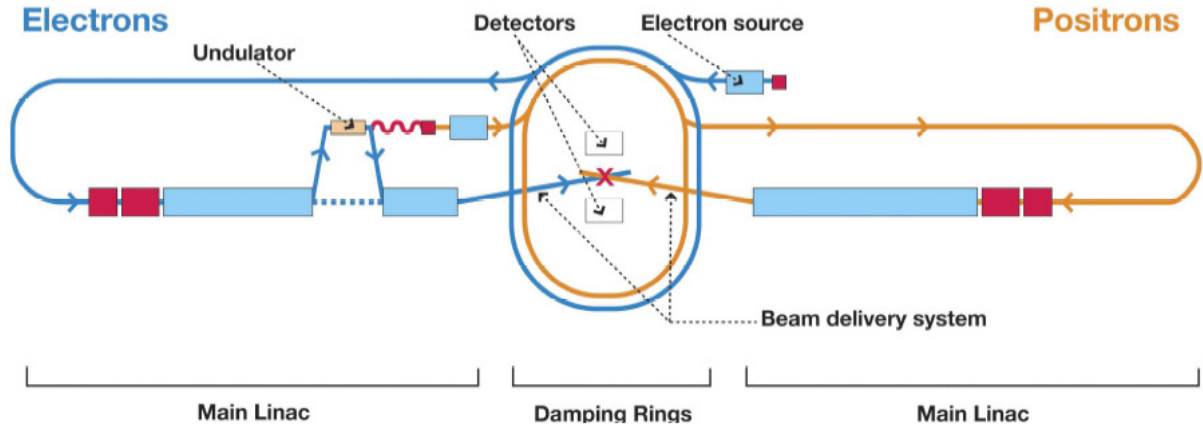


Figure 1. Principle layout of the ILC.

Contrary to protons the energy of electrons in synchrotrons is limited by synchrotron radiation which scales like $E_{sync} \propto E_b^4/r$. LEP reached beam energy of 100GeV in a 26 km ring which is definitely the maximum which is achievable at reasonable cost. Higher energies can only be reached in a linear collider with a high accelerating field. However electrons are point-like particles so that the full collision energy goes into the interaction and the initial state, possibly including polarization, is known. Also energy-momentum constraints can be used in the reconstruction. Since electrons don't have strong interactions the backgrounds in lepton colliders are generally low and all processes can be reconstructed. Lepton colliders are thus considered to be precision machines.

The LHC has been completed at CERN and will start data taking in spring 2009. It is a proton-proton collider with a centre of mass energy of 14TeV. The design luminosity is $\mathcal{L}=10^{34}\text{cm}^{-2}\text{s}^{-1}$. At this luminosity there will be around 20 "minimum bias" QCD events per bunch crossing underlying the interesting events.

The ILC is an e^+e^- linear collider in superconducting technology. A reference design report has been submitted last summer [4], a detailed technical design is currently under way. In a first phase energy of $\sqrt{s}\leq 500$ GeV is envisaged, upgradable to $\sqrt{s}\leq 1\text{TeV}$. With an accelerating gradient of ~ 35 MeV/m the ILC will fit in a 30 km tunnel. The design luminosity is $\mathcal{L}\sim 2-5\cdot 10^{34}\text{cm}^{-2}\text{s}^{-1}$ corresponding to $\sim 200-500\text{fb}^{-1}/\text{year}$. Electron beams should be polarizable with a polarization of $P = 80-90\%$. A principle layout of the ILC is shown in Figure 1.

The ILC may be approved around 2012 when the first LHC results are available so that physics can start in the early 2020s. As an alternative a linear collider reaching higher energies around 3TeV using the two-beam accelerating scheme,

CLIC, is studied at CERN [5]. If physics requires higher energies and this technology turns out to be feasible, CLIC maybe built instead of the ILC a few years later.

PHYSICS AT LHC AND ILC

Of course it is not known which scenario nature has chosen. For that reason many sample scenarios have been studied. For all simulated models new effects have been found at the LHC and ILC. The high energy of the LHC and the precision of the ILC always proved to be complementary and the combination of both machines will improve our knowledge significantly. Both machines can be used optimally if they take data simultaneously for a while. In this report we will restrict ourselves to Higgs and Supersymmetry. A detailed assessment of LHC physics can be found in [6, 7] and of ILC physics in [8]. The complementarity of the LHC and ILC is discussed in [9].

HIGGS PHYSICS

Within the Standard Model the Higgs mass is the only unknown parameter of the Higgs sector. Once the Higgs is found and its mass measured, all properties can be predicted and the model can be tested. In Supersymmetry two Higgs doublets are needed leading to five Higgs particles, two scalars (h, H), one pseudoscalar (A) and a pair of charged Higgses H^\pm . The lightest Higgs must be lighter than 130GeV and is probably Standard Model like. However precision measurements may be able to distinguish the models. At the LHC the Higgs is dominantly produced by gluon-gluon fusion, however in this mode it can only be reconstructed if it either decays into photons or into WW or ZZ which in turn decay leptonically. If a Standard Model like Higgs exists the LHC will find it. If the Higgs is just above the LEP exclusion limit, the

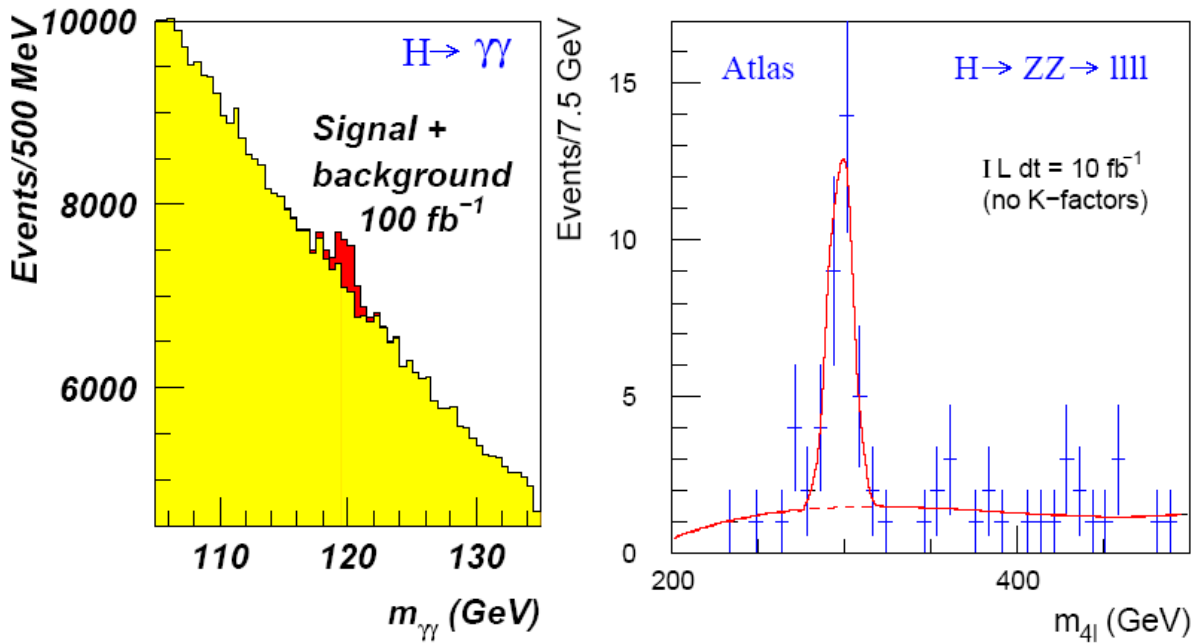


Figure 2. Left: CMS simulation of $H \rightarrow \gamma\gamma$; right: ATLAS simulation of $H \rightarrow ZZ$.

main discovery mode is $H \rightarrow \gamma\gamma$ which is challenging for the detector resolution (see fig. 2 left), however already around $m_H \sim 130 \text{ GeV}$ $H \rightarrow ZZ$ sets in, which is much easier to detect (see fig. 2 right).

As shown in fig. 3 the LHC can discover the Higgs with at least ten standard deviations over the full mass range leaving also some margin if the Higgs couplings are somewhat lower than predicted.

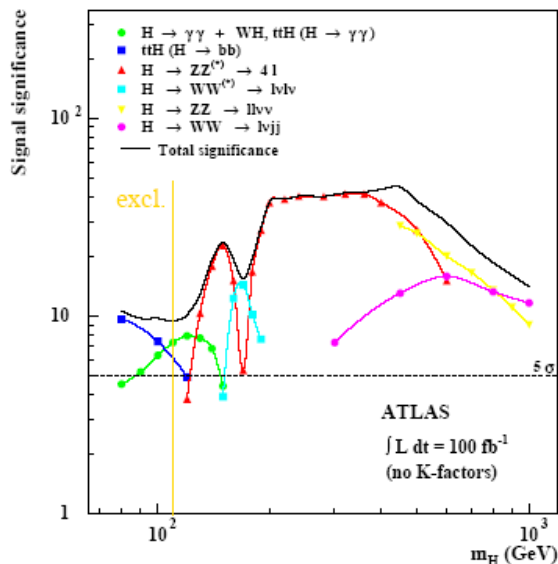


Figure 3. Expected significance for Higgs discovery combining ATLAS and CMS.

Once the Higgs is discovered its mass can be measured with a $O(100 \text{ MeV})$ precision relatively easily. Since the initial couplings are only badly

known and since especially the gg final state cannot be observed coupling measurements are very difficult to impossible. Also other quantum numbers like spin and CP can be measured only under certain conditions.

At low to moderate Higgs mass the dominant production process at the linear collider is the Bjorken process where the Higgs is radiated from an off-shell Z putting the Z back on mass shell. Using leptonic Z decays the Higgs can be reconstructed from the $\ell\ell$ recoil mass in a model independent way (see fig. 4 [10]). This measurement gives immediately the ZZH coupling to few percent precision and an absolute normalization for branching ratio measurements. As shown in Figure 5 e.g. the spin can be measured from a threshold scan.

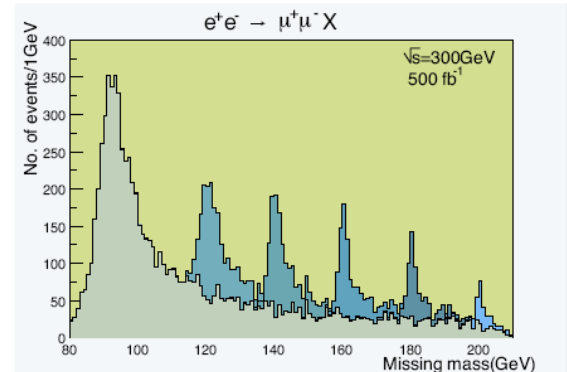


Figure 4. Recoil mass distribution for $e^+e^- \rightarrow \mu^+\mu^-X$ at the ILC for different Higgs masses [10].

Using the recoil measurement as normalization and identifying the Higgs final states

the Higgs couplings can be measured with a few percent precision. As shown in Figure 6 these measurements can be used to show that the Higgs really couples to mass [10]. In case deviations from the predictions are found, the pattern of the deviations can be used to identify the possible origin.

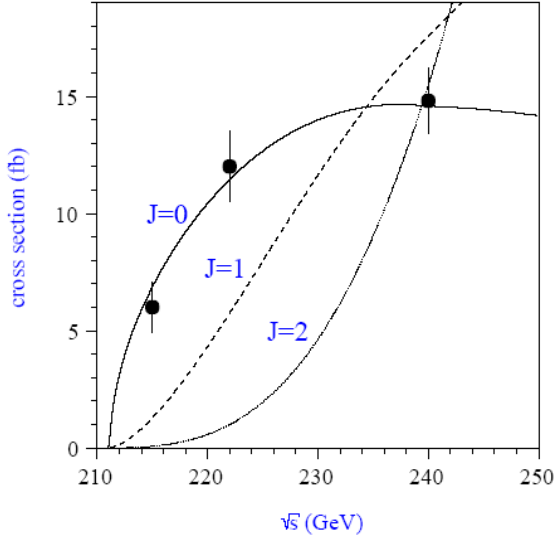


Figure 5. Threshold scan for the Higgsstrahlung process [11].

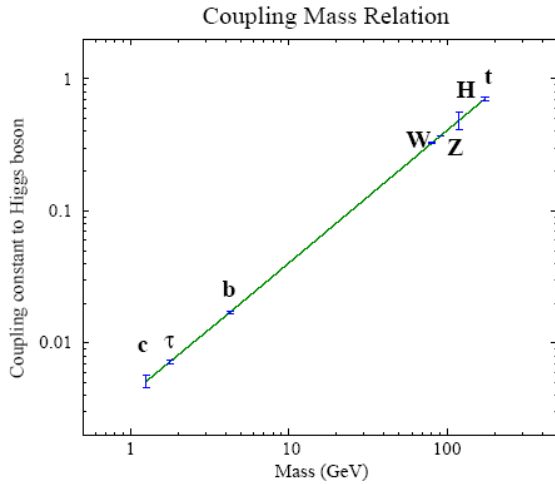


Figure 6. Precision of a Higgs coupling to a particle as a function of the particle mass [10].

SUPERSYMMETRY

Supersymmetry (SUSY) is symmetry between bosons and fermions where every Standard Model fermion gets a bosonic partner and every boson a fermionic partner [12, 13]. Since no superpartners have been found yet SUSY must be broken at a high scale. Due to cancellations in the radiative corrections SUSY solves the hierarchy

problem. If an additional R-parity is introduced, which protects the proton from a too fast decay, SUSY also offers a perfect dark matter candidate (LSP). Also, because of the new threshold, SUSY enables the unification of forces at a high scale. From LEP and the Tevatron we know, that all superpartners apart from the LSP should have a mass above about 100GeV. For the solution of the hierarchy problem to work the masses should be below about the TeV scale.

The partners of quarks and gluons, squarks and gluinos, have strong interactions and thus a large production cross section at the LHC. These particles decay in cascades producing the partners of the leptons and gauge bosons, sleptons, charginos and neutralinos, always ending in the LSP which escapes detection. SUSY events are thus always characterized by a large missing transverse energy often supplemented by leptons from the slepton decays in the cascades. Figure 7 shows the effective mass which is calculated from the visible and missing transverse momenta for the Standard Model and assuming a specific SUSY model. The two assumptions are well separated.

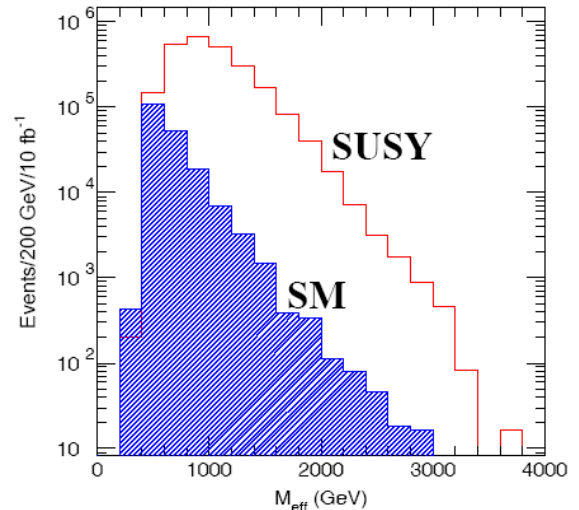


Figure 7. Effective mass for the Standard Model and assuming Supersymmetry.

Because of the two invisible LSPs, mass measurements at the LHC are difficult. However, mass differences of particles in the cascades can be reconstructed from invariant masses of combinations of decay products. Figure 8 shows the $\ell\ell$ mass from the process $\chi_2^0 \rightarrow \ell\ell \rightarrow \ell\ell\chi_1^0$. The sharp upper edge is a measurement of the $\chi_2^0 - \chi_1^0$ mass difference.

Since SUSY particles are produced in pairs the ILC can see them with masses basically up to the beam energy. It is improbable that squarks and gluinos can be seen at the ILC however there is a high chance that sleptons and the lighter charginos and neutralinos are visible. For all particles that are

produced, even the invisible ones, the properties, especially the masses can be measured using energy-momentum conservation. As an example, Fig. 9 shows the muon energy spectrum for the process $e^+e^- \rightarrow \tilde{\mu}_R^+ \tilde{\mu}_R^-$ [14].

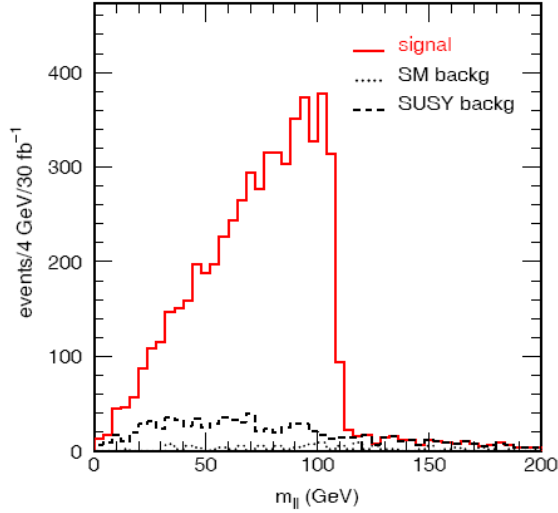


Figure 8. $\ell^+ \ell^-$ mass from $\chi_2^0 \rightarrow \ell \ell \rightarrow \ell \ell \chi_1^0$.

The smuon as well as the lightest neutralino mass can be obtained to a precision around 100MeV from the upper and lower edges of the spectrum. The precise determination of the neutralino mass also greatly helps the LHC. Fig. 10 shows the measurement of the squark and lightest neutralino mass at this machine. Due to the escaping neutralino there is a large correlation between the two uncertainties. Fixing the neutralino mass to the ILC value thus reduces the error on the squark mass significantly.

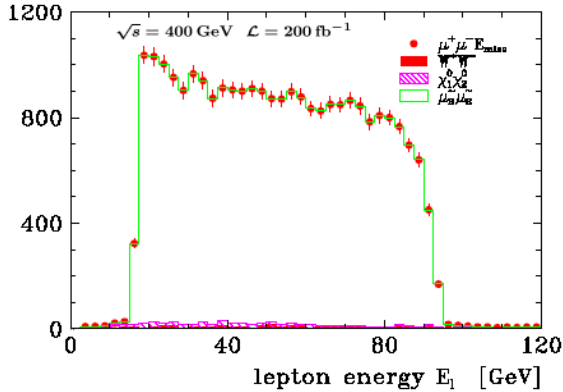


Figure 9. Muon energy spectrum for smuon-pair production at the ILC [14].

From the mass measurements at the LHC and ILC the SUSY breaking parameters at the weak scale can be obtained and extrapolated to high scales to test if the SUSY masses and the couplings unify at the same scale. As an example, Figure 11 shows this extrapolation for the gaugino and scalar mass parameters assuming a minimal SUGRA model [15].

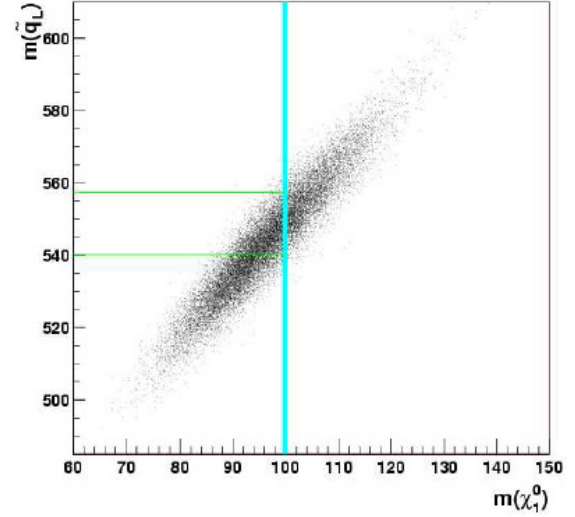


Figure 10. LHC measurement of the \tilde{q}_L and $\tilde{\chi}_1^0$ mass together with the $\tilde{\chi}_1^0$ -mass measurement of the ILC.

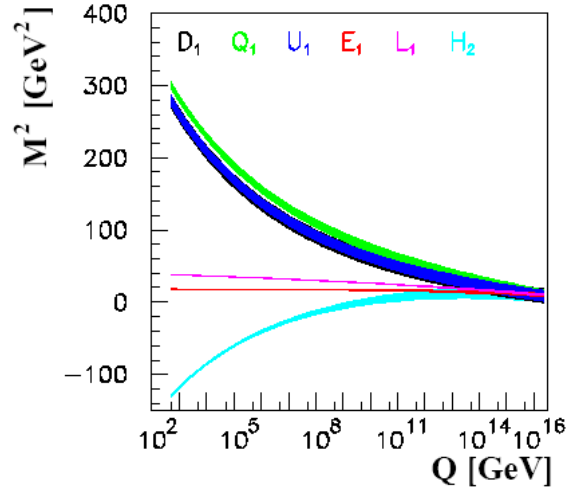
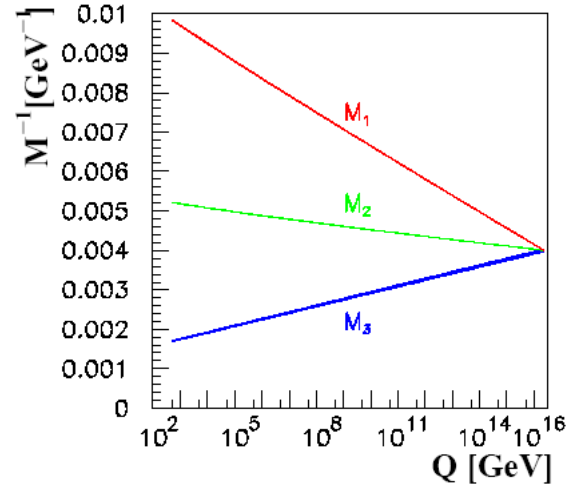


Figure 11. Evolution from low (top) to high (bottom) scales of Gaugino and scalar mass parameters in the MSSM [15].

To test if we really understand cosmology the dark matter particle needs to be found and its properties need to be measured. The dark matter

density can then be calculated and compared to the experimental result from cosmic microwave radiation. In case special mass conditions hold like a quasi degeneracy of the LSP with another SUSY particle or special resonance conditions, like a Higgs with twice the LSP mass, also the properties of these other contributing particles need to be known. Figure 12 compares for one specific scenario the accuracy reachable at the LHC and ILC with the ones that are obtained or will be obtained at cosmic microwave experiments [16]. In this scenario the LHC can do a crude check while the ILC precision matches the one of the Planck satellite testing with a few percent if we understand the connection between particle physics and cosmology.

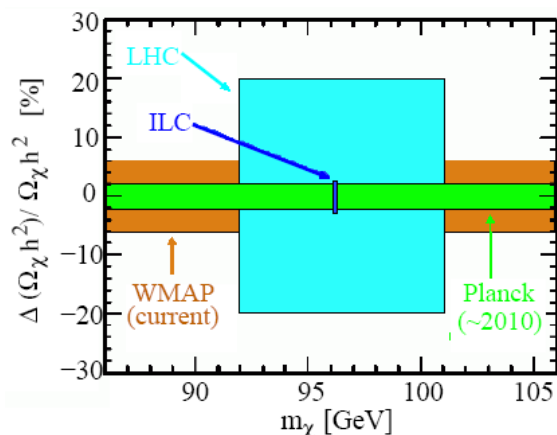


Figure 12. Accuracy of WMAP and expected accuracy of Planck compared to the LHC and ILC accuracies in the determination of the LSP neutralino mass and the cosmological relic density [16].

CONCLUSIONS

There are still some fundamental open problems in our understanding of the fundamental laws of nature. For most of these problems we can expect some answers from experiments at the TeV scale which is exactly the energy scale of the next generation of accelerators. The LHC is currently being commissioned and first results are expected for 2009. The LHC will give us first answers about the class of theories that are realized in nature. For a final understanding, however, an e^+e^- linear collider like the ILC or CLIC will be needed in addition. If the financial resources are available such a collider could start data taking in the early 2020s.

REFERENCES

[1] The ALEPH, DELPHI, L3, OPAL, SLD Collaborations, the LEP Electroweak Working Group, the SLD Electroweak and Heavy Flavor Working Groups, Phys. Rept. 427,

257 (2006), [hep-ex/0509008].
 ALEPH, DELPHI, L3 and OPAL Collaborations, and LEP Working Group for Higgs Boson Searches, R. Barate et al., Phys. Lett. B565, 61 (2003), [hep-ex/0306033].
 [2] L. Evans, New J. Phys. 9, 335 (2007).
 [3] Understanding Matter, Energy, Space and Time: the Case for the Linear Collider, http://sbhep1.physics.sunysb.edu/~grannis/lc_consensus.html
 [4] J. Brau et al. [ILC Collaboration], arXiv:0712.1950 [physics.acc-ph].
 [5] R. W. Assmann et al., CERN-2000-008.
 [6] ATLAS Collaboration, Detector and Physics Performance Technical Design Report, **CERN/LHCC/99-15**.
 [7] G. L. Bayatian et al. [CMS Collaboration], J. Phys. G 34 (2007) 995.
 [8] A. Djouadi et al., arXiv:0709.1893 [hep-ph].
 [9] G. Weiglein et al. [LHC/LC Study Group], Phys. Rept. 426 (2006) 47 [arXiv:hep-ph/0410364].
 [10] ACFA Linear Collider Working Group, K. Abe et al., hep-ph/0109166.
 [11] M. T. Dova, P. Garcia-Abia and W. Lohmann, hep-ph/0302113.
 [12] J. Wess and B. Zumino, Nucl. Phys. B70, 39 (1974); Yu. A. Gol'fand and E. P. Likhtman, JETP Lett. 13, 323 (1971).
 [13] M. E. Peskin, arXiv:0801.1928 [hep-ph].
 [14] H.-U. Martyn, arXiv:hep-ph/0302024, LCPHSM-2003-07.
 [15] G. A. Blair, W. Porod and P. M. Zerwas, Eur. Phys. J. C27, 263 (2003), [hep-ph/0210058].
 [16] E. Baltz, M. Battaglia, M. Peskin and T. Wizansky, Phys. Rev. D74, 103521 (2006).

ACKNOWLEDGEMENTS

I would like to thank the organizers of the workshop, especially Ivanka Bozovic for the perfect organization of the workshop and the nice atmosphere during the meeting.

A VARIATIONAL ESTIMATE OF THE HIGGS MASS

By

Veljko DMITRAŠINOVIĆ¹

(1) INN Vinča

I discuss the predictions of the “Gaussian functional” variational approximation to the Higgs particle mass in the Standard Model.

Key words: Higgs mass, functional Gaussian (variational) approximation

INTRODUCTION

FCAL@ILC is dedicated to new particle searches (e.g. SUSY), as well as to high precision physics (e.g. measurements of anomalous couplings of W,Z bosons). This is, of course, assuming the validity of the Standard Model. One (the last?) open question in the Standard Model (modulo neutrino masses and CP violation), is the Higgs particle, which should (must?) be found @LHC (2009-12?). We address one conservative scenario of what may happen if LHC does not find the Higgs boson within the present (one-loop approximation) mass limits.

The Higgs sector of the Standard Model (linear sigma model)

The “Mexican hat” potential

$$V_{Higgs, \sigma model}(\phi_i) = -\frac{m_0^2}{2}(\phi_i \phi_i) + \frac{\lambda}{4}(\phi_i \phi_i)^2 \quad (1)$$

where $i=0,1,2,3$, provides a mechanism for the spontaneous breaking of the O(4) symmetry. It leads to a non-vanishing “vacuum” expectation value (v.e.v.) of one, say the 0th, scalar field

$$\langle \phi_0 \rangle = \varphi_0 = f = (\sqrt{2}G_F)^{-1/2} = 246 GeV \quad (2)$$

which we call the Higgs field. The rest of the scalar fields are the “would-be” Nambu-Goldstone (NG) bosons which are absorbed into the longitudinal polarization components of the gauge bosons, the Higgs mechanism. The mass of the Higgs is proportional to the v.e.v. f , as are all the fermion and vector boson masses in the Standard Model, at least in the first Born approximation. The one-loop corrections lead to non-linear effects that place sometimes quite severe constraints on the Higgs mass from other measurements. Manifestly, the functional form, and perhaps even the numerical value(s) of these corrections depend on the order of the perturbation theory used.

The (hypothetical) question we shall consider is: What if LHC fails to find Higgs in the predicted

region? Of course, there are many scenarios for heavier Higgs(es). But, the most mundane loophole is that the afore-mentioned constraints were derived at the one-loop approximation level! What if the Standard Model is OK, but higher loops are just as important as the lower ones? We need a non-perturbative approximation to answer that question, e.g. a variational one! But what is a variational approximation to a quantum field theory (QFT)?

BASICS OF VARIATIONAL APPROXIMATIONS IN QFT

Variational method minimizes the ground state [g.s.] energy w.r.t. some variational parameters. This is standard procedure in quantum mechanics (QM), but how do you do it in quantum field theory (QFT)? We go back to Ref. [1]. We must work in Schroedinger picture, see [2], and need a trial wave function(al) for the ground state: one Gaussian in momentum space for each harmonic oscillator -- eigen-mode of the field

$$|\Psi_0[\vec{\phi}_k]\rangle = \quad (3)$$

$$\left(\prod_k \left(\frac{\omega_k}{\pi} \right)^{1/4} \right) \exp\left[-\frac{1}{2} \int \frac{d\vec{k}}{(2\pi)^3} \omega_k \tilde{\phi}(\vec{k}) \tilde{\phi}(-\vec{k}) \right]$$

The Gaussian wave functional is just a product of infinitely many Gaussian wave functions.

Gaussian wave functional

Configuration space Gaussian Ansatz trial wave functional for the ground state:

$$\begin{aligned} |\Psi_0[\phi_i]\rangle &= |\Psi_0[\phi_i(m_i, \varphi_i)]\rangle = \\ & N \exp\left[-\frac{1}{4\hbar} \int d\vec{x} \int d\vec{y} (\phi_i(\vec{x}) - \varphi_i) \right. \\ & \times G_{ij}^{-1}(\vec{x} - \vec{y}, m_i) (\phi_j(\vec{y}) - \varphi_j) \left. \right] \\ & G_{ij}^{-1}(\vec{x} - \vec{y}, m_i) = \frac{1}{2} \delta_{ij} \\ & \times \int \frac{d\vec{k}}{(2\pi)^3} \frac{1}{\sqrt{k^2 + m_i^2}} \exp(i\vec{k} \cdot (\vec{x} - \vec{y})) \end{aligned} \quad (4)$$

Theory with N scalar fields [O(N) sigma model], function of $2N$ variational parameters (N masses and N v.e.v.s): (m_i, φ_i) .

FGA in the linear sigma model

Evaluate the energy expectation value in the ground state

$$E_0(m_i, \varphi_i) = \langle \Psi_0 | H | \Psi_0 \rangle \langle \Psi_0 | \Psi_0 \rangle^{-1}$$

and minimize w.r.t. the variational parameters

$$\left. \frac{\partial}{\partial m_j} E_0(m_i, \varphi_i) \right|_{\min} = 0$$

$$\left. \frac{\partial}{\partial \varphi_j} E_0(m_i, \varphi_i) \right|_{\min} = 0 \quad (6)$$

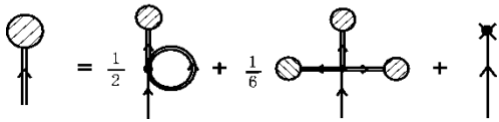
The resulting ground state (“vacuum”) energy is related to the “effective potential”

$$V_{eff}(\varphi_i) = E_0(m_i, \varphi_i)_{\min} - E_0(m_i, \varphi_i = 0)$$

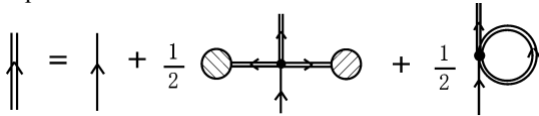
V_{eff} modifies/“renormalizes” the old (up to the 4th order) and produces new, higher-order vertices. (7)

Diagrammatic interpretation

From the minimization w.r.t. v.e.v. follows the zero-particle (“vacuum”) Schwinger-Dyson equation.



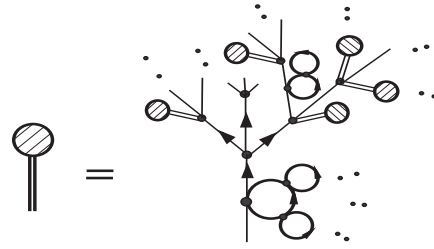
From the minimization w.r.t. masses follows the one-particle (“gap”) Schwinger-Dyson equation.



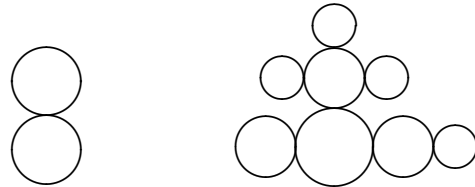
Physical meaning of the FGA

These SD eqs are integral eqs. Their iteration produces (sums of) infinitely many ordinary Feynman diagrams, e.g. see Fig below for the „tadpole“ graphs produced by the „vacuum“ SD

equation.



Note that it contains loop sub-diagrams that resemble cacti or daisies (flowers), see Fig.



(1.a)

(1.b)

Thus we may say that the FGA sums all „cactus“, or „daisy“ loop diagrams. This is manifestly an infinitely-many-loops non-perturbative approximation. Each loop by itself contains a numerical infinity, so one must first regularize and then renormalize the FGA effective potential/ground state energy! At this moment there are two schemes for the non-perturbative renormalization: 1) the so-called “autonomous” renormalization (with $(\lambda_b \geq 0)$) [4], and 2) the “precarious” scheme ($\lambda_b \leq 0$) [5], corresponding to two possible approaches of space-time dimensionality d to 4: $d \nearrow 4$ and $d \searrow 4$.

VARIATIONAL APPROXIMATION TO THE U(1) HIGGS MODEL

Gaussian effective potential for the U(1) Higgs model

Ibanez-Meier, Stancu and Stevenson [6] evaluated the U(1) Abelian Higgs model FGA effective potential using autonomous renormalization, and found a huge Higgs mass:

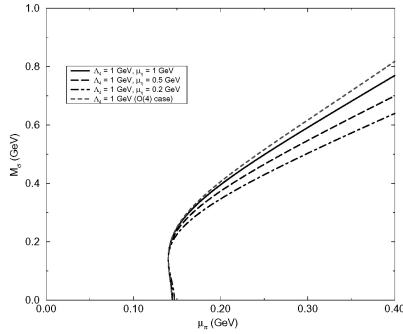
$$m_{Higgs} \approx 2\sqrt{2}\pi f = 2\sqrt{2}\pi \times 246 GeV \approx 2 TeV \quad (8)$$

This calculation was challenged on the grounds that “it is not gauge invariant”. What does this mean?

The Higgs mechanism turns the would-be Nambu-Goldstone bosons into longitudinal components of gauge bosons; this works only if the NG bosons are exactly massless. Otherwise, it violates the underlying U(1) symmetry.

Properties of Nambu-Goldstone fields in FGA

There are two coupled nonlinear (gap) equations with two unknowns, M, μ , and a new loop parameter, e.g. cutoff Λ , necessary to regularize the infinite integral, that determine the ground state/“vacuum” of the theory.

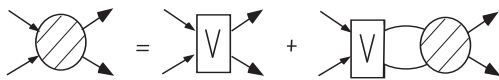


One free parameter can be fixed by demanding that Eq. (2) holds, so one is left with one equation with two unknowns, i.e. a line in a two-parameter space, see the Fig above/below.

The solutions do not have the (naively) expected properties: The (Nambu-Goldstone) meson field is not massless ($\mu \neq 0$), even in the chiral limit, (unless $M=0$ at the same time, which implies $v=f=0$, i.e., a spontaneously restored symmetry), as first noted by Kamefuchi, and H. Umezawa in 1964 [7]. Thence the statement that “FGA is not gauge invariant”.

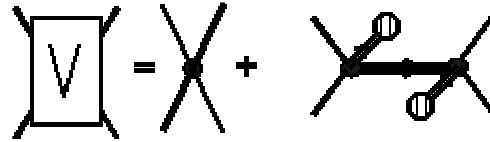
Solution to the NG boson problem in FGA

The NG theorem problem in the FGA was solved in 1994 (though published only two years later, [8]): It turns out that the “gap” mass μ is not the (physical) Nambu-Goldstone mass. The physical NG boson mass is given by the pole in the 4-point function, which satisfies the Bethe-Salpeter equation:



Four-point function and Bethe-Salpeter equation in FGA

The Bethe-Salpeter equation in the Gaussian functional approximation is defined by the fourth (functional) derivative of the FGA effective action. The kernel of the BS eq. is also determined in this way and is given by the diagrams

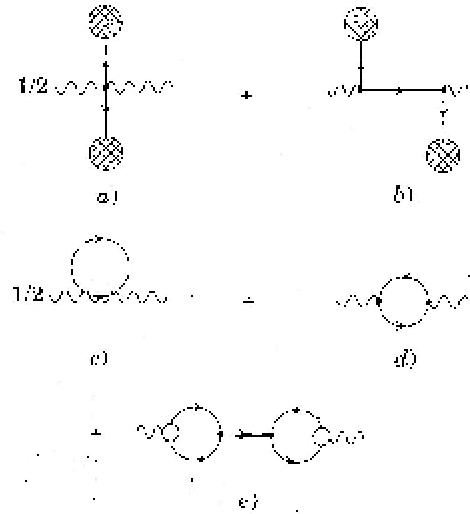


The solution to this Bethe-Salpeter equation has been found, and it has a pole at $m=0$, so long as the gap Eqs. (6) hold, irrespective of the details (values of the bare couplings/masses) as a Ward-Takahashi identity should, which fact is interpreted as the vanishing mass of the *composite* NG boson.

This ought to have been enough for the proof of “gauge invariance” of the FGA, but still, further doubts were raised, *viz.* if the conventional Higgs mechanism would work in the FGA.

Gauge invariance of Higgs mechanism in FGA

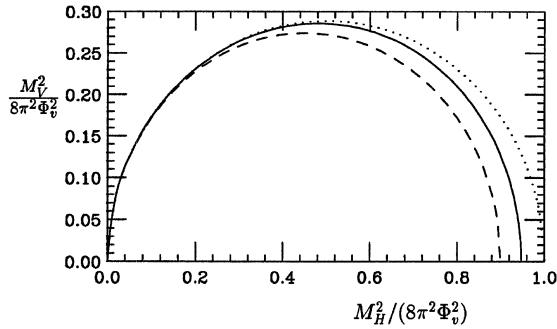
In Ref. [9] we explicitly constructed the vacuum polarization tensor (the gauge boson propagator) in the FGA in a class of Lorentz covariant gauges, see figure below. We showed its gauge invariance and evaluated the gauge boson mass. Thus all gauge problems were resolved: FGA may be used in the Standard Model.



Gaussian approximation to the SU(2) Higgs model

Using the “autonomous” non-perturbative renormalization prescription, the relation shown in the following figure between the Higgs and the vector boson masses was found in [6]. Note that the perturbative regime corresponds to the left-hand side of the figure, whereas the non-perturbative regime is in the right-hand-side corner.

U(1) Abelian Higgs model calculation was extended to non-Abelian SU(2) in Ref. [13].



It leads to only a small shift of the Higgs mass: $2 > 2.2$ TeV. The relation between the vacuum expectation value and the Higgs mass Eq. (8) has an interesting, classically scale-invariant form, which seems to imply that a (non-perturbative) renormalization group fixed point has been found. If so, these results ought to reflect the property called “triviality” of the $\lambda \phi^4$ theory in four space-time dimensions.

Gaussian approximation and “triviality”

In $4+\epsilon$ dimensions the $\lambda \phi^4$ theory is believed to be non-interacting (“trivial”). Similarly, in $4-\epsilon$ dimensions the theory is (at least formally) renormalizable. What happens in the limit of exactly four dimensions? The exact solution to this theory is supposed to have the property called “triviality”. Since the FGA already shares many of its nonperturbative properties (such as unitarity and causality [14],[15]) with the (as yet unknown) exact solution, Consoli and Stevenson conjectured that the FGA is also “trivial” [10]. In order to prove their point, they conducted lattice calculations [11], a study of Landau poles, ultraviolet fixed points, and ‘triviality’ in the perturbative expansion [12], as well as mode-dependent field renormalization [13] of the $\lambda \phi^4$ in four-dimensions, which is well beyond my field of expertise.

SUMMARY

The Functional Gaussian Approximation to the Higgs model is: (a) Lorentz and gauge invariant [8,9], (b) causal and unitary [14],[15], (c) self-consistent and non-perturbative, and (d) exact in the limit of large N [3],[16]. So it has all the properties of an exact solution to this QFT, and may be used to calculate infinitely-many-loop corrections to observables, if the results of the Higgs search at LHC deem it necessary.

Challenges for the future:

The physical interpretation of the FGA results is not always straight-forward, due to the non-perturbative character of the approximation.

Consequently, the renormalization is complicated and perhaps even ambiguous. If the Higgs boson is not found within the window predicted by the one-loop Standard Model then that will be a good reason to further develop the Gaussian functional approximation.

REFERENCES

- [1] L.I. Schiff, Phys. Rev. **130**, 458 (1963); for a physically equivalent approach based on functional calculus, see T. Barnes and G.I. Ghandour, Phys.Rev. **D22**, 924 (1980).
- [2] B. Hatfield, *Quantum Field Theory of Point Particles and Strings*, Addison-Wesley, Reading (1992); R.J. Rivers, *Path Integral Methods in Quantum Field Theory*, Cambridge University Press, Cambridge (1987).
- [3] T. Barnes and G.I. Ghandour, Phys. Rev. **D22**, 924 (1980);
- [4] P.M. Stevenson, B. Alles and R. Tarrach PR **D35**, 2407 (1987).
- [5] P.M. Stevenson, PR **D32**, 1389 (1985).
- [6] R. Ibanez-Meier, I. Stancu and P.M. Stevenson. Z.Phys. **C70**, 307 (1996); [hep-ph/9207276].
- [7] S. Kamefuchi, and H. Umezawa, Nuov. Cim. **31**, 429 (1964).
- [8] V. Dmitrašinović, J. A. McNeil and J. Shepard, Z. Phys. C **69**, 359 (1996) [hep-th/9406151].
- [9] V. Dmitrašinović, Nuov. Cim. **109A**, 1187 (1996).
- [10] Consoli and Stevenson [hep-ph/9303256]
- [11] M. Consoli and P.M. Stevenson, Z.Phys. **C63**, 421 (1994).
- [12] M. Consoli and P.M. Stevenson, Mod. Phys. Lett. **A11**, 2511 (1996).
- [13] M. Consoli and P.M. Stevenson, Phys.Lett. **B391**, 144 (1997).
- [14] V. Dmitrašinović, Phys. Lett. **B 433**, 362 (1998). I. Nakamura and V. Dmitrašinović, Prog. Theor. Phys. **106**, 1195 (2001).
- [15] I. Nakamura and V. Dmitrašinović, Nucl. Phys. **A713**, 133 (2003).
- [16] V. Dmitrašinović and I. Nakamura, J. Math. Phys. **44**, 2839 (2003).

Forward region at ILC and other experiments

FAST BEAM CONDITIONS MONITORING (BCM1F) FOR CMS

By

N. BERNARDINO RODRIGUES^a, R. HALL-WILTON^b, W. LANGE^c, A. MACPHERSON^b,
V. RYJOV^b, R. L. STONE^d

^a Canterbury University, 8041 Christchurch, New Zealand

^b CERN, 1211 Geneva 23, Switzerland

^c DESY Zeuthen, 15738 Zeuthen, Germany

^d Rutgers University, 08854 Piscataway, NJ, USA

wolfgang.lange@desy.de

Abstract

The CMS Beam Conditions and Radiation Monitoring System (BRM) [1] is composed of different subsystems that perform monitoring of, as well as providing the CMS detector protection from, adverse beam conditions inside and around the CMS experiment. This paper presents the Fast Beam Conditions Monitoring subsystem (BCM1F), which is designed for fast flux monitoring based on bunch by bunch measurements of both beam halo and collision product contributions from the LHC beam. The BCM1F is located inside the CMS pixel detector volume close to the beam-pipe and provides real-time information. The detector uses sCVD (single-crystal Chemical Vapor Deposition) diamond sensors [2] and radiation hard front-end electronics along with an analog optical readout of the signals.

INTRODUCTION

The CMS experiment sits in an unprecedentedly high radiation field and much effort has gone into the design and construction of systems with very high radiation tolerance. The LHC is designed to run with 362MJ of stored energy in one beam and with proton intensities in excess of 10^{14} per beam. Even very small fractional losses of this beam risk causing serious damage to detector elements.

Whilst the LHC itself has extensive instrumentation designed for machine protection, CMS requirements dictate that CMS must be able to detect beam-related problems as they develop and to assert beam aborts if required. In addition, CMS must be able to log data and perform post-mortem analysis in the case of accidents and understand the accumulated dosage and potential long term damage to the detector elements. For this reason CMS has implemented the BRM systems. Some of the sub-systems can be used to initiate LHC beam aborts and/or CMS equipment control, others can be used for fast beam and detector optimisations. Therefore the protection systems must be sensitive to very fast changes in beam conditions; the BRM systems can detect changes at the 25ns level, although the initially deployed protection systems will react in 3 μ s to 40 μ s.

The BCM1F is one of the fast monitoring systems designed to provide fast real-time diagnosis

of beam conditions with readouts able to resolve the sub-bunch structure.

BCM1F will serve as a diagnostic tool to be able to flag problematic beam conditions resulting in “bursts” of beam loss over very short periods of time. Such beam losses are expected to be one of the principle damage scenarios for the CMS detector systems. The location of the two the BCM1F planes allows for separation between ingoing and outgoing particles from the IP. Thus one can compare background rates from beam halo and rates from luminosity products.

SYSTEM OVERVIEW

The BCM1F is based on sCVD diamond detectors fast enough to match beam abort scenarios and small enough to be inserted into areas close to key detector components of CMS without adding substantial amounts of material or services.

The system is based on eight sCVD diamonds, each 5x5x0.5mm³, four positioned on either side of the IP at Z values of ± 1.8 m close to the beam pipe and the pixel detectors at a radius of 4.5 cm (Figure 1).

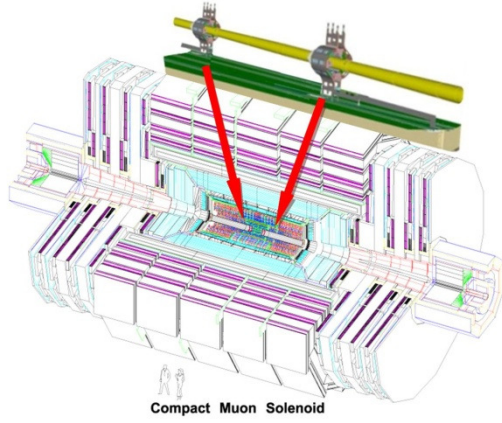


Figure 1: BCM1F locations

Four BCM1F diamonds are arranged in a polar (Z-) plane. The diamond sensor is connected to a JK16 radiation hard amplifier [3], after which the signal is transmitted to the counting room (Figure 2) over an analog optical link built from the CMS tracker optical components [4]. The back end readout produces rate, multiplicity, timing and coincidence information independently of the CMS DAQ. However, there is the possibility to feed information into the event stream via a standard CMS SLINK.

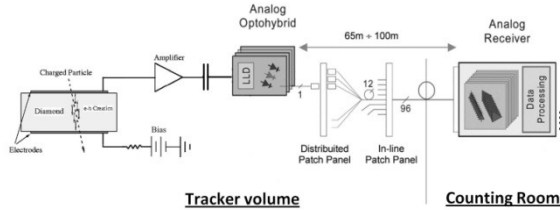


Figure 2: BCM1F readout sketch

A. sCVD Sensors

Properties like their low leakage current and fast signal response and their low capacitance (contributing to high SNRs), in addition to their small physical dimensions and their radiation hardness, make CVDs diamonds an ideal choice for the locations close to the interaction region. The sensor concept (solid state ionisation chamber) and layout is similar to silicon detectors: two metallization pads on the opposite surfaces of the crystal are used to apply the electric field and to collect signal currents when charged particles pass through. Polycrystalline diamond detectors have already successfully been used [5,6] as detectors for charged particles in recent collider experiments.

The majority of actual diamond detector developments are based on polycrystalline (pCVD) sensors, but recent improvements in quality and size of single crystals in conjunction with its superior electrical properties (table 1) determined the choice of this material for the BCM IF sensors.

The sensors were manufactured by Element Six [7] after a years of development and research in collaboration with the RD42 [8] project at CERN.

Table 1: pCVD and sCVD electrical properties

PROPERTY	Polycrystalline CVD diamond	Single crystal CVD diamond
Hole mobility (cm ² /Vs)	1,000	3,800
Electron mobility (cm ² /Vs)	1,800	4,500
Carrier lifetime (ns)	~1-10	~2,000
Voltage breakdown (MV/cm)	~0.5	~4
Charge collection distance (μm)	~250 at 1V/μm field	Thickness limited

B. Front-end Electronics

In addition to the required radiation hardness, the (given) detector locations have constrained the front-end layout, readout, monitoring, powering and test facilities.

1) Amplifier:

The BCM1F preamplifier (Figure 3) is the front-end part of an ASIC developed for readout of silicon strip detectors. The chip is fabricated in a commercial 0.25μm CMOS technology radiation-hardened by special layout techniques.

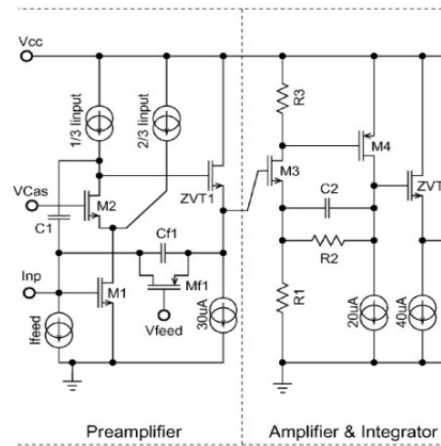


Figure 3: Schematic diagram of one JK16 channel

Each of the 16 channels comprises a fast transimpedance preamplifier working with an active feedback loop and an amplifier-integrator stage providing a 20 ns peaking time. The circuit has an input capacitance of 4 pF and a charge gain of 60 mV/fC. An excellent noise performance is achieved by the proper choice of the feedback current.

For a detector capacitance of 5pF the measured noise is about $700e^-$ (equivalent noise charge, ENC) at the output of the preamplifier.

2) Optical Readout:

Parts of the CMS tracker's analog optical chain are used to deliver the signals of the BCM1F detector to the S1 counting room (figure 2). The single ended output of the preamplifier is AC coupled to the laser driver (LLD-A SIC) [9], which modulates the current of the edge-emitting laser diode. Single mode fibers from the pigtailed lasers are connected at the periphery of the tracker volume via optical connectors to a fan-in merging all single fibers into a 12-fiber ribbon. A second optical patch panel within the CMS detector connects this ribbon to a rugged multi-ribbon cable (8x12-fiber ribbons/cable). In the S1 counting room each ribbon connects directly to a 12-channel analog optical receiver.

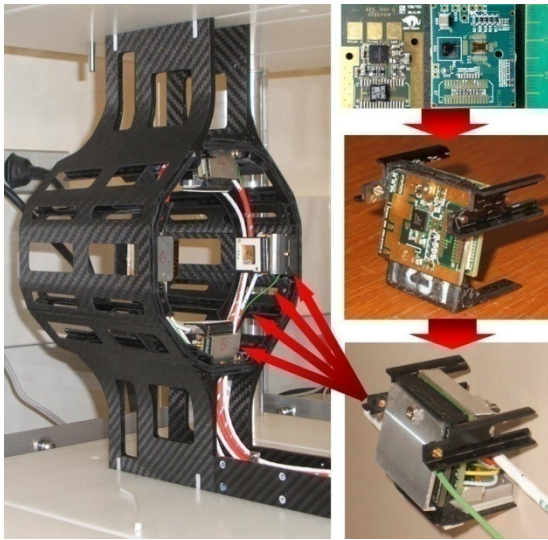


Figure 4: Sensor and AOH boards mounted on their carriage

Due to the limitation in size of the frontend parts, a piggy-back architecture was chosen to interconnect and mount the sensor/preamplifier board and the analog optical hybrid (AOH) board onto the carrying carbon fiber support (see figure 4). Minor modifications were done to the original AOH to allow for a different orientation of the laser diode. This assures a minimal bending radius of the pigtail fibers for all mechanical positions. For the BCM1F both the AOH gain and the laser diode bias current cannot be programmed since an I²C interface is not available at the installation position. Hence, a lot of investigation was made to choose the optimal input signal polarity and the optimal laser bias setting to preserve the dynamic range of the receiver side as well as to compensate for heat and radiation impacts on the laser diode itself.

C. Patch Panels and Back-end Electronics

Two sets of patch panels are foreseen. In the S1 counting room, a VME crate houses the PPS1 patch panels which combine and filter bias and supply voltages. Test pulses are optionally modulated onto the high voltage (bias) lines.

A multi-service copper cable (8 twisted pairs) connects to the tracker bulkhead, where the PP0 patch panel is used to re-arrange power supply lines and to decouple and recover the test-pulses for each detector.

A CMS tracker type 12-channel analog opto-receiver module is used for the BCM1F as well. The converted (electrical) signals are fanned-out to the different branches of the readout system:

The BCM1F outputs are sampled at 500 MHz by an 8-bit resolution flash ADC (CAEN). The ADC can be triggered externally or internally. Each channel can store up to 2 Megasamples. In the continuous sampling mode the module could store signals of 45 consecutive orbits in the LHC.

In addition, a general purpose multihit TDC with 20 bit resolution and 0.8ns LSB will be used to measure time intervals from different sensors as well as between ingoing beam particles and outgoing interaction products. A sketch of back-end electronics is shown on Figure 5.

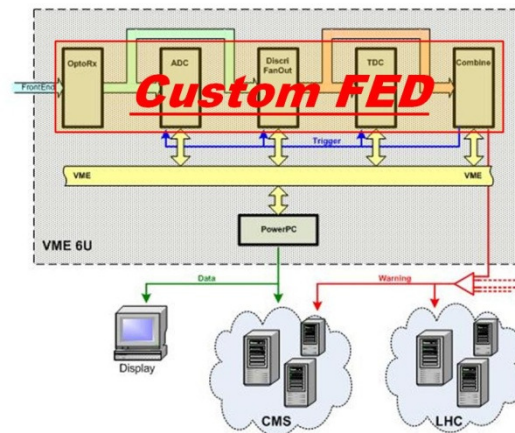


Figure 5: BCM1F backend sketch

A future custom Front End Driver (FED) module is currently under development. The module will have 16 input channels and data processing capabilities.

SENSOR TEST RESULTS

The assembled front-end modules were tested with a ⁹⁰Sr source. Figure 6 shows measured pedestal and pulse height distributions collected at different sensor bias voltages. The pedestals are uniform, one can see a good signal to noise separation. At 0.23V/ μ m field strength (110V bias

for 480µm sensor thickness) the sensors reach their maximum signal (see figure 7), providing a signal-to-noise ratio of 26 at the output of the preamplifier.

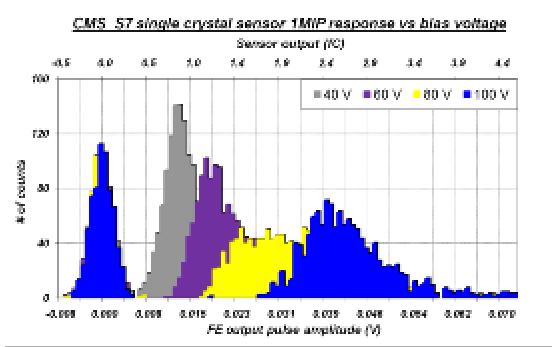


Figure 6: BCM1F module pulse height distributions

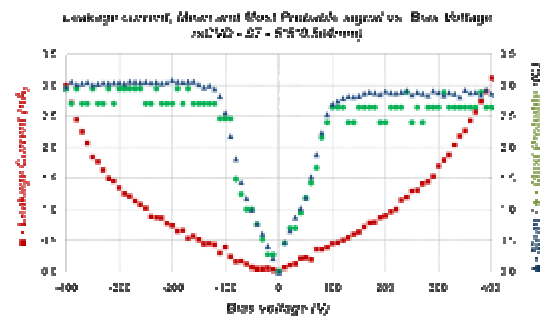


Figure 7: sCVD-S7 MIP response versus bias voltage

Figure 7 also shows the observed leakage current of a typical sensor as well as mean and most probable values of ⁹⁰Sr signals as a function of the bias voltage. The leakage current is dominated by the test setup and passive components on the front-end board.

RADIATION TOLERANCE STUDIES

The radiation hardness of single crystal sensors has been studied at the Technical University of Darmstadt (S-DALINAC facility: 10 MeV electrons) and at CERN (hadrons) in 2007. Two sCVD sensors (S1 and S2) were exposed to a 60MeV proton beam with an integrated flux of about 3×10^{14} p/cm². The crystal dimensions and radiation doses are listed in Table 2.

Table 2: sCVD dimension and fluence

Sensor sCVD	Thickness	Size	Radiation dose @60MeV	MIP equiv. radiation dose
S1	480µm	4*4 mm ²	3×10^{14} p/cm ²	17.5×10^{14} MIP/cm ²
S2	488µm	4*4 mm ²	3×10^{14} p/cm ²	17.5×10^{14} MIP/cm ²
S7	465µm	5*5 mm ²	none	none

The performance of the irradiated samples was measured and compared with similar non-irradiated sCVD crystals.

The test results are shown in Figure 8. Significant signal losses as well as a noise increase were observed. The 1-MIP response has decreased by roughly 80% and the signal to noise ratio degraded from 26 to 7 at a high electric field in the crystal.

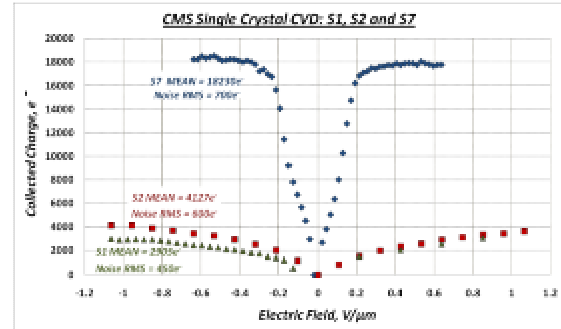


Figure 8: Irradiated and non-irradiated samples MIP response

Previous studies of the polycrystalline CVD diamond radiation hardness [4, 10] have been performed at 24GeV and 26MeV proton beams. The results show a significant difference in sensor damage at low and at high beam energies.

INSTALLATION AND FIRST LHC BEAM HITS

The BCM1F assemblies were successfully installed at begin of August 2008. All 8 modules were tested extensively. They are now commissioned for operation.

Several hundred hits were collected from the very first particles which have been circulated in the LHC on September 10, 2008. The plot on Figure 9 shows a signal height distribution from one BCM1F module. It shows a very good separation of signal and noise. Much more detailed studies will follow.

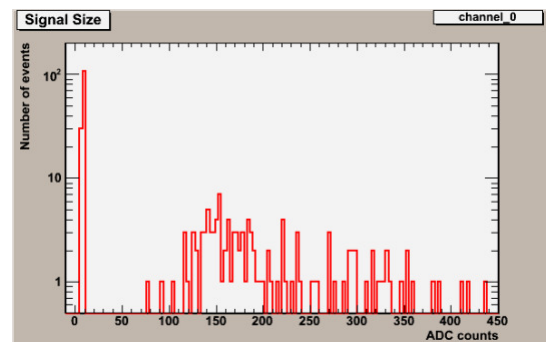


Figure 9: BCM1F pulse height distribution for first LHC beam

CONCLUSION

A general overview of the sCVD based fast beam condition monitor was presented. All parts of the system were successfully installed and exhaustively tested in their final positions in the CMS detector. The detectors and their readout chains demonstrated the expected performance under real working conditions at CMS during the very first days of the LHC operation.

REFERENCES

- [1] L. Fernandez-Hernando et al., "Development of a CVD diamond Beam Condition Monitor for CMS at the Large Hadron Collider", NIM A552 (2005) 183.
- A. Macpherson, "Beam Condition Monitoring and radiation damage concerns of the experiment", Proceedings LHC Project Workshop, Chamonix XV (2006) 198.
- D. Chong et al., "Validation of synthetic diamond for a Beam Condition Monitor for the Compact Muon Solenoid Experiment", IEEE Trans. Nucl. Sci. 54 (2007) 182.
- [2] R.J.Tapper, "Diamond detectors", Rep. on Prog. in Phys. 63 (2000) 8.
- [3] J. Kaplon and W. Dabrowski, "Fast CMOS Binary Front End for Silicon Strip Detectors at LHC Experiments", IEEE TNS 52 (2005) 2713.
- [4] J. Troska et al., "Optical readout and control systems for the CMS Tracker", IEEE Trans. Nucl. Sci., 50, No. 4 (2003) 1067.
- [5] R. Eusebi et al., "A diamond-based Beam Condition Monitor for the CDF experiment", Trans. NSS Vol.2 (2006) 709, San Diego, USA.
- [6] M. Brunisma et al., "CVD diamonds in the BaBar radiation monitoring system", Nucl. Phys. B150 (2006) 164.
- [7] Element Six Ltd., King's Ride Park, Ascot, Berkshire SL5 8BP, UK
- [8] CERN RD-42 Collaboration: "Development of Diamond Tracking Detectors for High Luminosity Experiments at the LHC "
- [9] G. Cervelli et al., "A radiation tolerant linear laser driver array for optical transmission in the LHC experiments", Proc. 7th Workshop on Electronics for LHC Experiments, CERN/LHCC/2001-034, pp 155-159. (2001)

[10] W. de Boer et al., "Radiation hardness of diamond and silicon sensors compared", Physica Status Solidi A204 (2007) 3004.

BEAMCAL READOUT SYSTEM REQUIREMENTS

By

Elena CASTRO, Hans HENSCHHEL

DESY Deutsches Elektronensynchrotron, Zeuthen, Germany

This document gives an overall view of the BeamCal system and reports on how the reading out of the data should be done considering the expected data rates and the purposes the calorimeter was designed for: Physics and fast feedback for the ILC machine operation. The numbers supplied here are estimative, however, they move around realistic values. The number of channels in the calorimeter, the number of layers used for analysis as well as the number of pads grouped for the fast readout, and the numbers of bits used for the digitization of signals may vary. The calculations of the data rates were done for the most recent approximations of last mentioned parameters. The report also introduces Front-End electronics concepts that could be used in the reading out. Lately, it was decided that a prototype of a calorimeter will be built. The details of the prototype are fixed and work is going on in order to get it available for test purposes. Here we also give a brief overview of possible prototype systems.

Key words: ILC BeamCal, Readout, Beam Parameter Feedback, LVDS, Gigabit Link, FONT

INTRODUCTION

BeamCal was designed with the purpose of being employed as a tool for Physics and for Beam Diagnostics. Depending on the task, the requirements for the granularity of the detectors and the data transfer speed together with the processing time will vary [1]. The calorimeter has to detect high energy electrons and photons produced e.g. in low transverse momentum QED processes such as Bhabha and photon-photon scattering. The latter is important in order to suppress this dominant background in many searches for new particles predicted in scenarios for physics beyond the Standard Model. In the polar angle covered by BeamCal, about 5 to 45 mrad, high energy electrons must be detected on top of wider spread depositions of low energy e^-e^+ pairs originated from beamstrahlung photon conversions. The bunch by bunch measurement of the total energy deposited by these pairs can be used to monitor the variation in luminosity and to provide a fast feedback to the beam delivery system. Moreover, the analysis of the shape of the energy flow can be used to extract the parameters of the colliding beams. This information can be further used to optimize the machine operation.

ILC BEAM TIMING AND BEAMCAL READOUT REQUIREMENTS

In the ILC the electron and the positron beams are structured in trains of ~ 3000 bunches of particles spaced by ~ 300 ns. The machine will be able to deliver five of these bunch trains per second with a dead time of ~ 200 ms (5Hz) between two consecutive trains [2]. This means that there will be 3000 collisions every 300ns followed by a pause of

199ms. The BeamCal will produce about 2Mbit of data for each bunch crossing. Using an immediate read out of all the information would lead to peak data rates in the range of ~ 2.5 Tbits/s, which would require a large number of high speed transmission lines. The required space, electrical power and costs make this solution to be discarded.

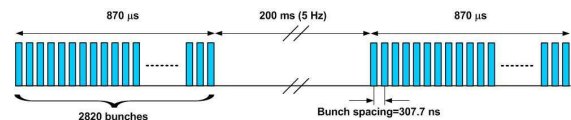


Figure 1. ILC nominal beam timing

However the 199ms gap allows to transfer these about 2Mbit of data per bunch crossing through a reasonable number of links, provided a fast and high volume storage buffer can be implemented right at the front-end - which is still a technological challenge.

In addition to these so-called ‘physics’ data the BeamCal is intended to deliver a very fast beam condition feedback which allows for correction of the luminosity steering during a bunch train, that is within a few microseconds after its start. MC simulations [3] showed that a selection of a few 100 channels from dedicated BeamCal layers is sufficient to derive the required information. Hence a low volume but dead-time free and low latency readout channel has to be established as well which transfers the data synchronously to the bunch clock.

THE BEAMCAL SYSTEM

The BeamCal system consists of two independent calorimeters: one for the Very Forward Region and another one for the Very Backward Region of the Large Detector Concept, both located

in $\pm 3.5\text{m}$ distance from the IP. Comprising an outer radius of 150mm the BeamCal covers an azimuthal angle from 5 to 45mrad.

The calorimeter will have a 'sandwich' structure of 30 layers of sensors. Each layer will be divided into 8 sectors with a granularity of ~ 160 channels per sector, this makes a total number of 1280 channels per layer and 38400 channels per calorimeter. Figure 2 shows a half barrel of parallel sensor layers and the simulated occupancy distribution of e^+e^- pair production. Figure 3 shows the layout of a prototype sensor wedge made from GaAs.

The granularity of the thirty layers of the BeamCal has to be high enough to resolve the developing showers originating from beamstrahlung photon conversions. On the other hand, a fine granularity increases the total number of channels and overall cost. It also determines the power dissipation and the produced data rates [3]. Some studies have been done on the impact of a change in the pad size on the electron reconstruction [4]. Following MC simulations the optimal efficiency leads to ~ 3000 channels per layer. For the purpose of luminosity feedback and beam tuning ~ 200 channels would be sufficient.

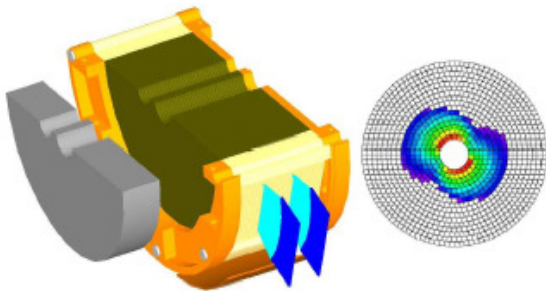


Figure 2. Structure of BeamCal.

Left: in grey is the graphite block in front of BeamCal; in orange is the support structure; in ginger are the tungsten absorber disks with sensor layers interspersed. Right: the pad structure of a sensor plane with depositions of e^+e^- pairs after one bunch crossing

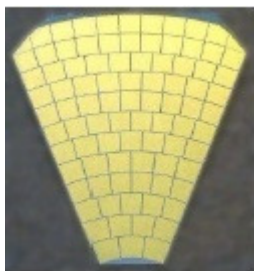


Figure 3. Prototype Sensor

A GaAs sensor wedge with an 87 pads structure.

DATA TRANSMISSION

The individual pads of a sensor are connected to the front-end ASICs (probably 32 channels each: preamplifier, shaper, ADC, buffer and readout

multiplexer) which are placed on a printed circuit board at the outer edge of the sensor (see Fig. 4). Transmission lines will feed the data along the calorimeter to a repeater/data concentrator block behind the last layer. Power and control lines will be traced in opposite direction. Merely at the concentrator there will be interconnections between adjacent sectors. The concentrator carries all long-distance interfaces to the off-detector data acquisition (optical links), control and supplies.

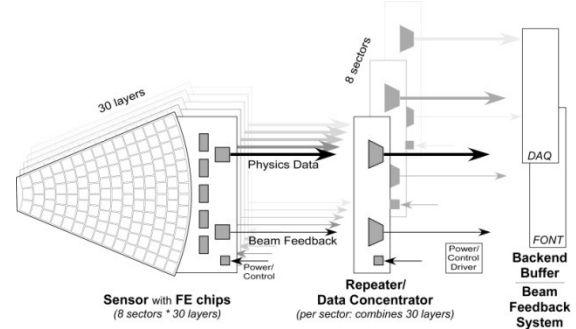


Figure 4. Data transmission scheme.

Several LVDS links will transmit the data from individual sensors to the data concentrator; few optical links will further link to the DAQ system and Beam Diagnostics Feedback system FONT. Power supplies and FE control lines are shown for completeness.

DATA RATES

For estimating the data rates to be handled by the BeamCal readout we consider a 10 bits digitization for the 'physics' data and 8 bits for the fast beam feedback data as suggested from MC design considerations. This corresponds to the ADC currently being implemented in the front-end electronics of LumiCal [5] and in a dedicated BeamCal concept by Stanford University which is still in the design stage [6].

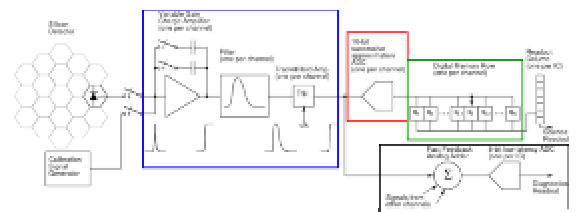


Figure 5. Block scheme of the SLAC BeamCal FE ASIC.

A 32-channel two-gain preamplifier/shaper stage is followed by a 10bit ADC and a 100kByte buffer memory. The analog sum of all 32 channels is digitized dead-time free at 8bit resolution.

All numbers presented hereafter bear on a single (forward OR backward) calorimeter only and prescind from considering parity bits or other protocol overhead; the kilo and mega prefixes are applied with the factor 1000 (instead of 1024).

Physics data

Due to the expected high occupancy, a full readout of all channels is needed (no sparsification possible); the rates are calculated using the 200ms intertrain pause as the time window for readout. For each bunch crossing (bx) a single sensor produces 160bit of data, that gives ~4.5Mbit for a bunch train, which have to be buffered at the very front-end! Reading out during the train intermittent interval leads to a data rate of 23Mbit/s. Subsequent layers should be multiplexed onto a common daisy chain or bus line – if one would use a single line per sector the data rate would reach 677Mbit/s. The overall amount of data to be read out is some 1Gbit.

Table 1. Data volumes and rates for ‘physics’ data.

‘Physics’ data	per sector	overall
pads per layer	160	
resolution	10bit	
data per sensor per bx	1600bit	
bunches per btrain	2820	
data per btrain	4.51Mbit	
intertrain pause	0.2s	
data rate per sensor	23Mbit/s	
layers per sector	30	
data per btrain	135.4Mbit	
data rate per sector	677Mbit/s	
sectors	8	
data per btrain		1.08Gbit
overall rate		5.4Gbit/s

For the transmission between layers and the data concentrator LVDS lines are foreseen at present due to their high speed by low power requirements and good noise rejection. In order to reduce the data rate on this link to values which can be handled by the LVDS standard every 10 layers (200Mbit/s) or 6 layers (125Mbit/s) may share a common line. Hence 3 (or 5) LVDS links per sector are necessary. For the transmission to the DAQ system optical links are considered, where a single Gigabit link per sector would be sufficient.

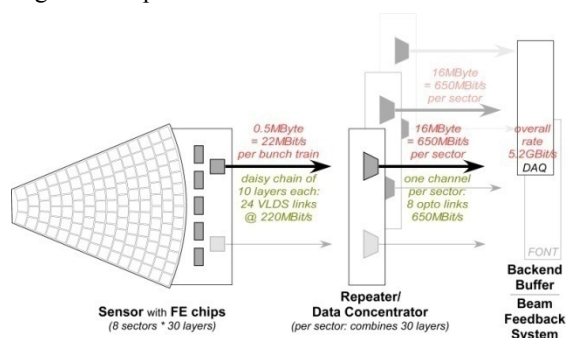


Figure 6. Data transmission – physics data.

Beam diagnostics data

The region of maximum energy deposition by the showers of the e^-e^+ pairs is at a depth of $5-6X_0$. The depositions on the sensor layers in this range have the best sensitivity for beam diagnostics [7].

As well the contribution of other layers to the diagnostics precision [8] and of a fine granularity is insignificant. Hence for the diagnostics data the small sensor pads may be grouped to coarse segments. The layout of these groups may consider electronics parameters (pcb design, crosstalk, balance of occupancy) since there is no physics preference for either a radial or angular clustering.

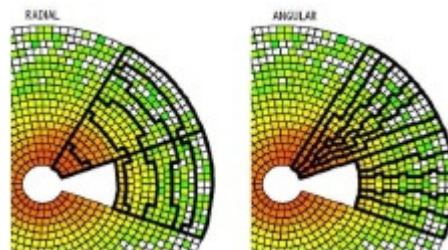


Figure 7. Clustering of pads for beam diagnostics.

Angular arrangement (right) helps to balance the occupancy and thus power load among the FE chips of a sensor; radial arrangement may reduce the effect of interchannel crosstalk.

The beam diagnostics data have to be read out dead-time free along with the bunch clock, that is at a 308ns repetition cycle (cf. Fig. 1). A single sensor produces on 5 channels 40bit of data, that gives a rate of 124Mbit/s. This fits well to the LVDS standard; however - exploiting the limits - one could also multiplex two consecutive layers onto a single transmission line per sector at ~250Mbit/s.

At the data concentrator the lines from all 8 (or at least from 4) sectors should be merged to an optical Gigabit link which sends the data to the beam parameter feedback system.

Table 2. Data volumes and rates for lumi feedback.

Diagnostics data	per sector	overall
channels per layer	5	
resolution	8bit	
data per sensor per bx	40bit	
layers per sector	2	
bunch cycle	308ns	
data per sector	80bit	
data rate per sector	248Mbit/s	
sectors	8	
overall data		640bit
overall rate		1.98Gbit/s

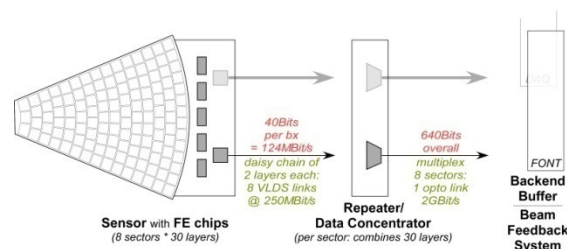


Figure 8. Data transmission – diagnostics data.

BEAMCAL PROTOTYPE

A BeamCal prototype will be built on the basis of available technologies. It will cover some 10 layers of a single sector with a granularity of ~ 100 channels. There will be a few 1000 channels in total.

Facing the fact that neither the sensor development nor the front-end electronics design will provide a 'final' solution within the next few years the prototype will make use of state-of-the-art technologies: Silicon or Gallium Arsenide as sensor material, readout chips from the prototypes generation currently under development in the collaboration. These will comprise 8 to 64 channels and may not include digitization or means for a low latency feedback channel!

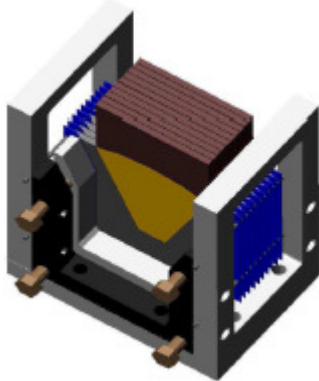


Figure 9. Prototype BeamCal Sector.

Frame with few layers of a single sector of the BeamCal design (tungsten absorber and sensor planes) – to be used for measurements in a test beam and as electrical and mechanical mockup.

REFERENCES

- [1] The Forward Calorimetry Collaboration (FCAL). Report for the ILC Detector R&D Panel Instrumentation of the Very Forward Region. ILC Detector R & D Panel Report, May 20, 2007.
- [2] T. Raubenheimer, Suggested ILC Beam Parameter Range. Available at <http://www-project.slac.stanford.edu/ilc/acceldev/beamparameters.html>
- [3] Ch. Grah, A. Saprnov. Fast Luminosity Measurement and Beam Parameter Determination. EUROTeV-Report-2007-006, October 15, 2007.
- [4] A. Elagin. The Optimized Sensor Segmentation for the Very Forward Calorimeter. Talk given at the International Linear Collider Physics and Detector Workshop and Second ILC Accelerator Workshop at Snowmass, 2005.

[5] M. Idzik, K. Swientek, Sz. Kulis. ADC measurements status. FCAL Collaboration Meeting at the Institute of Nuclear Physics PAN, May 6-7, 2008.

[6] A. Abusleme. BeamCal front-end design: challenges, solutions and techniques. FCAL Collaboration Meeting at the Institute of Nuclear Physics PAN, May 6-7, 2008.

[7] Ch. Grah, A. Saprnov. Beam Parameter Determination using Beamstrahlung Photons and Incoherent Pairs. EUROTeV-Report-2006-019, May 11, 2008.

[8] Ch. Grah, A. Saprnov. Beam Parameters Determination Using Beamstrahlung Photons and Incoherent Pairs. FCAL Collaboration Meeting at the Institute of Nuclear Physics PAN, May 6-7, 2008.

LASER ALIGNMENT SYSTEM FOR LUMINOSITY DETECTOR LUMICAL

Status Report

By

Leszek ZAWIEJSKI
W. DANILUK, E. KIELAR, J. KOTUŁA, K. OLIWA, W. WIERBA¹
and W. SŁOMIŃSKI²

(1) *Institute of Nuclear Physics PAN, Cracow, Poland*

(2) *Jagiellonian University, Cracow, Poland*

The status of work on Laser Alignment System for LumiCal detector is presented. LumiCal will be used for precisely luminosity measurement in International Large Detector, one of the detector concepts planned for future experiments on International Linear collider. The optical method for the position measurements of the LumiCal was tested using laboratory setup with two laser beams and CCD camera as the basic elements. The measurements achieved the accuracy $\pm 0.5 \mu\text{m}$ in X and Y direction and $\pm 1.5 \mu\text{m}$ in Z direction. The system is sensitive for temperature changes on the level $\sim 1 \mu\text{m}$ over 1°C . The possible extension of the system for a few meters distance measurements between the left and right part of LumiCal as well as for measurements of the displacement of the individual sensor layers inside LumiCal are discussed.

Key words: laser alignment system in measurements, CCD camera, filter, CMOS sensor, Renishaw optical head, ThorLab travel translation stage, temperature stabilization

INTRODUCTION

According to Reference Design Report [1], the International Linear Collider (ILC) project [2], requires high precision for both accelerator and detectors prepared for future experiments. In particular LumiCal detector is expected to give high precision in the integrated luminosity measurement $\Delta L/L$, better than 10^{-3} . It is based on the detection of Bhabha event rate. To fulfill this task it is necessary to build a detector with micrometer precision and have the running system – Laser Alignment System (LAS) for a precise measurement of the positions of LumiCal detector with accuracy of a few hundred micrometers and the displacement of its internal layers with accuracy of a few micrometers. The LumiCal detector contains two sandwich type calorimeters located symmetrically to the Interaction Point. The mechanical construction of each calorimeter consists of two half barrels embracing the outgoing beam pipe. Its internal structure is built with tungsten planes (as absorber), interspersed with layers of the silicon sensors as active material.

PERMISSIBLE DISPLACEMENTS

The absolute distance between two calorimeters (Fig. 1) should be known with accuracy better than $(60 - 100 \mu\text{m})$.

For single (Left/Right) calorimeter (Fig. 1) centered on outgoing beam, the displacement with respect to the beam pipe (Beam Pipe Monitor, quadrupol QD0) should be known with accuracy better than $(200 - 700 \mu\text{m})$.

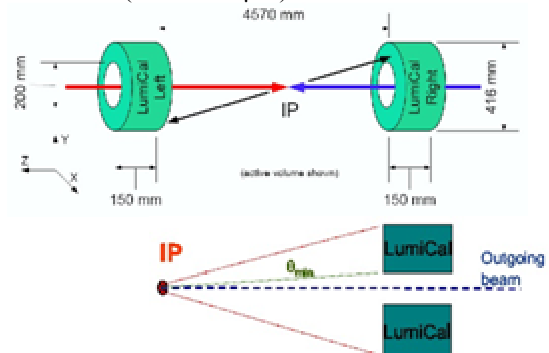


Figure 1. The elements of the LumiCal detector located in respect to Interaction Point (IP).

What is important for precisely luminosity measurement is the knowledge of the position of inner radius of active material which defines the minimal polar angle θ_{min} (Fig. 1). The expected error on the relative luminosity depends on this angle: $\Delta L/L \sim 1/\theta_{\text{min}}$. The required accuracy for inner radius is on the level $\sim 4 \mu\text{m}$. Figure 2 shows the mechanical structure of (Left/Right) calorimeter.

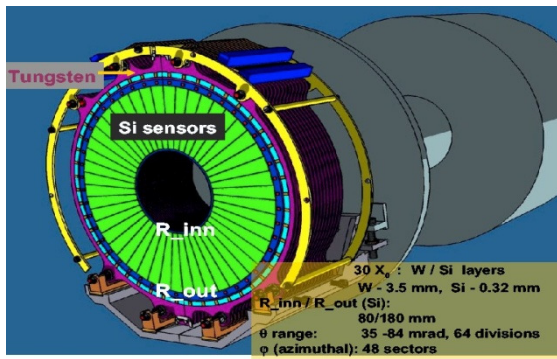


Figure 2. The structure of (L/R) calorimeter.

These limits on displacement were obtained based on the Monte Carlo simulation [3,4] where the changes in the relative luminosity were calculated as function of calorimeter displacement treated as the whole or by introducing some deformation in its internal structure.

METHOD AND LABORATORY SETUP

The principle of the method for short displacement measurements of the LumiCal is shown in Fig. 3.

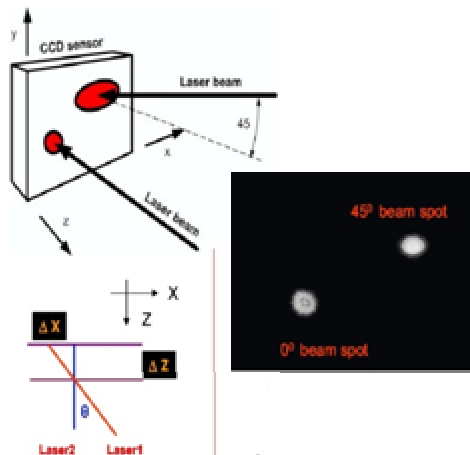


Figure 3. Simplified diagram of the setup with two laser beams which create the spots observed on CCD camera.

Two laser beams, one perpendicular and one under 45° degree, fall down on silicon CCD camera.

The coordinates centers of the spots created on the face of CCD camera at some distance between laser source and camera (Fig. 3) were calculated by special algorithm based on information obtained by readout of the pixels of CCD sensor. With these reference values one can calculate the relative displacements of a movable object to the reference position. The new experimental setup, which is shown in Fig. 4, was used to test the LAS and to find its accuracy and sensitivity to possible change of the temperature environment.



Figure 4. Picture of the new laboratory setup with CCD camera, Renishaw RG24 optical heads and two laser beams.

RESULTS

Figure 5 shows results of the measurements of the displacement in X (Y) and Z direction. The difference between the reference values for centers of the spots as calculated using algorithm and real positions (as obtained with Renishaw optical head linear encoders) gave $\pm 0.5 \mu\text{m}$ for X (Y) and $\pm 1.5 \mu\text{m}$ for Z directions.

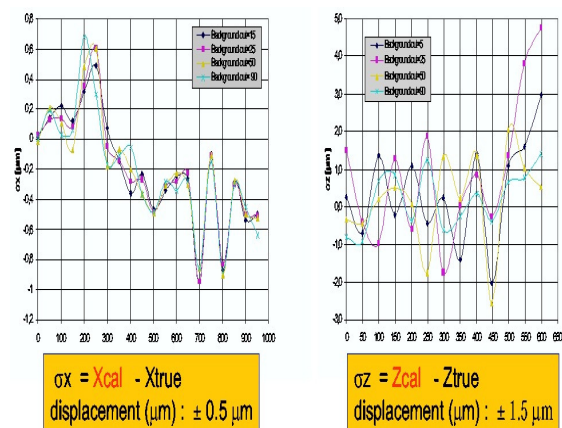


Figure 5. The accuracy measurements in X (Y) and Z directions.

The temperature effect on the displacement measurements was studied allowing the temperature to change in the range $\pm 5^\circ\text{C}$. The observed changes in spots positions did not exceed $1 \mu\text{m}$ on 1°C . Supplying the temperature stabilization on the level 0.1°C , the corresponding changes in spots positions were smaller than $0.5 \mu\text{m}$. Figure 6 shows an example of fluctuations in the positions of the spots in the long term (> 24 hours) measurements.

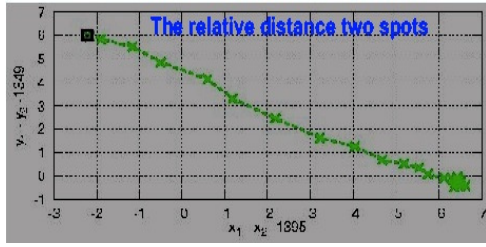


Figure 6. Observed changes in relative positions of both beam spots in long time period measurements with temperature stabilization $\Delta T \sim 0.1^\circ\text{C}$.

FURTHER DEVELOPMENTS OF LAS

Figure 7 shows the scheme of readout electronics for dedicated silicon sensor CMOS which allows for automatic (online) position calculations at compact shape of the system. Tests of the readout of the chain have just started.

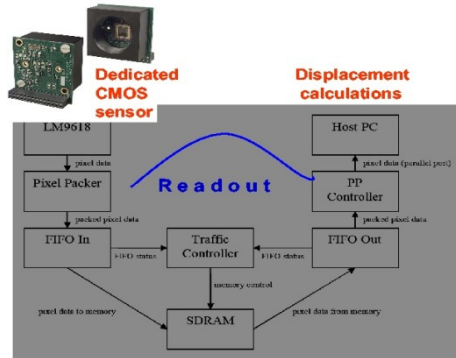


Figure 7. Schematic diagram of the readout for automatic positions calculation using dedicated CMOS sensor

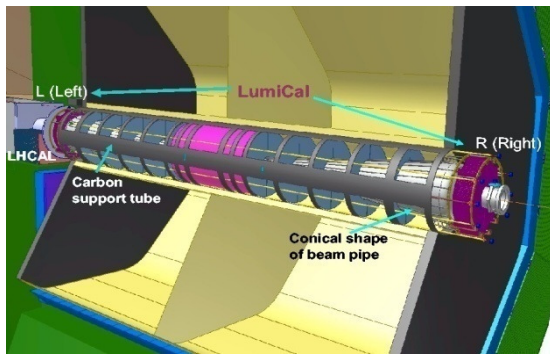


Figure 8. LumiCal in the structure of IL

LumiCal is part of ILD detector and several modifications of LAS will be necessary. There are several concepts which involve the use of other optical alignment systems like RASNIK [5] or the method based on interferometers and frequency scanned interferometry (FSI) system [6]. Figure 8 shows the location of LumiCal calorimeters inside the structure of ILD detector. The possible extension of LAS, which will allow for displacement measurement for Left/Right calorimeters in respect to beam pipe, is illustrated

in Fig. 9 (Right) and between them in Fig. 9 (Left). The system will include several laser beams/ CMOS sensors, mirrors, retro reflectors and interferometers. The common laser alignment system can be built with vertex detector VXD.

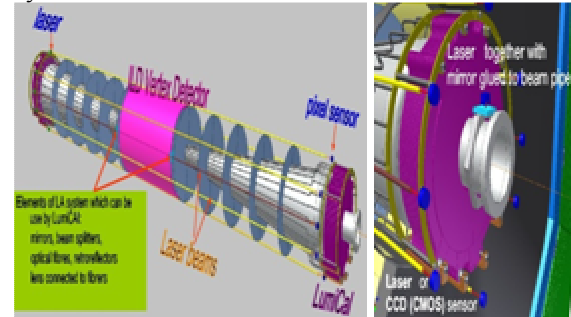


Figure 9. Left: Possible solution for absolute distance measurements between Left and Right calorimeters using laser beams or FSI system, created together with vertex detector VXD. Right: measurement position of single calorimeter with respect to beam pipe.

For measuring the displacement of the internal layers of the silicon sensors one of the proposed method can be used. The measurements that use half transparency special sensors glued to each silicon layers with infrared (IR) laser beam traversing all sensors are shown in Fig. 10 (Left).

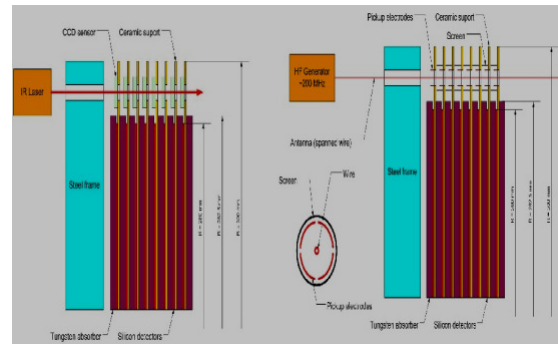


Figure 10. The possible solutions for measurements of the displacement internal sensor layers of the LumiCal detector.

Such type of alignment method for Forward tracker prototype with silicon microstrips will be studied in more details with test beam measurements [7] at the end of this year.

In the other method (Fig. 10, Right), which can be used for comparison with the previous method, the spanned wire is going through the holes in sensor planes and works as antenna. It picks up electrodes to measure the position of layer. The expected accuracy of this method will be on the level of $0.5 \mu\text{m}$.

ACKNOWLEDGEMENTS

This work is partly supported by The Polish Ministry of Science and High Education under

Agreement No. 141/6.PR UE/2007/7 and Commission of the European Communities under the 6th Framework Programme “Structuring the European Research Area”, contract number RII3-026126

REFERENCES

- [1] International Linear Collider, Reference Design Report, Vol. 4 Detectors, ILC-Report-2007-001.
- [2] International Linear Collider:
<http://www.linearcollider.org/cms/>
- [3] The FCAL Collaboration:
<http://www-zeuthen.desy.de/ILC/fcal/>.
- [4] A. Stahl, LC-DET-2005-004.
- [5] D. Goldstein, D.Salzberg, Nuclear Instruments and Methods in Physics Research A, 506 (2003) 92.
- [6] A. F. Fox-Murphy et al., Nuclear Instruments and Methods in Physics Research A 383 (1996) 229;
John R Green, PhD Thesis, “Development of a Prototype Frequency Scanning Interferometric Absolute Distance Measurement System for the Survey & Alignment of the International Linear Collider”, University of Oxford, 2007;
Hai-Jun Yang et al., “Frequency Scanned Interferometry for ILC Tacker Alignment”, arXiv:physics/0506197v1, June, 2005;
Hai-Jun Yan et al., Nuclear Instruments and Methods in Physics Research A 575 (2007) 395.
- [7] A. Savoy-Navarro, “JRA2-SITRA status”, a talk given at JRA2 plenary session, EUDET Annual Meeting, Amsterdam, 2008, Holland.

CLIC FORWARD REGION STUDIES STATUS REPORT

By

Ariella CATTAI¹, Lucie LINSSEN¹ and Andrey SAPRONOV²

(1) CERN – Geneva

(2) LNP JINR – Dubna, Moscow

The paper gives a status report on the background studies in the forward region of a future CLIC detector. For this purpose, a GEANT4 description of the forward calorimetry region and Mask was set up. Beamstrahlung events and their pair decay products simulated using the GUINEAPIG simulation package were tracked through the forward region. The study provides a first estimate of the electron, photon and neutron background levels of back-scattered particles in the tracker and calorimeter region of a CLIC experiment.

Key words: CLIC, forward region, background, beamstrahlung, GEANT4

SNAPSHOTS OF CLIC ACCELERATOR FEATURES

The Compact Linear Collider [1] aims to accelerate electrons and positrons at a centre-of-mass energy of 3 TeV and with Luminosity in the range of $10^{34} \text{cm}^{-2} \text{s}^{-1}$. The operation scheme of this novel machine foresees that the linacs accelerate the particles in one single pass and that the beams are dumped after the collisions. These features imply the use of very high electrical fields for acceleration (100 MV/m) and a very low repetition frequency for the collisions (50-100 Hz). Very high acceleration gradients are obtained with room temperature travelling wave structures at high frequency (12 GHz). The innovative idea of CLIC relies upon a two-beam acceleration concept: the main beam and the drive beam that runs parallel to it (Figure 1). The drive beam consists of high current (100 A) train-bunches with a repetition frequency of 12 GHz. By sending the drive beam through decelerating structures (PETS) it is possible to extract the RF power at 12 GHz and transfer it via waveguide to the accelerating structures of the parallel main beam.

High luminosity requires small beam size at the collision point. Therefore the beam dimensions of CLIC are 1 and 40 nm rms in the vertical and horizontal plane respectively. To achieve this challenge, CLIC exploits two damping rings in succession at the linac input, while, in the main linac itself, the RF accelerating structures are designed in order to control the wake fields induced by the bunches. These expedients will avoid the blow-up of the emittance. Finally, a sophisticated beam-delivery system with quadrupoles, stabilized to a vibration amplitude of less than 0.2 nm for oscillations above 4 Hz, will focus the beams down to the final dimensions.

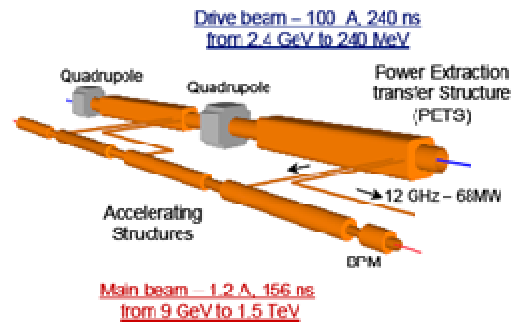


Figure 1. The CLIC two beams schema showing the Main Beam running in the accelerating structures and the Drive Beam with the Power Extraction & Transfer Structures.

GEOMETRY DESCRIPTION OF THE FORWARD REGION

Earlier studies of CLIC detectors [2] proved the need for an absorber for low-energy background particles in the forward region in order to protect the tracking and calorimeter regions of a CLIC experiment. In the 2004 studies this absorber, called Mask, was composed of a conical and a cylindrical component, placed on both sides of the interaction point and surrounding the z-axis (overall detector axis). For our recent CLIC studies, the Mask geometry has been introduced into the GEANT4¹ package in a flexible manner, such that its parameters can easily be varied. The model includes a flexible beam crossing-angle, initially fixed to 20 mrad. Within the GEANT4 description the LumiCal and BeamCal calorimeters have also been included, in analogy to the ILC forward region implementation. Both LumiCal and BeamCal are aligned to the outgoing beam axis. Figure 2 shows a schematic representation of the forward region

¹ GEANT4.9.0p01, physics list QGSP_BERT_HP

elements and a Dummy Cone that surrounds them. This volume allows having a quick glance at the background particles leaving the forward region. Figure 2 depicts also the definition of the Θ -angle, indicating the direction, and z , indicating the position of impact of the background particles onto the Dummy Cone.

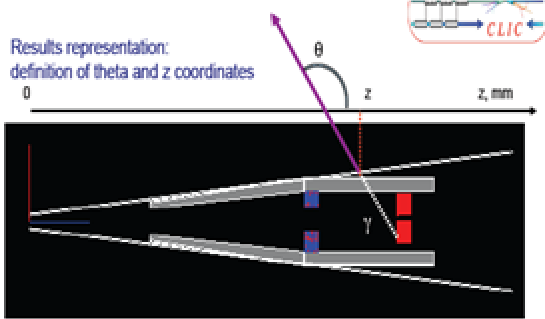


Figure 2. Schematic layout of the geometry description in GEANT4, comprising the Mask, LumiCal, BeamCal and Dummy Cone elements. The definition of angle Θ and position z refer to the orientation and location of the detected background particles in the Dummy Cone.

Initial geometry parameters have been chosen to do a first background study. These parameters are summarized in Tables 1, 2 and 3.

Table 1: Mask parameters in the initial study:

Description	Value	Unit
Starting point of the cone, z_{start}	1000	mm
Joint between conical and cylindrical part, z_{joint}	2270	mm
End-point of the cylindrical part, z_{end}	3350	mm
Inner angle of conical part, Q_i	85	mrad
Outer angle of conical part, Q_o	120	mrad
Material	tungsten	
Coating of polyethylene	0	mm

Table 2: LumiCal parameters in the initial study:

Description	Value	Unit
Front-face position, z_{start}	2270	mm
Inner radius	80	mm
Outer radius	Limited by mask	
Number of detector layers	30	
Tungsten absorber	3.5	mm
Silicon detector thickness	0.5	mm
Graphite front face cover	50	mm

Table 3: BeamCal parameters in the initial study:

Description	Value	Unit
Front-face position, z_{start}	3100	mm
Inner radius	20	mm
Outer radius	160	mm
Number of detector layers	30	
Tungsten absorber	3.5	mm
Diamond detector thickness	0.5	mm
Graphite front face cover	0	mm

BACKGROUND STUDIES

Beamstrahlung events with their coherent pair decay products, simulated using the GUINEAPIG simulation package, were tracked through the forward region elements. The study provides a first estimate of the electron, photon and neutron background levels in the forward region of a CLIC experiment and it gives an indication of the effectiveness of the Mask. Figure 3a shows the distribution of photon, e^+ , e^- and neutron particle hits in the Dummy Cone in the absence of the Mask. The number of events in Fig. 3 (top), and in all following figures, corresponds to 380000 beamstrahlung background pairs produced (1‰ of a single beam crossing). When the Mask is added the background spectrum is much reduced (Figure 3 (bottom)). One observes an effective reduction of photons and e^+ back-scattered from LumiCal and BeamCal, while the shielding of neutrons originating from BeamCal needs further improvement. Figure 4 shows the energy distribution of the background hits in the Dummy Cone. The distribution is dominated by energies below the 10 MeV level, which can normally be masked effectively.

To better understand the origin of the background particles, Figure 5 (top) shows a scatter-plot of the Θ, z coordinates of the hits on the

Dummy Cone in the absence of the Mask. It shows that a large number of background hits originate from the front and back faces of BeamCal. At low z -values, backscattered particles originate from the front face of BeamCal, passing through the inner opening of LumiCal. The backscattered particles from LumiCal itself are less numerous, because it has a much larger inner opening angle than BeamCal. Figure 5 (bottom) shows the same scatter plot with the Mask, indicating the effectiveness of the Mask.

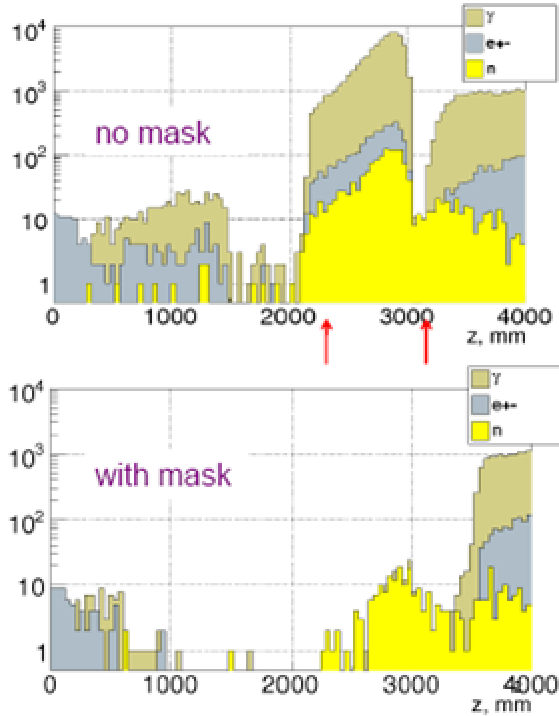


Figure 3. Distribution of photon, e^+ - and neutron background hits in the Dummy Cone in the absence of the Mask (top) and with the Mask (bottom).

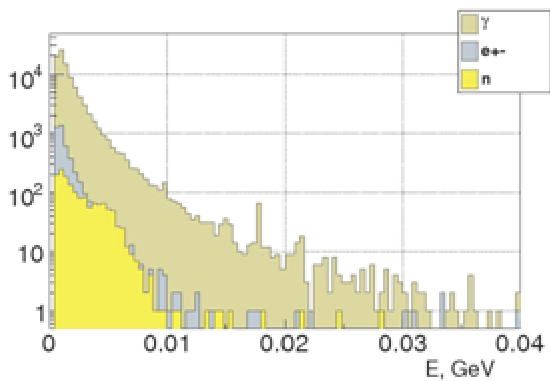


Figure 4. Energy distribution of photon, e^+ - and neutron background hits on the Dummy Cone in the absence of the Mask.

A further study was made to determine the background rates as a function of the parameters of the Mask. The conical part of the Mask mainly serves to protect the tracker region of the CLIC

detector. Figure 6 shows the number of background particles below $z=2100$ mm as a function of the Mask thickness $\Theta\Delta=\Theta_o-\Theta_i$. For $\Theta_i=85$ mrad the effect of the Mask thickness flattens off beyond ~ 5 mrad, showing that the Mask can be made thinner than anticipated in the conical region. The starting point of the cone, z_{start} , will be the subject for further studies to see whether the protection of the inner tracking regions can be improved.

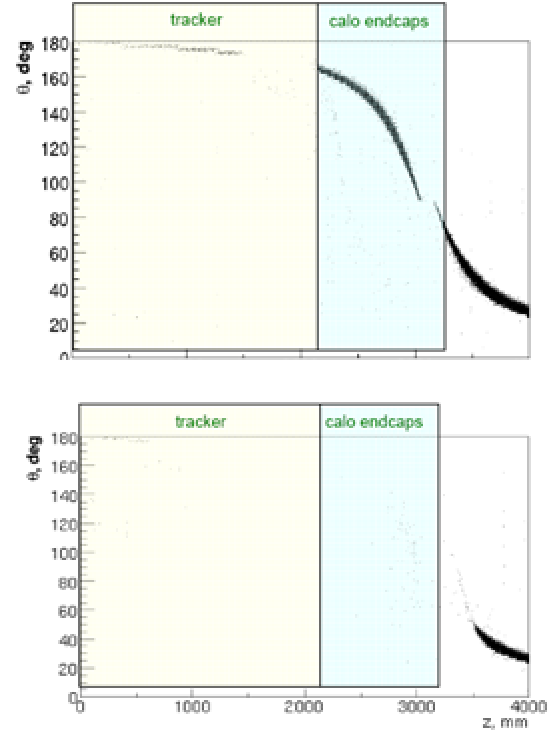


Figure 5. Θ - z coordinates of the background hits on the Dummy Cone in the absence of the Mask (top) and with the Mask (bottom).

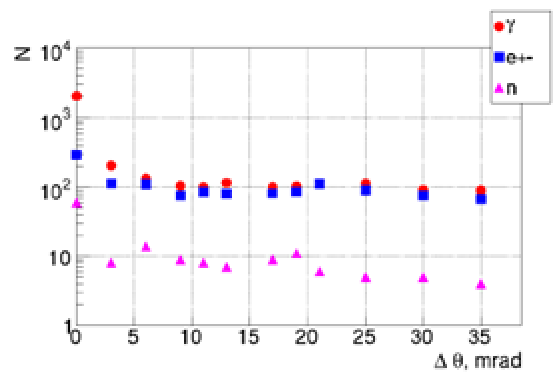


Figure 6: The number of background particles impacting on the tracker region of a CLIC detector as a function of the Mask thickness $\Theta\Delta=\Theta_o-\Theta_i$.

The cylindrical part of the Mask mainly serves to protect the calorimeter region of the CLIC detector. Figure 7 shows the number of background particles in the calorimeter region ($z=2100$ mm to $z=3350$ mm) as a function of the cylindrical Mask

thickness, expressed as $\Theta\Delta=\Theta_0-\Theta_1$, where $\Theta\Delta=35$ mrad corresponds to a Mask thickness of 80 mm.

[2] CLIC Physics Working Group, Physics at the CLIC multi-TeV linear collider, CERN-2004-005, Jun 2004

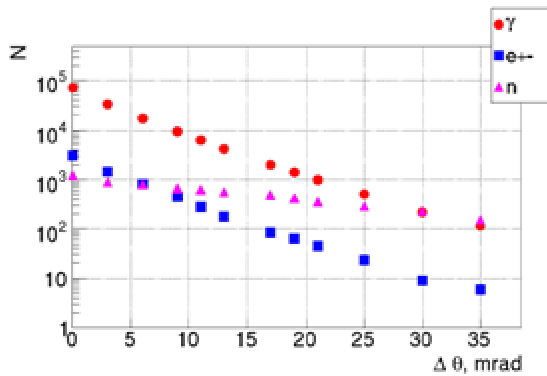


Figure 7: The number of background particles impacting on the calorimeter region of a CLIC detector as a function of the Mask thickness from 0 mm ($\Theta\Delta=0$) to 80 mm ($\Theta\Delta=35$ mrad).

The study indicates the need for a rather thick Mask. In the present study, the Mask had no polyethylene coating. Subject to further study, we expect that a polyethylene coating could help to reduce the overall thickness of the Mask in the conical region. In addition, a graphite coating on the front face of BeamCal could possibly provide a further reduction of the background rates.

OUTLOOK

This paper describes a very first study of background particles in the CLIC forward region. For this purpose the CLIC forward region elements were modeled in the GEANT4 package with a flexible geometry. Background beamstrahlung events, generated by the GUINEA PIG package, were tracked through the forward region. The background spectrum is dominated by photons, electrons, positrons and neutrons with energies up to a 10 MeV, originating from interactions of beamstrahlung relics in the forward region hardware. The study confirms the need for a forward Mask, and indicates that its thickness can be reduced to approximately 10 mm in the conical region. The cylindrical region of the Mask requires a larger thickness, subject to further studies involving the inner opening angle of BeamCal and its front face coating as well as the polyethylene coating of the Mask. The first results show the effectiveness of the simulation using the flexible detector geometry of the model. It will form the basis for more extended studies foreseen for the near future.

REFERENCES

[1] CLIC Study Team, A 3 TeV e+e- Linear Collider based on CLIC Technology, CERN 2000-008, Jul 2000

LUMINOSITY MEASUREMENT AND FORWARD PHYSICS AT ATLAS

By

Ljiljana SIMIĆ

Institute of Physics, Belgrade, Serbia

A summary of the measurements accessible with the forward detectors available in the ATLAS LHC experiment is presented. Luminosity determination using the LUCID and ALFA detectors is discussed in addition to measurement of diffractive processes that should be possible at low luminosity. A possible high luminosity upgrade strategy involving new forward proton detectors is also briefly reviewed.

Key words: luminosity, forward physics, ATLAS, LHC.

FORWARD DETECTORS IN ATLAS

With the center-of-mass energies of 14 TeV, the CERN Large Hadron Collider (LHC) will open up unprecedented phase-space for particle production spanning up to $\Delta\eta \sim 20$ units of pseudorapidity (Fig. 1). The total LHC pp cross section predicted by the COMPETE Collaboration is: $\sigma_{\text{tot}}(\text{LHC}) = 111.5 \pm 1.2(\text{stat})_{-2.1}^{+4.1}(\text{syst})$ mb [1]. Half of this large value corresponds to very soft physics including elastic pp collisions. Many interesting scattering processes mostly mediated by colorless exchanges (Pomeron, photon or gluon) are characterized by particles (protons) emitted at very low angles with respect to the beam and/or an (often exclusive) system produced at more central rapidities. In this report we present a summary of the program accessible with the forward detectors in ATLAS experiment.

ATLAS is general purpose detector [2] at the LHC with full ϕ coverage and a excellent central coverage in the E_{cm} , reaching pseudorapidity $|\eta| < 2.5$ for inner tracking detector, $|\eta| < 4.9$ for hadronic and electromagnetic calorimeters and $|\eta| < 2.7$ for muon spectrometer. Although, ATLAS see most of the charged particles from final states, still a significant amount of them with $|\eta| > 5$, escapes detection. Moreover, most of the energy flow of final state is in very forward $|\eta|$ regions, well beyond their reach (Fig. 1). To extend the detection capability of the ATLAS, additional forward detectors, LUCID, ZDC and ALFA will complement ATLAS coverage. This detectors are designed for various (relative and absolute) luminosity measurements, but are in addition foreseen for forward physics study. When ordered by their distance from the ATLAS interaction point (IP) the first system is LUCID (LUMinosity measurement using Cherenkov Integrating Detector) located at 17 m away from the IP on both sides. The second system is Zero Degree

Calorimeter (ZDC), inserted in the transverse aperture of the ATLAS neutral particle absorbers, at about 140 m from the IP on each side. The most remote system is the ALFA (Absolute Luminosity for ATLAS) system located at a distance of 240 m from IP.

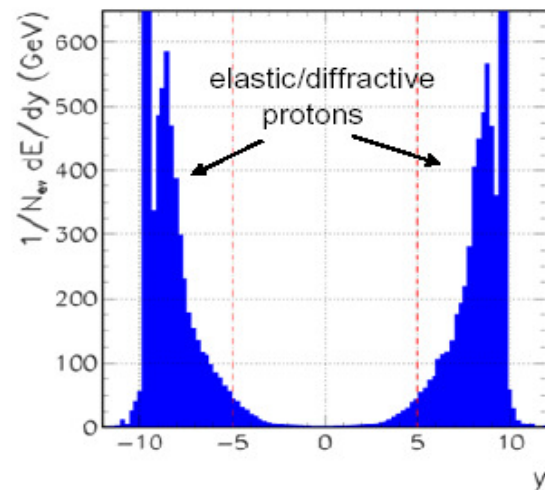


Figure 1. Energy flow at the LHC: most of the energy is deposited between: $8 < |y| < 9$ ($y \approx \eta$ for negligible masses i.e. for $E \approx p$).

LUCID [2] is the main luminosity monitor in ATLAS. Its main purpose is to detect inelastic pp scattering in the forward direction, both in order to measure the integrated luminosity and for on-line monitoring of the instantaneous luminosity and beam conditions. Potentially LUCID could also be used for diffractive studies e.g. as a rapidity gap veto. The LUCID detector provides coverage of $5.8 < |\eta| < 6.1$. It consists of two arrays of polished aluminium tubes that surround the beam pipe. Each tube is 15 mm in diameter and filled with C_4F_{10} gas at about 1.2 bar pressure. The arrays are placed around the beam pipe at 17 m of IP, on both sides. When a charged particle is crossing the tube, the Cherenkov light is emitted at about 3° with respect to the impinging charged track direction. Light is

collected at each tube end by either a PMT or an optical fiber-bundle leading to a PMT, after few reflections on the tube internal surface. The key characteristics of the detector are: the Cherenkov threshold of 10 MeV for electrons and 2.8 GeV for pions to limit the background: the pointing geometry allowing particles coming from the IP to produce more light than background particles coming from the LUCID sides; the aluminium reflectivity and the radiation hardness. In addition, the lack of Landau fluctuations in the number of Cherenkov photons makes the particle counting robust, while a sufficient time resolution allows to measure individual bunch crossing which occur every 25 ns .

ZDC [2] will measure neutral particles at a 0 polar angle. It covers $|\eta| > 8.3$ region for neutral particles. ZDC has a central role in the ATLAS heavy ion program where it is used to measure the centrality of the collisions, the luminosity as well as to provide the triggers. During the start-up phase of the LHC (pp collisions with luminosities well below $10^{33} \text{ cm}^{-2} \text{ s}^{-1}$), the ZDC will enhance the acceptance of ATLAS central and forward detectors for diffractive processes and provide an additional minimum bias trigger for ATLAS. The ATLAS ZDC consists of six tungsten/quartz calorimeter modules where the light from the quartz fibers is read-out by PMTs. In addition the ZDC is equipped with horizontal quartz rods, parallel to the beam in order to determine the location of the showers in the plane perpendicular to the beam.

ALFA [3] consists of scintillating fiber trackers located inside Roman pots which allow the detectors to approach the beam inside the LHC beam pipe and the main purpose of ALFA is to measure elastic proton scattering at low angles. The aim is to determine absolute luminosity in ATLAS, but also other physics studies are foreseen such as measuring the total pp cross section, measuring elastic scattering parameters and potentially measurement of tag protons for diffractive studies.

LUMINOSITY MEASUREMENT

A precise determination of the luminosity L will be crucial experimental issue at the LHC, since it represents one of the main uncertainties for cross-section measurement for various processes. If all systematics in cross-section measurement is under control, any deviation from the predicted value will be one of the first signs of new physics.

There are two kinds of luminosity measurements: an absolute value which serves as a point of reference, and relative which allows to follow values of the luminosity accumulated as a function of time. Absolute value of the luminosity can be determined from the measurement of the LHC beam parameters:

$$L = \frac{f \sum_{i=1}^{k_b} N_{1i} N_{2i}}{4\pi\sigma_x^* \sigma_y^*}$$

where f is revolution frequency, k_b is the number of bunches, N_{ji} is the number of protons in bunch i of beam j and σ_x^* and σ_y^* are the transverse beam dimensions at the IP. Previous experience at hadron colliders suggests that a 5-10% precision (20-25% in early running phase) may be reached from the measurement of the machine parameters. However, at the LHC such a precision would already dominate the systematic error in the determination of cross-section and other main fundamental quantities.

Besides the machine parameters the luminosity can also be determined by measuring the rate of a clean and well-known process. Both QED and QCD processes will be available at LHC for this task, namely $pp \rightarrow pp\mu^+\mu^-$ (exclusive muon pair production by double photon exchange) and $W \rightarrow l\nu$, or $Z \rightarrow l^+l^-$. The former process will be limited in recorded statistics (cross section $\sim \mu\text{b}$), whereas the latter requires a good control of the proton PDF which makes it unclear if the achievable precision on luminosity will exceed the level of 5%. ATLAS preliminary results show that overall uncertainty in W cross section measurement of 5% and in Z cross section measurement of 3% can be achieved with data of 50 pb^{-1} [4]. However, the goal of ATLAS is to reach precision for absolute luminosity measurement of 2 to 3%. This could be achieved by using the optical theorem. By measuring elastic pp scattering at very small angles ($dN_{el}/dt|_{t=0}$) together with the total pp cross-section (σ_{tot}), both the luminosity and the total cross-section can be determined via:

$$L = \frac{1}{16\pi} \frac{(N_{el} + N_{inel})^2 (1 + \rho^2)}{dN_{el}/dt|_{t=0}}$$

$$\sigma_{tot} = \frac{16\pi}{(1 + \rho^2)} \frac{dN_{el}/dt|_{t=0}}{(N_{el} + N_{inel})^2}$$

where ρ represents the real-to-imaginary part ratio of the elastic amplitude in the forward direction. In order to keep extrapolation errors small, this method requires the measurement of very small proton scattering angles (down to about $10 \mu\text{rad}$ at LHC) or equivalently, very small square of four momentum transfer $|t| \approx (p\theta)^2$, where p represents the proton momentum and θ its scattering angle ($t_{min} \approx 10^{-3} \text{ GeV}^2$ at LHC). Dedicated detectors close to the beam-line and specific beam optics are needed for this measurement together with a precise determination of the inelastic rate that in turn requires a good coverage of the full pseudorapidity region which is not ideal for ATLAS.

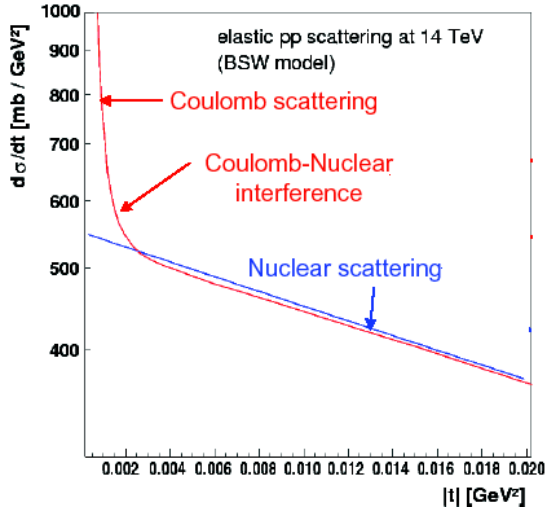


Figure 2. Four-momentum transfer $|t|$ distribution for elastic pp scattering.

On a longer time scale ATLAS aims to extract the absolute luminosity from the t -distribution of the elastic pp scattering in the Coulomb interfering (CNI) region (Fig. 2), where the strong amplitude equals the electromagnetic one. In this case, both the luminosity and the total cross section can be extracted from the elastic rate dependence on the momentum transfer without the inelastic rate measurement:

$$\frac{dN}{dt}(t \rightarrow 0) = L\pi \left(\frac{-2\alpha}{|t|} + \frac{\sigma_{\text{tot}}}{4\pi} (i + \rho) e^{-b|t|/2} \right)^2$$

From a fit to the data in CIN region it is possible to determine directly the total cross section σ_{tot} , the ρ and b (nuclear slope) parameter, as well as the absolute luminosity. However, this measurement requires to go down to $|t| \sim 6.5 \cdot 10^{-4} \text{ GeV}^2$, or $\theta \sim 3.5 \mu\text{rad}$. This technique was used by the UA4 experiment at the CERN SPS [5] and precision of the order of 3% was reached. However UA4 experiment needed to go down to $120 \mu\text{rad}$ whereas the ATLAS needs to go down to $3.5 \mu\text{rad}$. It makes this measurement very challenging. This measurement requires a special high β^* optics, detectors to be installed at about 1.5 mm from the LHC beam axis, a spatial resolution of these detectors well below $100 \mu\text{m}$ and insensitve area at the edge of the detector less than $30 \mu\text{m}$. The solution to achieve this measurement is to install Roman pot detectors which can go close to the beam when the beam is stable.

The relative luminosity measurement as a function of time will be done in ATLAS using the LUCID detector. This detector is mainly sensitive to primary particles (much more light is coming from primary particles than from secondary or soft particles). The LUCID detector allows to obtain a linear relationship between the luminosity and the number of tracks counted in the detector which leads to an easy measurement of the luminosity. For

an absolute luminosity measurement, LUCID must be calibrated. The calibration is planned to proceed in steps of successively higher accuracy. Initially the calibration will rely on calculations based on the LHC machine parameters. It will soon become possible to use standard candle processes instead, such as W and Z events. Ultimately, the most accurate calibration will come from the ALFA Roman-pot detectors which will measure elastic scattering in the Coulomb interference region. With this final calibration, LUCID will measure the luminosity with an accuracy of better than 5% .

DIFFRACTIVE MEASUREMENTS IN ATLAS

ATLAS will use forward detectors to measure the total and elastic cross section and carry out an absolute luminosity measurement. In addition, ATLAS also plans to implement a program on measurement of soft and hard diffractive processes [6].

Diffractive processes cover the class of inelastic interactions that have large rapidity gaps ($\Delta\eta > 4$) without hadronic activity, where one or both protons emerge intact in the final state. Such event topologies, with reduced QCD radiation, imply colorless exchange mediated by two or more gluons in a color-singlet state (a Pomeron).

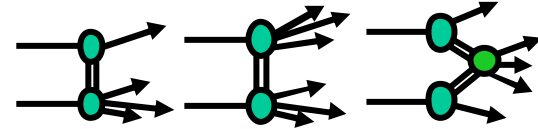


Figure 3. Diffractive processes: single (left), double (middle) or central (double-Pomeron-exchange) diffraction (right).

Depending on the number of Pomerons and relative separation, one further distinguishes single (SD), double (DD) or central (double-Pomeron-exchange, DPE) diffractive processes (Fig. 3). The diffractive system has a mass equal to $M^2 \approx s\zeta_1$ ($M^2 \approx s\zeta_1\zeta_2$) for single (central) diffractive events, and the size of the rapidity gap of the order $\Delta\eta \approx \ln(s/M^2)$ where ζ is the longitudinal momentum fraction, $\zeta \approx 1-x_F$, ($x_F = 2p_L/\sqrt{s}$) and \sqrt{s} is the center-of-mass energy of the colliding protons. At the LHC, typical values of $\Delta\eta$ are about 5.3 for $M=1 \text{ TeV}$ and 9.9 for $M=100 \text{ GeV}$. Class of diffractive processes that contains high-mass or large- p_T state ($X = q\bar{q}$, jets W , Z) in the diffractive final state is called hard diffractive scattering due to the presence of a hard (short distance) scale. The occurrence of hard scattering can be related to a partonic structure and a variety of measurements can be used to provide constraints on parton densities. Also, of particular interest are hard exclusive DPE processes where the centrally produced system can be a new heavy particle (Higgs, for example).

In the ATLAS experiment the following diffractive measurements are foreseen at low luminosity :

- Soft single diffraction is characterized by a produced diffractive system separated by a large rapidity gap, or lack of hadronic activity from an outgoing proton. The cross section for this process is presented in terms of the fractional momentum lost by the proton, $\zeta \approx 1-x_F$, ($x_F = 2p_L/\sqrt{s}$) and the momentum transfer, t ($d\sigma_{SD}/dt dM$). The outgoing proton in soft single diffraction exchange can be tagged and measured during special LHC runs by the ALFA detectors. The acceptance is approximately 50% for $\zeta \approx 0.01$ and 10% for $\zeta \approx 0.1$. It is expected that at a luminosity of $10^{27} \text{ cm}^{-2} \text{ s}^{-1}$ there will be between 1.2 and 1.8 million events recorded in 100 hours of data acquisition.

- Single diffractive di-jet production can be selected by identifying gap, by requiring that a forward detectors register little hadronic activity. LUCID, ZDC and ATLAS forward calorimeter (FCAL) can be used as a part of a rapidity gap requirement for diffractive analysis. Di-jet production by SD should be measurable with 100 pb^{-1} of data.

- Central exclusive production (CEP) is defined as the process $pp \rightarrow p \oplus X \oplus p$, where X is fully measured diffractive state such as jet-jet, H, WW, ll... and \oplus represents large rapidity gap ($\Delta\eta > 4$). All of the energy lost by the protons goes into the production of a hard central system, X. Thus the final state consist of two outgoing protons, a hard central system and no other activity. There is a significant theoretical uncertainty on the CEP cross section and measurement with ATLAS will help to constrain the calculation.

- Gaps between-jets arise from a $2 \rightarrow 2$ scatter via a color singlet exchange and has previously been measured at HERA and the Tevatron. The process was observed to be a strong interaction and possible candidate for the color singlet exchange is the BFKL Pomeron,. This however remains to be experimentally verified. A prediction of BFKL is that the fraction of events with little activity between the jets (the gap fraction) should rise with the separation of the jets. The rise of the gap fraction was not observed at the Tevatron, for example, because the center of mass energy was too small. An improved measurement should be possible at the LHC due to the increased center of mass energy. In principle ATLAS should be able to measure the gap fraction up to 9.95.

At high luminosity, the rapidity gap method can not be used to select diffractive events because particles from pile-up will fill the gaps. A diffractive physics program can be continued by installing new forward proton detectors at 220 m (radiation hard detectors) and at 420 m (proton tagging detectors) from IP. This will open

possibility of searching for new physics CEP such as Higgs boson production in SM and MSSM. The main benefit arises when both protons are tagged and measured because mass of the centrally produced system can be calculated by $M^2 = \zeta_1 \zeta_2 s$. Thus for exclusive resonance production, a mass measurement can be made regardless of the decay products of the produced particles. Furthermore, forward proton tagging allows measurement of photon induced processes such as W-pair production via the anomalous quartic gauge coupling $\gamma\gamma WW$.

REFERENCES

- [1] COMPETE Collaboration, Phys. Rev. Lett. **89** 201801, 2002.
- [2] ATLAS Collaboration, The ATLAS experiment at the CERN Large Hadron Collider, JINST 3 S08003, 2008.
- [3] ATLAS Collaboration, ATLAS Forward Detectors for Measurement of Elastic Scattering and Luminosity CERN/LHCC/2008-004, ATLAS TDR 18, 2008.
- [4] ATLAS Collaboration, ATLAS Experiment, Expected Performance of the Detector, Trigger and Physics, CERN-OPEN-2008-020, Geneva, 2008, to appear.
- [5] UA4 Collaboration, Phys. Lett. **B198**, 583 1987.
- [6] ATLAS Collaboration ATLAS Detector and Physics Performance, CERN/LHCC/99-15, ATLAS TDR 15, 1999.

VERY FORWARD REGION IN BELLE: PHYSICS IMPACT AND OPPORTUNITIES

By

Peter KRIŽAN^{1,2}

(1) University, Faculty of Mathematics and Physics, Ljubljana, Slovenia
(2) J. Stefan Institute, Ljubljana, Slovenia

The importance of missing energy studies with the Belle detector is presented, and illustrated with the first measurement of the branching fraction for the purely leptonic $B \rightarrow \tau \nu$ transition. We then discuss a possible improvement in the hermeticity of the spectrometer by adding a detector in the very forward region. The candidate detector is very similar to the silicon sensors of the forward calorimeter at the linear collider.

Key words: B mesons, leptonic B decays, Belle, Super B factory, linear collider, forward calorimeters

INTRODUCTION

The two B factories, PEP-II with BaBar and KEKB with Belle, have been a real success story. They carried out precision measurements of CKM matrix elements and angles of the unitarity triangle, observed direct CP violation in B decays, measured rare decay modes by fully reconstructing the other B meson, and observed D mixing. They measured CP violation in $b \rightarrow s$ transitions and thus probed for new sources of CP violation; the study of forward-backward asymmetry in $b \rightarrow s$ transitions has by now become a powerful tool to search for physics beyond SM. Last but not least, they observed a long list of new hadrons, some of which do not seem to fit into the standard meson and baryon scheme.

B DECAYS WITH MORE THAN ONE NEUTRINO IN THE FINAL STATE

A particular challenge are the studies of B meson decays with more than one neutrino in the final state. An example of such a process is the leptonic decay $B \rightarrow \tau \nu$ which is then followed by the decay of the tau lepton with one or two more neutrinos. In the Standard model (SM) this transition proceeds via W annihilation. The measured branching fraction can be used to extract the value of $f_B |V_{ub}|$, which, in turn, can be used to determine f_B and to compare its value to the value as derived from lattice calculations. The measured branching fraction can also be used to set limits on the charged Higgs mass and $\tan\beta$.

Such rare processes are searched for in the following way [1]. First, one of the B mesons is fully reconstructed in a number of exclusive decay channels like $B \rightarrow D^{(*)}\pi$. The remaining particles in the event are the decay products of the associated

B (Fig. 1). In the $B \rightarrow \tau \nu$, $\tau \rightarrow \pi \nu$ or $\tau \rightarrow \mu \nu \nu$ decay sequence, only one charged particle is detected.

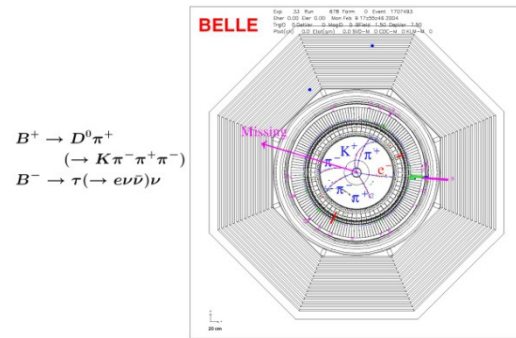


Figure 1. Event candidate for the $B \rightarrow \tau \nu$ transition.

To exclude background events with additional neutral particles (π^0 or γ) in the final state, we use the remaining energy in the calorimeter which is not associated with reconstructed charged tracks (Fig. 2). In this measurement we greatly profit from the excellent hermeticity of the Belle spectrometer. The measurement yields

$$BF(B \rightarrow \tau \nu_\tau) = (1.79_{-0.49}^{+0.56+0.46}) \times 10^{-4}$$

from which we can determine the B meson decay constant, f_B , using the SM relation,

$$BF(B \rightarrow \ell \nu)_{SM} = \tau_B \frac{G_F^2}{8\pi} |V_{ub}|^2 f_B^2 m_B m_\ell^2 \left(1 - \frac{m_\ell^2}{m_B^2}\right)$$

The resulting value,

$$f_B = 229_{-31}^{+36+34} \text{ MeV}$$

is in good agreement with an unquenched lattice QCD prediction, $f_B = (216 \pm 22) \text{ MeV}$ [2]. Physics beyond the SM, such as supersymmetry or two-Higgs doublet models, could modify this branching

fraction through the introduction of a charged Higgs boson [3]. The ratio of the branching fraction to the SM value,

$$r_H = \frac{BF(B \rightarrow \tau\nu)}{BF(B \rightarrow \tau\nu)_{SM}} = \left(1 - \frac{m_B^2}{m_H^2} \tan^2 \beta\right)^2$$

depends on the parameters of the charged Higgs particle. From the measured value as given above and assuming the lattice QCD value [3] of f_B , limits can be derived on the charged Higgs particle mass and the ratio of vacuum expectation values, $\tan\beta$. As shown in Fig. 3, this measurement (green) is able to exclude a sizable part of the parameter space. With a hundred times larger data sample, such an analysis could indeed yield an almost complete exclusion plot in charged Higgs mass and $\tan\beta$ plane (bottom plot in Fig. 3).

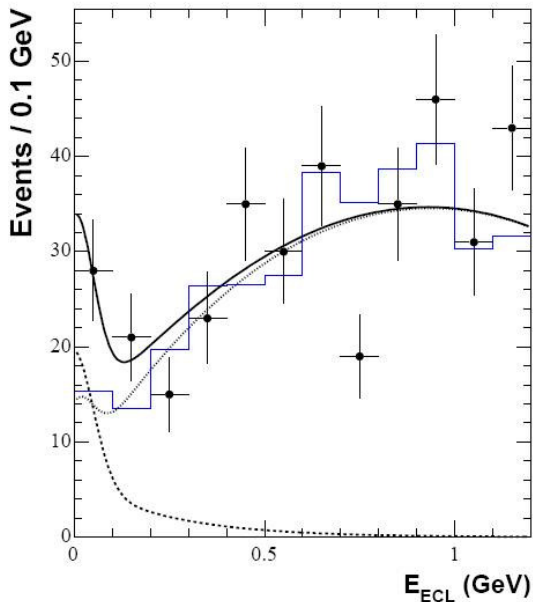


Figure 2. Residual energy as recorded in the calorimeter for the $B \rightarrow \tau\nu$ decay candidates. Signal events correspond to the peak at zero deposited energy.

MOTIVATION FOR A SUPER B FACTORY AND DETECTOR UPGRADE

To search for departures from the Standard model, a two orders of magnitude larger sample of B meson decays is needed. A sizable upgrade is therefore needed both of the accelerator complex as well as of the detector [4]. As a part of the upgrade of the Belle detector (Fig. 4), we are also considering the installation of a tracking device in the very forward region of the spectrometer (Fig. 5). Such a detector would improve the hermeticity of the spectrometer, which, in turn, would help reduce the background level in studies of rare B meson decays to final states with more than one neutrino.

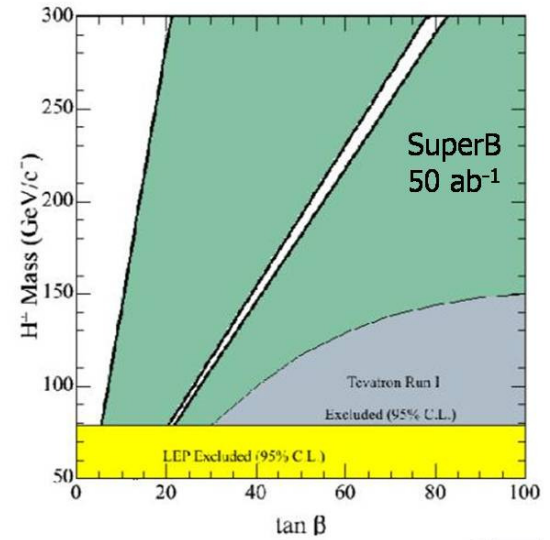
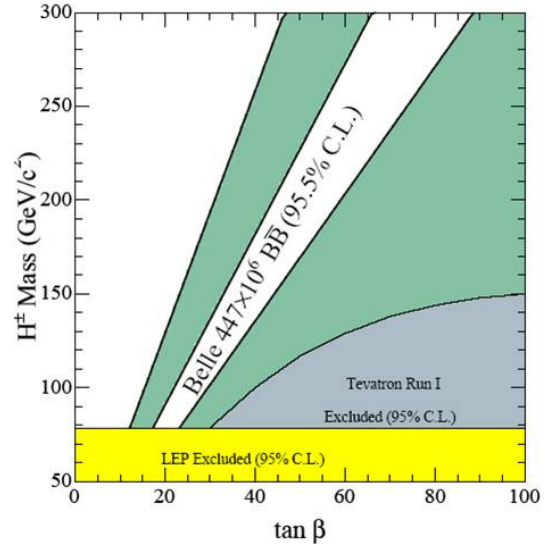


Figure 3. Limits on the values of the charged Higgs mass and $\tan\beta$ as derived from the measured branching fraction for the $B \rightarrow \tau\nu$ decay (top), expected accuracy with a sample corresponding to a luminosity of 50ab^{-1} .

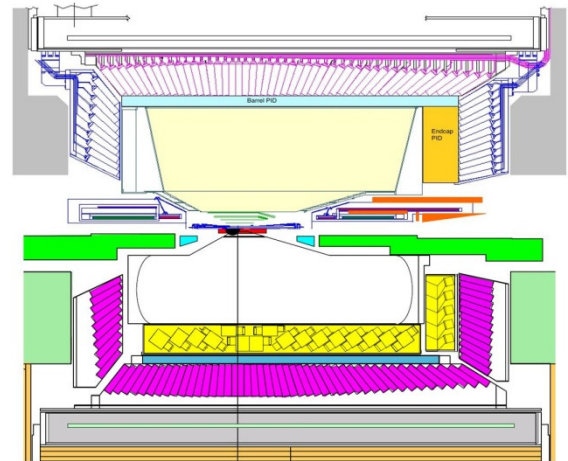


Figure 4. Comparison of the detector layout for SuperBelle (top half) and Belle (bottom).

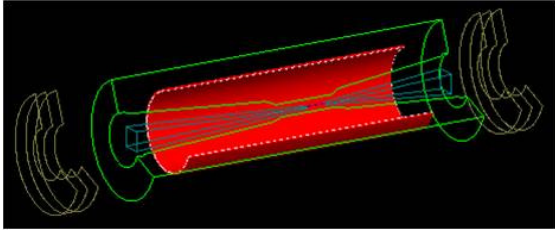


Figure 5. A schematic layout of the super-forward (and backward) tracking system.

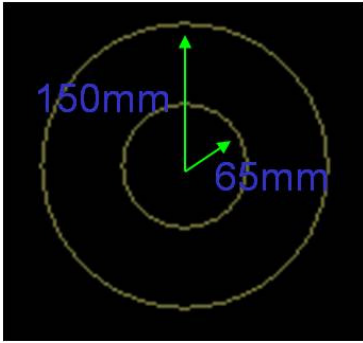


Figure 6. A schematic layout of the sensors for the super-forward (and backward) tracking system.

IMPACT OF THE VERY FORWARD DETECTOR

Another interesting very rare process is the decay $B \rightarrow K^{(*)} \nu \bar{\nu}$ with the experimental signature very similar to the $B \rightarrow \tau \nu$ decays. This decay is used as the benchmark channel to determine the parameters of the very forward detector, and to evaluate its impact.

In a simulation study [5], we have assumed that the counter is a silicon based tracking device, consisting of three layers at the positions $z=705\text{mm}$, 735mm and 765mm with respect to the interaction point along the more energetic (electron) beam. As sensors, disk shaped silicon detectors were assumed with $2\text{mm} \times 2\text{mm}$ large pixels (Fig. 6). The counter was used as a veto counter, i.e., events with a track candidate consistent with originating in the interaction region within very rough margins were excluded from the further analysis. In this way, a significant background reduction by 32% was observed, while the signals events suffered no loss (Fig. 7). This result seems to be quite promising. We note, however, that the study has to be refined by including realistic assumptions on the sensor granularity, material in front of the counter, supporting structures and available space.

The sensor as assumed in the simulation study resembles very much the sensor (Fig. 8) of the LumiCal counter for the linear collider detector [6]. A simulation study is needed to investigate to which extent such a sensor could be applied without major changes in the design. Of course, the read-out electronics requirements are quite different at a B factory, and the radiation load has to be carefully estimated.

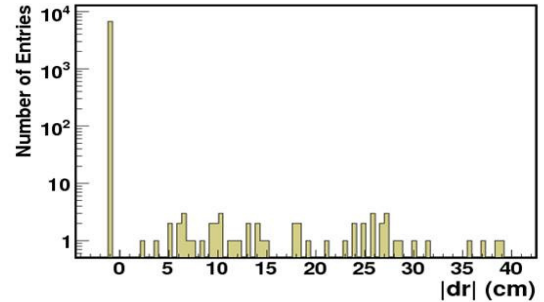
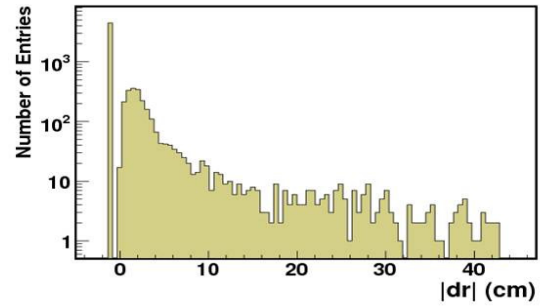


Figure 7. Impact parameter distribution for the background (top) and signal events (bottom). Events with at least one track with $|dr| < 12\text{cm}$ were rejected in the analysis.

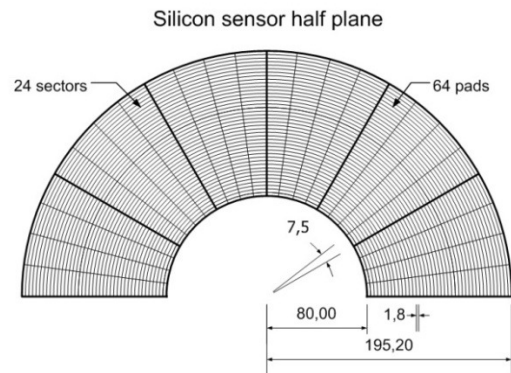


Figure 8. The present version of the silicon sensor for the LumiCal at the linear collider detector [6].

SUMMARY

At Belle, studies of events with missing energy in the calorimeter have turned out to be a promising way to investigate very rare transitions, which could show indications of physics processes beyond the Standard model. For a significant improvement in the sensitivity, the B factory has to be upgraded, which includes major changes to the Belle spectrometer. An initial simulation study indicates that with a tracking device in the very forward region, the background levels in rare events with more than one neutrino could be significantly reduced. The design of the tracking device could profit considerably from the experience gained in sensor development for the LumiCal and BeamCal counters of the linear collider detector.

REFERENCES

- [1] K. Ikado, Phys. Rev. Lett. **97**, 251802 (2006)
- [2] HPQCD Collaboration (Alan Gray et al.), Phys. Rev. Lett. **95**, 212001 (2005)
- [3] W. S. Hou, Phys. Rev. D **48**, 2342 (1993).
- [4] K. Abe et al. (edited by S.Hashimoto, M.Hazumi, J.Haba, J.W.Flanagan and Y.Ohnishi), Letter of Intent for KEK Super B Factory, KEK report 2004-04, <http://belle.kek.jp/superb/>
- [5] K.F. Chen, Missing energy studies for Super-Belle, talk given at the BNM2008 workshop, Jan. 24-26, 2008, Atami, Japan, <http://superb.kek.jp/bnm2008/slide/6A-Chen.pdf>
- [6] W. Wierba, Silicon sensors for LumiCal, these proceedings.

Luminosity Calorimeter

LUMICAL DESIGN OVERVIEW

By

Wojciech WIERBA,

J. BŁOCKI, W. DANILUK, A. GALAS, E. KIELAR, J. KOTUŁA, A. MOSZCZYŃSKI, K. OLIVA, B. PAWLIK, L. SUSZYCKI¹, L. ZAWIEJSKI

Institute of Nuclear Physics PAN, Cracow, Poland

(1) AGH University of Sciences and Technology, Cracow, Poland

Two LumiCal calorimeters will be located in very forward region of the International Large Detector, one of several detector concepts planned for future International Linear Collider, on both sides of the interaction point. LumiCal's will be used for precisely luminosity measurement with accuracy of 10^{-4} . Calorimeters consist of thirty tungsten plates intersected with segmented silicon sensors planes. The actual position of each silicon detector plane relative to each other has to be stable within $\sim 10\ \mu\text{m}$ and the position of the calorimeter relative to the beam line and the interaction point should be known with accuracy of a few hundred micrometers to fulfill the requirements for luminosity measurements. To achieve this goal the structure of the calorimeter has to be very stiff. The aim of this paper is to describe the proposed mechanical structure of the detector, which can fulfill the stiffness requirement. The proposed space for fan out, front-end electronics and cooling system is also presented. Thermal expansion of detector, needs for temperature stabilization are also discussed. The integration with ILD detector is focused on possible fixing LumiCal inside ILD.

Key words: ILC, ILD, precision luminosity measurement, silicon sensors, mechanical structure, integration, thermal expansion, temperature stabilization, water cooling

INTRODUCTION

In the future detector for the International Linear Collider (ILC, with colliding beams of electrons and positrons e^+e^-) [1], the very forward region is a particularly challenging area for instrumentation. The LumiCal detector [2] is expected to give a required precision luminosity measurement and to extend calorimetric coverage of small angles of electron emission from 27.5 to 83.1 mrad. The luminosity measurement will be based on detection of Bhabha event rate and a relative precision of the integrated luminosity of 10^{-4} will be enable [3]. A precise measurement of the scattering polar angles requires an ultimate precision in detector mechanical construction and metrology [4].

DESIGN OVERVIEW

On both sides of the interaction point there will be one LumiCal detector. Each calorimeter is in a form of a barrel which is divided into two parts along the vertical plane. The proposed LumiCal detector will consists of 30 layers of tungsten of 1 radiation length thickness and $320\ \mu\text{m}$ silicon sensors layers. The sensitive region extends from 80 mm to 195.2 mm in radius. The outer radius of calorimeter is foreseen to be 260 mm to cover the space for front end electronics, readout cables, cooling and precision positioning sensors. The

mechanical inner radius is 76 mm [5]. The proposed design overview is presented in Fig. 1.

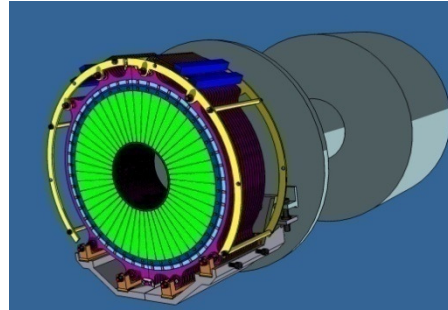


Figure 1. LumiCal mounted on supporting tube.

Tungsten plates

The tungsten plate thickness will be 3.5 mm (1 radiation length) and the shape is shown in Fig. 2.

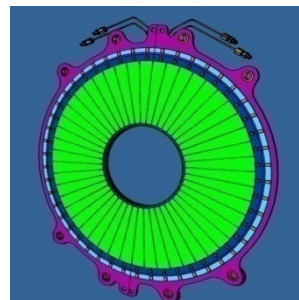


Figure 2. One tungsten plate with silicon sensor glued on and front end electronics.

The tungsten plates have to be divided into two parts to allow detector to be clamped on vacuum beam pipe. More detailed drawing of one half plate is presented in Fig. 3.

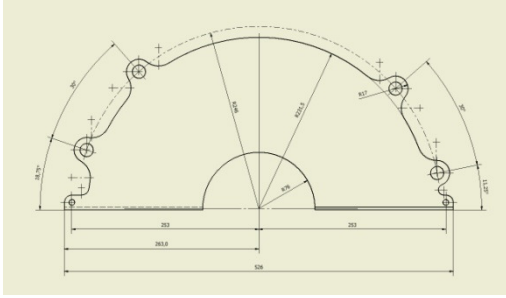


Figure 3. Detailed shape of one tungsten half plate.

To define the center of gravity of one part of the detector the following formulae has been used

$$x_s = \frac{4}{3\pi} \cdot \frac{R_2^3 - R_1^3}{R_2^2 - R_1^2}$$

For $R_2 = 231,50$ mm and $R_1 = 76$ mm, we have $x_s \approx 106$ mm, as it is shown in Fig. 4. It is assumed that there are two support points for the half of the barrel in an equal distance (57 mm) from the gravity center in the horizontal direction (see Fig.4).

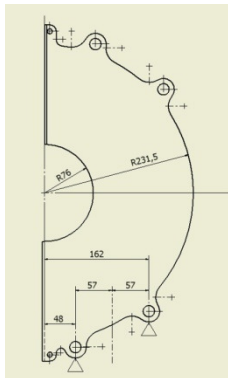


Figure 4. The position of the gravity center.

In fact, for each tungsten plate a plane of the division into two parts is not along the vertical plane but rather along a plane which is rotated around the central axis of the barrel by +3.75 deg or -3.75 deg as it is shown in Fig. 5.

It has to be pointed out that the tungsten plate (+3.75 deg) has the same shape as the tungsten plate (-3.75 deg). It means, that the barrel is composed of only one type of the tungsten plate.

To assemble the calorimeter we need two types of rings shown in Fig. 6. These rings are used as inserts what means that after connecting them with the tungsten plate the inner ring hole is very precisely bored. Now, using special bolts (M12) the barrel can be assembled and placed on the support. It is important that the tension in bolts should be about 15 MPa. The half of the barrel is composed

of thirty tungsten plates to which on the one side silicon detectors have been glued.

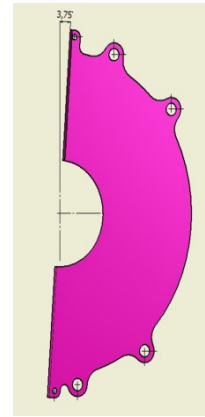


Figure 5. The tungsten plate (+3.75 deg).



Figure 6. Insert ring and spacer

The main advantage of the new design is its simplicity. The structure is composed of very limited number of elements. We have one type of the tungsten plate, two types of the rings, the special M12 bolts and two supporting C frame.

Half barrel closing

Each LumiCal detector is divided into two half barrels clamped on the vacuum beam pipe. Every tungsten plane and silicon sensors are divided into two half parts for that purpose as shown in Fig. 7.

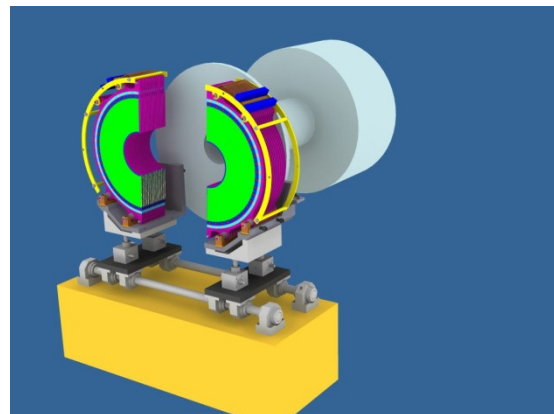


Figure 7. Closing the LumiCal on beam pipe with help of temporary support.

Left and right part of LumiCal barrel should not have a gap in tungsten absorber when closed. There are three possibilities shown in Fig. 8.

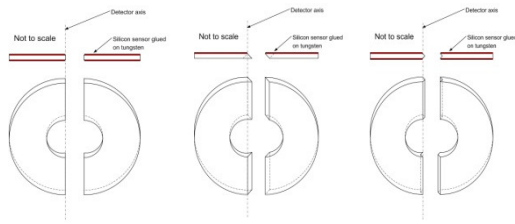


Figure 8. Possible closing of tungsten half planes.

First solution on left does not avoid the gap in tungsten, the second one (in middle) is quite easy to manufacture and acceptable but it is not possible to glue silicon sensors on both sides of tungsten absorber. The third solution has no gap, allows to glue silicon sensors on both sides of tungsten absorber, but is complicated to manufacture. Idea that silicon sensors are glued on the both sides of the fifteen tungsten plates has a remarkable advantage because the number of silicon planes which the position should be monitored is reduced from thirty to fifteen. In addition, the structure fulfills the symmetry condition what is very important from the point of view of thermal deformations. But, due to problem in manufacturing the closing in shape shown on right in Fig. 8. we have decided to use the 45 degree solution (middle drawing in Fig. 8).

Space for front end electronics

One LumiCal will have 92160 electronic readout channels. On one half plane it should be a place for 1536 electronic channels. We foresee a space as shown in Fig. 9.

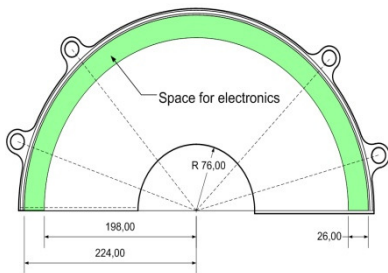


Figure 9. Space for front end electronics on one half plane.

The cross section of a spaced for electronics is presented in Fig. 10.

There is enough space to use a standard wire bonding for electric connections. The major problem is to connect electrically fan out traces on Kapton foil with pads of silicon detector. We can not use wire bonding because there is no space for it. One solution is bump bonding – quite complicated and expensive technology. We try to solve this problem using electrically conductive glue as shown in Fig. 11.

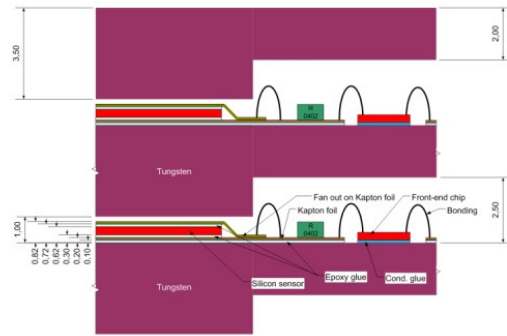


Figure 10. Cross section showing fan out connections to the front end electronics chips.

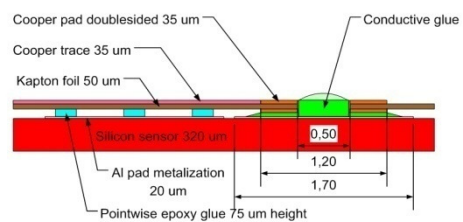


Figure 11. Fan out gluing.

INFLUENCE OF MECHANICAL DESIGN ON LUMICAL PERFORMANCE

Material used for absorber, bolts and spacing rings have some influence on the LumiCal performance and their temperature and electrical behavior have to be taken to account in the next design step.

Thermal expansion

It is foreseen to use the cooling water as a temperature stabilization medium for the LumiCal. Lets assume the temperature change of 1 °C which seems to be a save estimation. Probably, it is possible to stabilize the temperature of one LumiCal within ± 0.2 °C.

The most important parameter for luminosity measurement is an inner radius of LumiCal silicon sensors. This parameter should be known and stable with the accuracy better than 4 μm . The silicon sensors are glued on the tungsten absorber with Kapton E foil insulation. Tungsten has a very small coefficient of thermal expansion α ($\text{CTE} = 4.3 \times 10^{-6} \text{ K}^{-1}$) in comparison with aluminum (~5 times higher) or standard steel (~3 times higher). The inner radius of LumiCal absorber (76 mm) will expand thermally by 0.33 $\mu\text{m}/^\circ\text{C}$. The outer active radius (195.2 mm) will change by + 0.84 $\mu\text{m}/^\circ\text{C}$ and the outer mechanical radius of detector (260 mm) will expand by + 1.12 $\mu\text{m}/^\circ\text{C}$. Silicon has coefficient of thermal expansion α ($2.5 \times 10^{-6} \text{ K}^{-1}$) ~2

times smaller than tungsten. Simplified drawing is shown in Fig. 12.

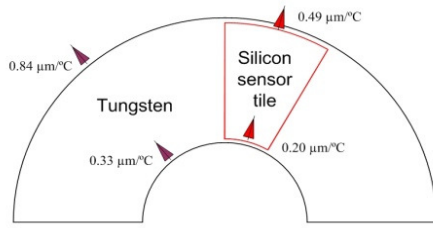


Figure 12. Thermal expansion of the half plate of tungsten absorber and silicon sensor tile glued to the tungsten

Silicon sensor tiles are glued (epoxy adhesive, $CTE = 25 \times 10^{-6} \text{ K}$) to the tungsten absorber with some Kapton E foil ($CTE = 16 \times 10^{-6} \text{ K}$) insulation, it is clearly seen, that silicon sensor tiles and Kapton foil have to be stuck pointwise to tungsten. In that case, we can roughly estimate that the inner active radius of LumiCal will expand less than $0.5 \mu\text{m}/^\circ\text{C}$ and outer radius less than $1.5 \mu\text{m}/^\circ\text{C}$. In real life the thermal expansions of tungsten and silicon will compensate a little (depending on position of the glue dots).

MC simulations have proved that inaccuracy in distances among tungsten plates and silicon sensors along the LumiCal axis less than $50 \mu\text{m}$ has negligible influence to the luminosity measurement. Simplified view of bolt, spacers and rings is shown in Fig. 13.

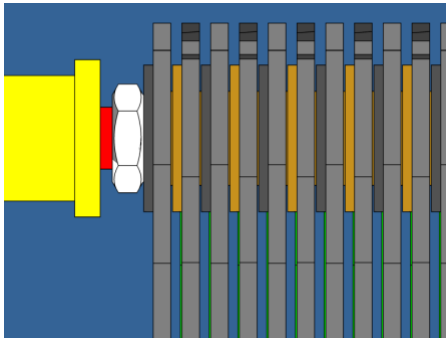


Figure 13. Precision rings (grey) pressed into tungsten plates (light grey) and spacers (dark yellow) on M12 bolts (red) fastened the LumiCal structure.

The total length of LumiCal is 135 mm. Using steel M12 bolts and rings the detector will expand + $2.41 \mu\text{m}/^\circ\text{C}$ and with brass material + $2.63 \mu\text{m}/^\circ\text{C}$. This estimation looks very good, the distances between two silicon sensors will change in z less than $0.1 \mu\text{m}/^\circ\text{C}$ that seems to have negligible influence on luminosity measurement accuracy.

Cooling

Front end electronics will be the major source of heat in the LumiCal. Thanks to the power

cycling during brakes (199 ms) between trains (5 Hz, 1 ms) the dissipated power in one LumiCal will be around 30 W. Lets overestimate 60 W per detector which gives $\sim 2 \text{ W}$ per sensor plane. The water flow of 0.43 l/min. per plane will take heat off with $0.1 \text{ }^\circ\text{C}$ temperature increase. The total cooling water flow in one LumiCal will be less than 15 l/min (more than 3 times overestimated). Some details of cooling system are shown in Fig. 14.

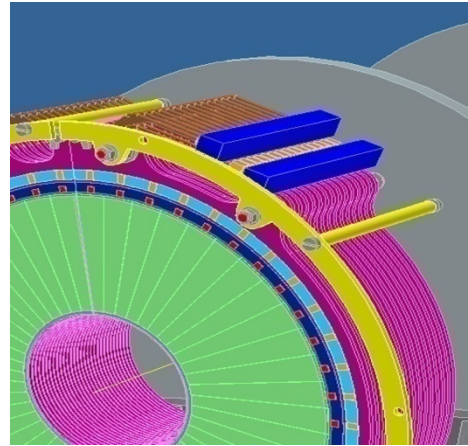


Figure 14. Water cooling system.

The front end electronic chips will be placed directly on tungsten surface (holes in printed circuit board on Kapton foil because of low $TC = \sim 0.19 \text{ W/m}^\circ\text{K}$ for Kapton – see Fig. 10) with thermal (and electrical) conductive glue – thermal epoxy ($TC = \sim 1\div 4 \text{ W/m}^\circ\text{K}$). Tungsten has thermal conductivity ($TC = \sim 200 \text{ W/m}^\circ\text{K}$) a little bit smaller, but comparable with aluminum ($TC = \sim 237 \text{ W/m}^\circ\text{K}$). For the proposed placement of front end chips and cooling water pipes we have roughly estimated the temperature of electronic chips to be $+1.5 \text{ }^\circ\text{C}$ and the tungsten under front electronics to be $\sim +0.3 \text{ }^\circ\text{C}$ over the cooling water temperature (depends on thermal contact between water pipe and tungsten – not yet detailed designed).

Front end electronics grounding

The fast low noise front end chips will be glued directly on tungsten surface with electrical (and thermal) conductive glue (resistivity = $0.01 \div 0.5 \Omega\cdot\text{cm}$). The resistance between electronic chip with 5 mm^2 substrate connected via $100 \mu\text{m}$ thick conductive glue (resistivity max. $0.5 \Omega\cdot\text{cm}$) to the tungsten will be $\sim 0.01 \Omega$ or more less. The resistivity of tungsten ($5.51 \cdot 10^{-8} \Omega\cdot\text{m}$) is 3 times higher than of copper ($1.71 \cdot 10^{-8} \Omega\cdot\text{m}$) but still sufficient for electrical grounding and EMI shielding.

INTEGRATION WITH ILD

The works on integration with ILD detector are concentrated on how to fix the LumiCal inside detector. The LumiCal will be fixed to the supporting tube as presented in Fig. 15.

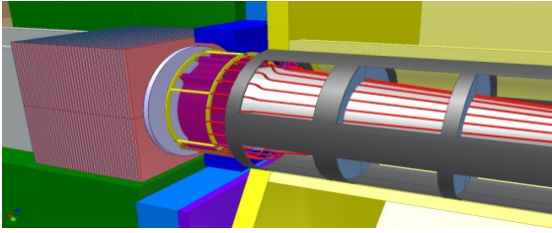


Fig. 15. LumiCal in front of LHC, conical shape of beam pipe

The discussion with ILD are concentrated on the special ‘shelf’ for LumiCal positioning and fixing, see Fig. 16.

The space for cables and cooling pipes is also under discussion. The crucial point is the Laser Alignment System for LumiCal’s . In Fig. 17. you can see proposed laser beams for precision alignment.

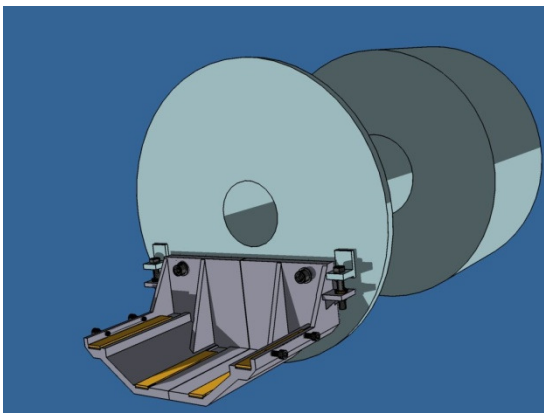


Fig. 16. “Shelf” screwed to the supporting tube to fix LumiCal inside ILD.

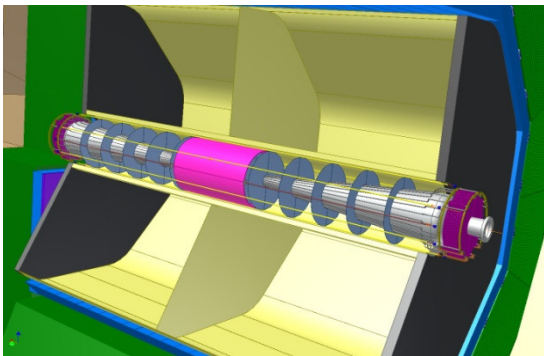


Fig. 17. Proposed laser beams for LAS.

CONCLUSIONS

The mechanical design of the LumiCal is in a very good shape, we have proved the stiffness of proposed construction. The design is quite simply, the structure is composed of very limited number of precisely manufactured elements.

First attempt has been made to discuss place for front end electronics and evaluate the cooling needs. We have estimated the thermal expansion of mechanical structure influence on luminosity measurement accuracy. First results shows, that

only the inner acceptance radius of LumiCal has to be controlled very precisely. Temperature stabilization of LumiCal within 2°C seems to be necessary. Additional online alignment sensors near the beam pipe are foreseen.

REFERENCES

- [1] International Linear Collider:
<http://www.linearcollider.org/cms>;
Reference Design Report, ILC-REPORT-2007-001.
- [2] TESLA Technical Design Report, DESY 2001-011, ECFA 2001-209, March 2001; H. Abramowicz et al., IEEE Transactions of Nuclear Science, 51 (2004) 2983; R&D for ILC – Detector, Instrumentation of the Very Forward Region, The Forward Calorimetry (FCAL) Group, DESY PRC R&D Report 02/01, April, 2006; Large Detector Concept, LDC outline document: <http://www.ilcldc.org/documents> .
- [3] A.Stahl, *Luminosity Measurement via Bhabha Scattering: Precision Requirements for the Luminosity Calorimeter.*, LC-DET-2005-004, Apr 2005.
- [4] J. Błocki et al., *Laser measurement of the LumiCal detector displacement*, Report No. [1985/PH](#) , 2006, IFJ PAN, Cracow, Poland.
- [5] J. Błocki et al., *A proposal for the mechanical design of the LumiCal detector*, Report No. [1990/PH](#) , 2006, IFJ PAN, Cracow, Poland.

ASPECTS OF LUMICAL INTEGRATION WITH ILC

By

Bogdan PAWLIK

INP PAN, Krakow, Poland

In this report influence of latest ILC detector geometry on performance of the luminosity detector LCAL is presented. Reconstruction accuracy, magnitude of accepted Bhabha process cross-section and beamstrahlung background are examined. Geometry of the beam-pipe seems to be dominant issue concerning beamstrahlung background.

Key words: LCAL, LumiCal, ILC, Bhabha events rate, beam-strahlung background, beam pipe shape, luminosity measurement accuracy.

INTRODUCTION

The main goal of the luminosity detector LCAL (formerly LumiCal) is to measure the luminosity with required relative accuracy $\Delta\mathcal{L}/\mathcal{L} \approx 10^{-4}$. This is an ultimate goal that must be achieved to justify presence of LCAL. Recently ongoing process of "ILD optimization" and included engineering constraints forces examining performance of LCAL in new optional geometry setups.

The ILC detector concept includes changes in comparison with LDC detector model as following:

- increase distance of LCAL from IP from 2227 mm to 2512 mm
- construction constraints suggest decreasing outer

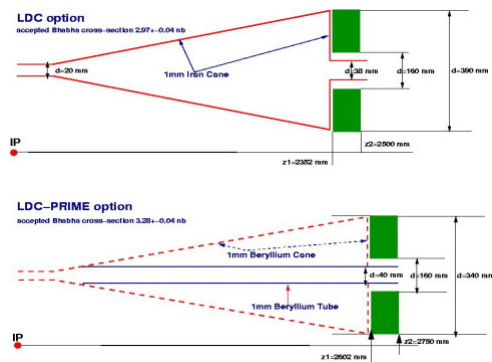


Fig.1

Figure 1. Comparison of LCAL and beam pipe setups for ILC and ILC models

LCAL radius from 195 to 170 mm

- change of the shape of beam pipe in front of LCAL from conical to tube-like shape.

Simplified setup of beam pipe and LCAL is shown in [Fig. 1].

BHABHA EVENT RATE

The Bhabha event rate depends on the detector acceptance. As the cross-section scales as $1/\theta^3$ the

lower minimum polar angle of detector acceptance the higher cross-section can be measured. Table 1 summarizes results of calculations made using BHLUMI program.

Table. 1 Comparison of accepted Bhabha cross-section and event rates.

	Fiducial Volume [rad]	Cross-section [nbarn]	Event rate ^{a)} [Hz]
LDC	0.034-0.078	2.97±0.04	~60
ILD	0.031-0.063	3.28±0.04	~65

As can be seen increase of the distance from IP increases, as expected, accepted cross-section (event rate). The cross-section in Fiducial Volume shown in Tab.1 is for the events when both leptons were found in the indicated polar angle range. No further requirements were imposed. Effectively tagging an event as the Bhabha event needs more conditions to be fulfilled – this filtering will reduce effective size of data sample that can be used for luminosity calculations. Event rates quoted in Tab.1 can be straightforward translated into the time needed to accumulate sufficient data sample to estimate actual machine luminosity, frequency quoted means that to achieve statistical error $\sim 10^{-4}$ (luminosity $\sim 500 \text{ fb}^{-1}$) one needs ~ 1 year of running at nominal machine luminosity. Obviously the shorter this time the better.

POLAR ANGLE RESOLUTION

The relative error on luminosity measurement can be expressed with a good approximation as :

$$\Delta\mathcal{L}/\mathcal{L} \approx \Delta\theta/\theta_{min}$$

^{a)} Event rate calculated using nominal machine luminosity $2 \times 10^{34} \text{ cm}^{-2}\text{s}^{-1}$.

where $\Delta\theta$ is an offset on reconstructed polar angle and θ_{min} is lowest polar angle accepted. As can be seen from [Fig.2] change of the shape of beam pipe from cone to tube induces increase of amount of material on the path of particles from IP to LCAL by factor of ~ 10 . This may lead to decreased performance of the detector, concerning angular resolution, due to scattering of the primary particle off the beam pipe wall. The simulations done for two options (conical/tube like) of the shape of beam pipe (Tab.2) indicates increase of polar angle offset by 4 STD, while resolution seems to be better. This results, based on quite limited data samples (10 000 events) and need further exploration, indicate that conical shape of beam-pipe in front of LCAL, is preferred.

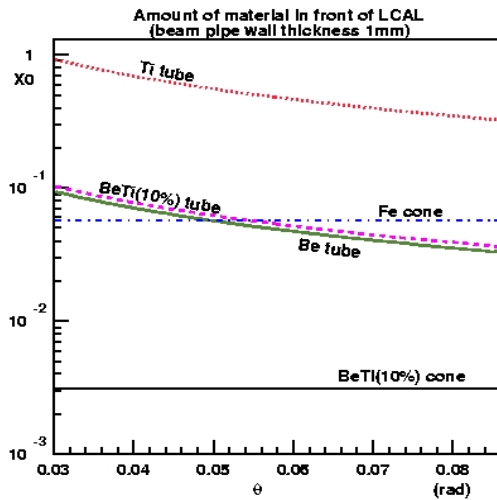


Figure 2. Amount of material in front of LCAL for different options of beam pipe shapes.

Table 2. Comparison of reconstructed polar angle offset and resolution for two option of beam-pipe shape.

	$\Delta\theta$ [μrad]	$\sigma(\theta)$ [μrad]
cone	1.8 ± 0.1	27.6 ± 0.1
tube	2.2 ± 0.2	26.8 ± 0.2

BEAMSTRAHLUNG BACKGROUND

Beamstrahlung profile (X-Y projection) is shown at [Fig.3].

The radius of beam-pipe is constrained by inner radius of LCAL and radius of “beamstrahlung tube”. An optimal radius would be that minimizing number of hits in LCAL and maximizing event rate. As can be seen, beam-pipe centered on outgoing beam-line minimizes beamstrahlung background. It indicates also possibility to reduce inner LCAL radius to 60-70 mm. This would increase significantly event rate to 5.34 nbarn (event rate ~ 100 Hz).

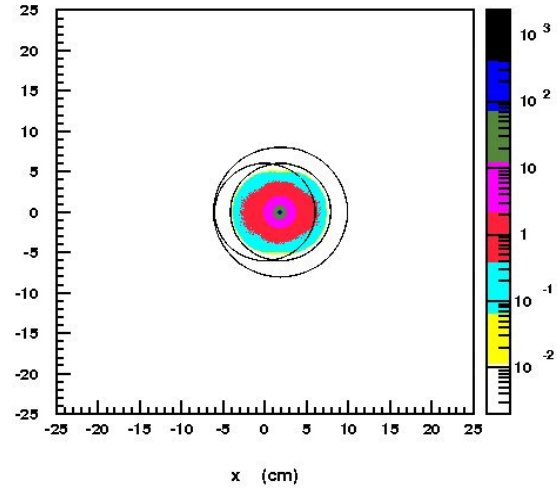


Figure 3. Beamstrahlung profile and three options of beam-pipe position and radii.

SUMMARY

The most important parameter in the “LDC \rightarrow ILD” conversion process seems to be design of beam pipe in front of LCAL and radius of LCAL inner beam-pipe which must be greater then ~ 60 mm.

REFERENCES:

ELSEWHERE

TOWARDS A FINAL SELECTION FOR LUMINOSITY MEASUREMENT

By

Ivan SMILJANIĆ, Ivanka BOŽOVIĆ JELISAVČIĆ, Miša PANDUROVIĆ, Mihajlo MUDRINIĆ and Judita MAMUŽIĆ

Vinča Institute of Nuclear Sciences, Belgrade, Serbia

This paper is to summarize proposed selection for luminosity measurement with respect to the studied systematic effects (beam-beam interaction, presence of physics background, detector energy resolution and bias of energy scale). Study has been done for the LDC concept of detector for ILC.

Key words: ILC, FCAL, LDC, luminosity calorimeter, luminosity measurement, systematics

INTRODUCTION

Due to the relatively large cross-section, and possibility to accurately calculate the cross-section from theory, small-angle Bhabha scattering is used to measure and monitor the luminosity of electron-positron colliders, such as the International Linear Collider (ILC). Measurement of event rate of the Bhabha scattering process in the Luminosity Calorimeter (LumiCal) in the very forward region of the ILC is a way to determine luminosity at ILC [1]. Physics case at ILC (precision EW measurements, TGCs) requires control of the systematic error of luminosity at the level of 10^{-3} or 10^{-4} for the GigaZ case.

Luminosity calorimeter has been designed for the precise determination of the total luminosity. This is compact electromagnetic sandwich calorimeter consisting of 30 longitudinal layers of silicon sensor followed by tungsten absorber and the interconnection structure. In the Large Detector Concept (LDC) assumed here [2], it is located at $z=2270$ mm from the IP, covering the polar angle range between 35 and 87 mrad. It corresponds to the inner radius of the LumiCal of $r_{min}=80$ mm, and outer radius of $r_{max}=195$ mm. Tungsten and silicon thickness is about one radiation length. In order to provide precise reconstruction ($\Delta\theta=2.9\cdot 10^{-6}$ rad, $\delta(\theta)=3.3\cdot 10^{-5}$ rad) of the polar angle, segmentation of sensor planes is set as follows:

- 30 layers, 64 radial divisions, 48 azimuthal divisions;
- azimuthal cell size - 131 mrad;
- radial cell size - 0,8 mrad.

Layout of the forward region in the Large Detector Concept is shown in Figure 1 [3].

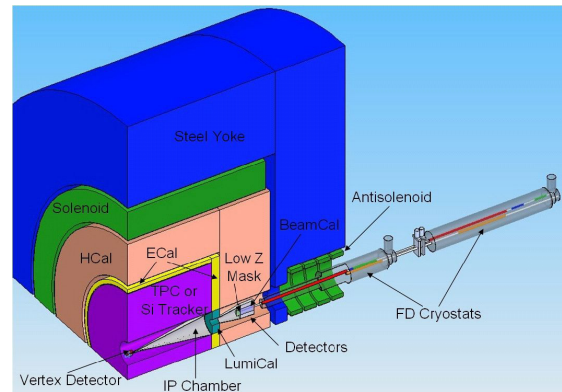
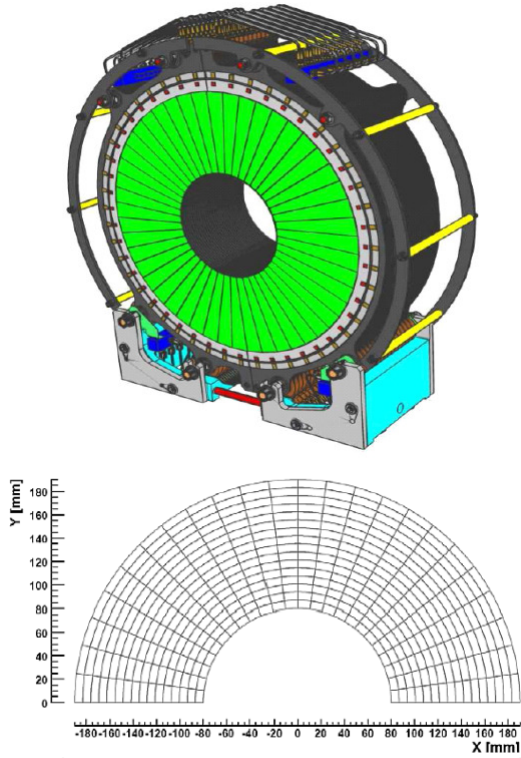


Figure 1. Layout of the forward region in the LDC concept

Luminosity calorimeter is centered along the outgoing beam in order to avoid azimuthal angle dependence of luminosity uncertainty. LumiCal, together with sensor segmentation, is illustrated at Figure 2 [4].

The aim of this study is to optimize event selection for luminosity measurement taking into account following effects:

- beam-beam deflection;
- physics background;
- bias of energy scale and
- finite energy resolution of the detector.



(every fourth radial segment is drawn)

Figure 2. LumiCal and the segmentation of sensor half-plane

METHOD

Integrated luminosity at ILC will be determined from the total number of Bhabha events N_{th} produced in the acceptance region of the luminosity calorimeter and the corresponding theoretical cross-section σ_B .

$$L_{int} = \frac{N_{th}}{\sigma_B} \quad (1)$$

The number of counted Bhabha events N_{exp} has to be corrected for the number of background events misidentified as Bhabhas, N_{bck} , and for the selection efficiency ε .

$$L_{int} = \frac{N_{exp} - N_{bck}}{\varepsilon \cdot \sigma_B} \quad (2)$$

Bhabha events with cross-section of $\sigma_{bha} = (4.12 \pm 0.03) nb$ are simulated with BHLUMI [5] event generator, implemented in BARBIE [6], a GEANT3 [7] based detector simulation of LumiCal. These events are simulated with no crossing angle, due to its small effect on the cross-section. Selection criteria have been optimised with respect to the studied systematics.

BEAM-BEAM DEFLECTION

Signal and background will be additionally affected by the beam-beam interaction effects. They will modify both initial state, through

beamstrahlung, and the final state through electromagnetic deflection, resulting in the total suppression of the Bhabha cross-section (BHSE) of order of 4.4%. In order to reduce this hard-controlled effect to 1.5%, asymmetric theta cuts are used [8]. With the given LumiCal geometry, cuts are set as follows:

- cut 1: 39-80 mrad;
- cut 2: 35-87 mrad.

These cuts are applied subsequently to forward and backward sides of the detector, in order to reduce systematics for the IP position and relative position of forward and backward detector.

PHYSICS BACKGROUND FROM 2-PHOTON PROCESSES

Four-fermion NC processes $e^-e^+ \rightarrow e^-e^+\bar{f}f$ are considered to be the main source of physics background for luminosity measurement [9]. They are dominated by the multiperipheral processes (2-photon exchange). Corresponding Feynman diagram is given in Figure 3.

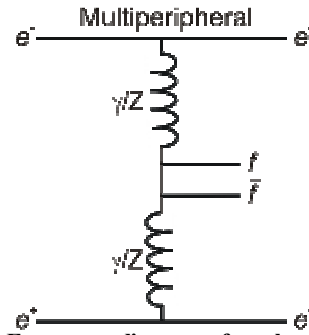


Figure 3. Feynman diagram for the dominant 2-photon exchange

Two-photon processes are having high cross-section around $10 nb$, as shown at Figure 4. [10], comparable to the signal.

Outgoing e^-e^+ pairs are emitted along the beam pipe carrying the most of energy, while low-energetic $\bar{f}f$ pairs are distributed over a wider polar angle range. Due to the steep polar angle distribution of the produced particles, the most of energy is to be deposited in the beam calorimeter while low-energetic particles are mainly deposited in the luminosity calorimeter.

In this study, background processes are simulated using WHIZARD event generator [11], [12], [13]. One million leptonic and one million hadronic events are simulated including contribution of all neutral tree-level processes in the full angular range. Total cross-section $\sigma_{tot} = (2.05 \pm 0.05) nb$ is obtained, with following assumption on generation:

- invariant masses of outgoing lepton pairs are greater than $1 GeV/c^2$

- momentum transferred in photon exchange is also greater than $1 \text{ GeV}/c$.

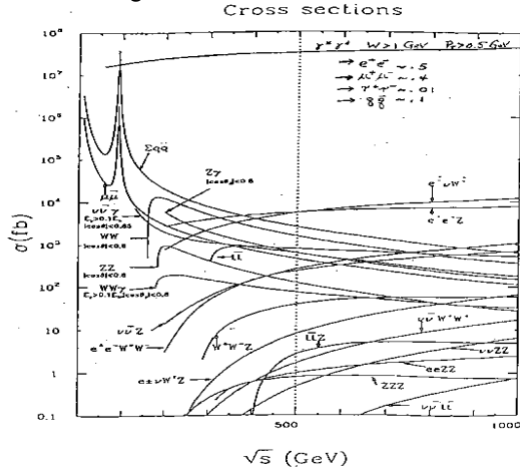


Figure 4. Cross-sections for 2-photon processes with respect to CMS energy

Using WHIZARD event generator, it seems that the cross-section is insensitive to the momentum transferred in photon exchange.

ENERGY RESOLUTION AND BIAS OF ENERGY SCALE

Energy of particles in LumiCal is measured through the calibration procedure, assuming both showers fully contained in the LumiCal.

$$\frac{\Delta E}{E} = \frac{\delta E}{\sqrt{E}} \sqrt{\text{GeV}} \quad (3)$$

Simulation has shown that energy resolution of $\delta E \cong 21\%$ is achievable with the studied LumiCal design [14]. Measured particle energy is, thus, affected by the finite energy resolution and the possible bias. Since the detector is being calibrated under realistic beam conditions, the bias of energy scale can also be present.

EVENT SELECTION

Bhabha events are identified by two electromagnetic cascades carrying the full beam energy, originating from collinear and coplanar Bhabha particles. As mentioned above, collinearity of Bhabha events is to small extent distorted due to the beam-beam interaction effect. Beam-beam interaction is accommodated by using asymmetric cuts on particle polar angle. In addition, characteristic topology of Bhabha events allows us to define a sensitive variable to distinguish signal from physics background:

- relative energy, defined as a fraction of beam energy, E_{beam} , carried by the Bhabha particle (E_L and E_R are the energies of particles deposited at the left and right side of the LumiCal):

$$E_{rel} = \frac{E_L + E_R}{2 \cdot E_{beam}} \quad (4)$$

- energy balance and

$$E_{balance} = \frac{|E_L - E_R|}{E_{min}} \quad (5)$$

- modified energy balance

$$\alpha = \frac{|E_L - E_R|}{E_L + E_R} \quad (6)$$

both measuring difference between energy depositions at forward and backward (left and right) sides of the LumiCal.

RESULTS

Here we studied combinations of asymmetric cuts with sensitive variables (4), (5) and (6) with respect to the physics background, detector energy resolution and bias of energy scale.

Relative energy cut

As shown on Figure 5, to keep the luminosity uncertainty ($\Delta L/L$) at the level of 10^{-4} , relative Bhabha energy should be controlled better than 187 MeV (20 MeV) at $E_{rel}=150 \text{ GeV}$ ($E_{rel}=200 \text{ GeV}$). This is obtained from the linear fit of efficiency slope at $E_{rel}=150 \text{ GeV}$ and $E_{rel}=200 \text{ GeV}$ respectively.

With the looser cut on relative energy, more background particles will be misidentified as Bhabhas. Therefore, it is necessary to investigate background to signal ratio (B/S) with respect to the relative energy cut. The result is shown in Figure 6.

The tighter cut at 200 GeV suppresses background more efficiently ($B/S=6.56 \cdot 10^{-4}$) than the cut at 150 GeV ($B/S=1.19 \cdot 10^{-3}$), but the value of B/S at 150 GeV is still acceptable under the assumption that background can be controlled at the level of 10^{-1} .

At Figure 7, luminosity uncertainty dependence on energy bias is shown, for relative energy cut at 150 GeV . Linear fit implies that if there is a bias of energy scale, it has to be known with the margin of 148 MeV to keep the luminosity uncertainty at 10^{-4} level.

In order to check how well the detector energy resolution needs to be controlled, a random number generator is used to smear the energy of particles that caused showers in the LumiCal. Figures 8 and 9 show luminosity uncertainty dependence on energy resolution at $E_{rel}=200 \text{ GeV}$ and $E_{rel}=150 \text{ GeV}$ respectively. As shown on Figure 8, to preserve luminosity uncertainty below 10^{-4} , detector energy resolution at $\delta E=20\%$ should be controlled at 1.5% level. This is consistent with the value estimated by A. Stahl [15].

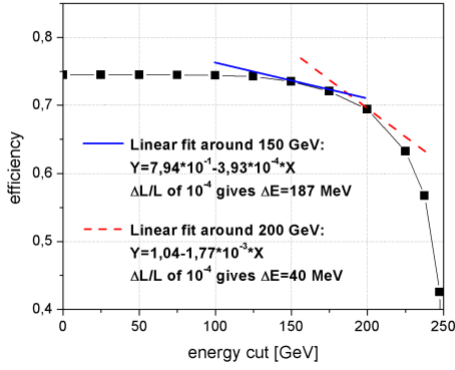


Figure 5. Efficiency vs. relative energy cut

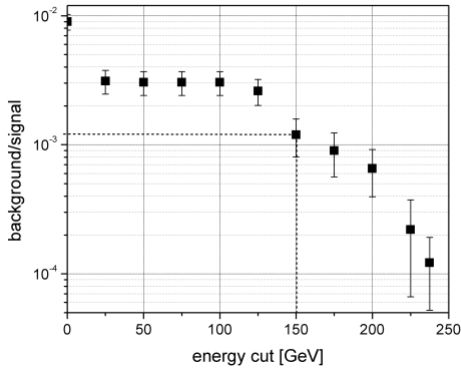


Figure 6. Background to signal ratio vs. relative energy cut

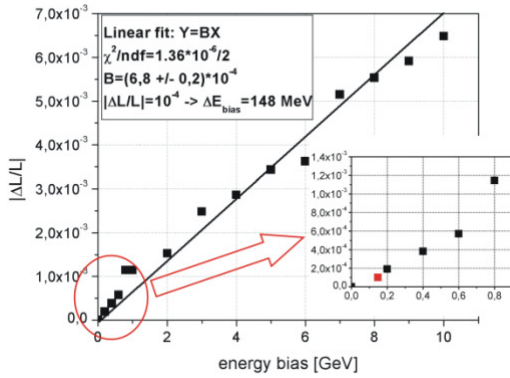


Figure 7. Luminosity uncertainty vs. bias of energy scale for $E_{rel} > 150 \text{ GeV}$.

Assuming that Bhabha particles carry more than 60% of the beam energy, a linear fit shown on Figure 9 implies that the detector energy resolution needs to be loosely controlled at the level of 25%, independently of the resolution itself. Both fits are done within 2σ statistical dissipation of data.

Energy balance cut

As shown on Figures 10 and 11, background to signal ratio of $1.04 \cdot 10^{-4}$ can be achieved with $E_{balance} < 0.2$, corresponding to the efficiency of 63.3%. Despite the fact that the luminosity uncertainty is not dominated by the statistical error,

this selection is more than 10% less efficient than the one based on the relative energy.

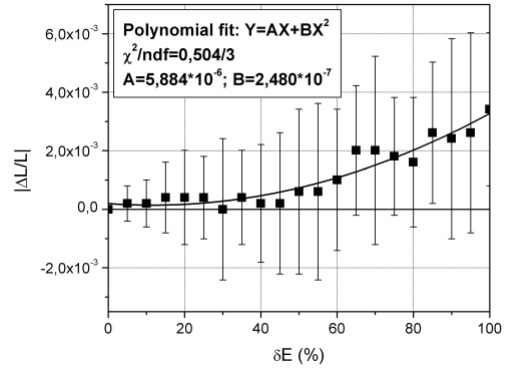


Figure 8. Luminosity uncertainty dependence on energy resolution for $E_{rel} > 200 \text{ GeV}$

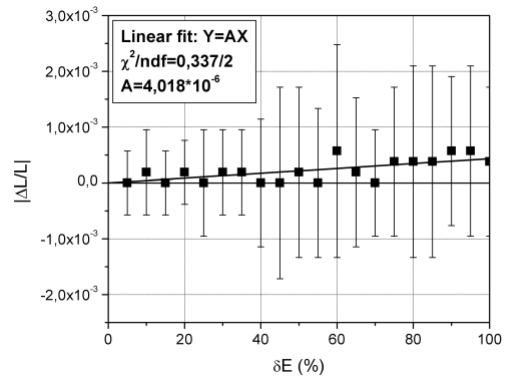


Figure 9. Luminosity uncertainty dependence on energy resolution for $E_{rel} > 150 \text{ GeV}$

The major disadvantage of this selection comes from the very small margin to control the detector energy resolution δE . Polynomial fit shown at Figure 12 indicates that $\delta E = 20\%$ has to be controlled at the level of 0,56% to keep the luminosity uncertainty below 10^{-4} . Therefore, energy balance cut should not be used instead of relative energy cut.

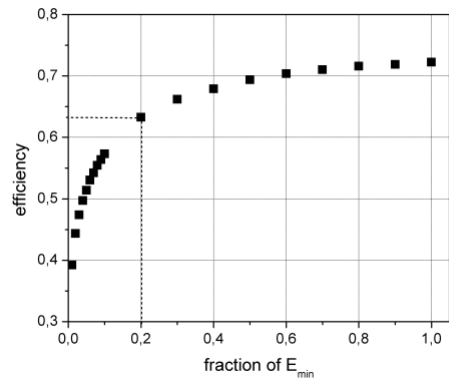


Figure 10. Bhabha selection efficiency vs. energy balance cut

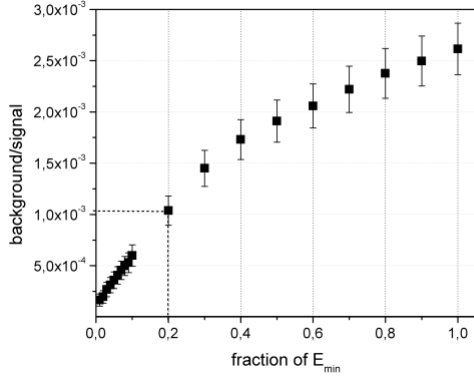


Figure 11. Background to signal ratio vs. energy balance cut

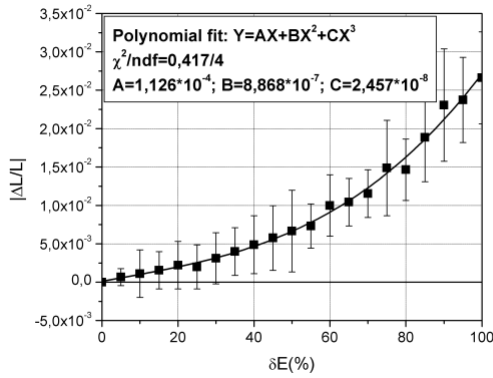


Figure 12. Luminosity uncertainty vs. detector energy resolution for $E_{balance} < 0,2E_{min}$

Modified energy balance – “alpha” cut

Modified energy balance “alpha” is variable similar to energy balance by its physical content. As shown on Figures 13 and 14, $\alpha < 0,6$ looks like a reasonable for cut-off value: background requires no tight control ($B/S=4.27 \cdot 10^{-4}$) and the efficiency curve comes into saturation with respect to alpha.

If there is a bias (offset) of energy scale, it should be known with margin of $\pm 670 \text{ MeV}$, if one wants to know luminosity at the level of 10^{-4} , as shown on Figure 15.

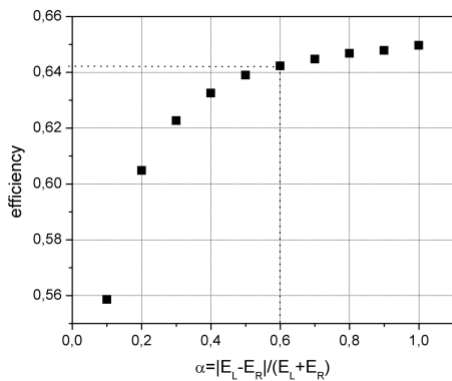


Figure 13. Bhabha selection efficiency vs. alpha

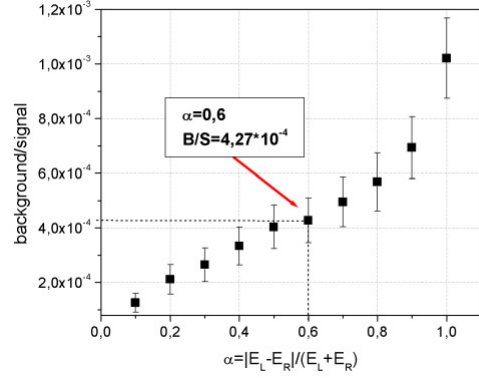


Figure 14. Background to signal ratio vs. alpha

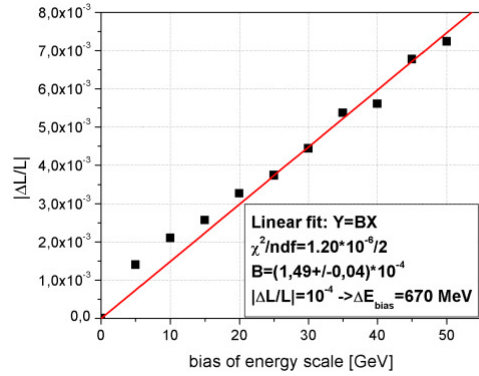


Figure 15. Luminosity uncertainty vs. bias of energy scale for $\alpha < 0,6$

As can be seen on Figure 16 this cut is, within statistical uncertainty margins of 2σ , insensitive to the energy resolution of detector.

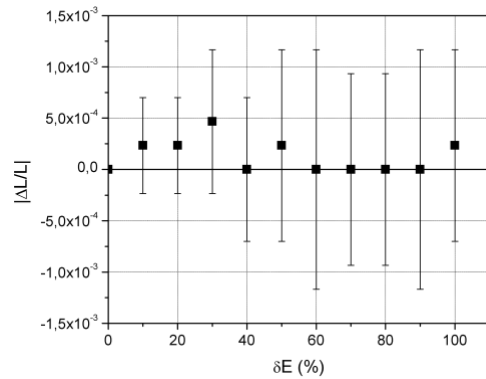


Figure 16. Luminosity uncertainty vs. energy resolution for $\alpha < 0,6$

CONCLUSION

For selection based on asymmetric cuts on particle polar angle and modified energy balance, luminosity measurement is the least sensitive to the studied systematic effects:

- beam-beam interaction ($BHSE=1,5\%$);
- presence of physics background ($B/S \sim 10^{-4}$);

- finite detector energy resolution ($\delta E=20\%$) and
- (unknown) bias of energy scale.

With the given selection, to contribute to the luminosity uncertainty of $\Delta(L)/L=10^{-4}$, bias of energy scale has to be controlled better than 670 MeV (or approximately third of a percent of Bhabha energies), while the luminosity measurement is practically insensitive to the control of detector energy resolution and description of physics background processes. However, BHSE is a percent effect and to be controlled better than 10^{-2} , requires variations in the reconstructed luminosity spectrum to be known with the precision of $4 \cdot 10^{-3}$ and beam parameters (σ_z and σ_x) to be known better than 20% under realistic beam conditions [8].

Proposed selection is preliminary in terms of forward region design modifications towards the integration into ILD detector concept.

REFERENCES

- [1] International Linear Collider; Reference Design Report, April 2007, <http://www.linearcollider.org/cms/>
- [2] Detector outline document for the Large Detector Concept, LDC Working Group for the Reference Design Report of the International Linear Collider, August 2006, <http://www.ilclde.org/documents/dod/>
- [3] Jelisavčić Božović I., Pandurović M., The Forward Calorimetry at ILC
- [4] Sadeh I., The Luminosity Calorimeter, talk given at the ILC ECFA Workshop, Warsaw, Poland, June 2008
- [5] Jadach S., Placzek W., Richter-Was E., Ward B.F.L. and Was Z., BHLUMI, A Monte Carlo Event Generator for Bhabha Scattering at Small Angles, Version 4.04.
- [6] Pavlik B., BARBIE Version 4.1, Simulation package of the TESLA luminosity calorimeter
- [7] Application Software Group, 1994. Computing and Networks Division GEANT—Detector Description and Simulation Tool, CERN Program Library Long Wriiteup W5013, CERN, Geneva, Switzerland, http://wwwasdoc.web.cern.ch/wwwasdoc/geant_html3/geantall.html
- [8] Rimbault C., Bambade P., Mönig K. and Schulte D., Impact of beam-beam effects on precision luminosity measurements at the ILC, 2007 JINST 2 P09001 doi: 10.1088/1748-0221/2/09/P09001
- [9] Jelisavčić Božović I., Pandurović M., Mudrinić M., Smiljančić I., Physics background as a systematic effect in luminosity measurement at International Linear Collider, Facta Universitatis, Series Physics, Chemistry and Technology, Vol. 5, No 1, 2007
- [10] Nauenberg U., The BeamCal Simulation Project Progress Report, talk given at the FCAL Collaboration meeting, Institute of Nuclear Physics, IFJ PAN, Krakow, Poland, 6-7 May 2008
- [11] Kilian W., Ohl T., Reuter J., WHIZARD: Simulating Multi-Particle Processes at LHC and ILC, arXiv: 0708.4233 [hep-ph] 0708.4233 [hep-ph] <http://arxiv.org/abs/0708.4233>
- [12] Moretti M., Ohl T., Reuter J., O'Mega: An Optimizing matrix element generator, LC-TOOL-2001-040-rev, arXiv: hep-ph/0102195-rev <http://arxiv.org/abs/hep-ph/0102195>
- [13] Kilian W., WHIZARD Manual 1.0, LC-TOOL-2001-039, <http://www-flc.desy.de/lcnotes/>
- [14] Sadeh I., LumiCal Optimization Simulations, talk given at the FCAL Collaboration meeting, Institute of Nuclear Physics, IFJ PAN, Krakow, Poland, 6-7 May 2008
- [15] Stahl A., Luminosity Measurement via Bhabha Scattering: Precision Requirements for the Luminosity Calorimeter, LC-DET-2005-004, May 2005.

INFLUENCE OF THE SHAPE OF THE BEAMPIPE ON THE LUMINOSITY MEASUREMENT AT THE ILC

By Iftach SADEH

School of Physics and Astronomy, The Raymond and Beverly Sackler Faculty of Exact Sciences, Tel Aviv University, Tel Aviv, Israel.

Measurement of the luminosity at the International Linear Collider will be accomplished by counting the number of Bhabha scattering events at small angles. This measurement depends on the amount of material which is placed in front of the luminosity calorimeter, due to possible pre-showering of particles. In the current detector layout no such material is foreseen, owing to the structure of the beampipe. Here, an alternative design is considered, for which particles pass through the beampipe before reaching the luminosity calorimeter. The subsequent effect on the luminosity measurement is studied.

Key words: ILC, FCAL, LDC, luminosity calorimeter, luminosity measurement, systematics

INTRODUCTION

The focus of this study is the luminosity calorimeter (LumiCal) of the e^+e^- International Linear Collider (ILC). The requirement for LumiCal is to enable a measurement of the integrated luminosity with a relative precision of about 10^{-4} [1]. Bhabha scattering is used as the gauge process for the luminosity measurement [2].

For small angles ($\leq 10^\circ$), Bhabha scattering is dominated by the t-channel exchange of a photon [3]. One can write the differential with respect to the scattering angle of the cross-section, σ_{Bh} , as

$$\frac{d\sigma_{Bh}}{d\theta} = \frac{2\pi\alpha^2}{s} \frac{\sin\theta}{\sin^4(\theta/2)} \approx \frac{32\pi\alpha^2}{s} \frac{1}{\theta^3}. \quad (1)$$

The scattering angle θ is the angle of the scattered lepton with respect to the beam, α is the fine structure constant, and s is the e^+e^- center-of-mass energy squared.

Strictly speaking, Born-level elastic Bhabha scattering never occurs. In practice, the process is almost always accompanied by the emission of electromagnetic radiation, for example, $e^+e^- \rightarrow e^+e^-\gamma$. A set of topological cuts is applied in order to distinguish Bhabha scattering from the background processes. This is done by comparing the position and the energy of electromagnetic (EM) showers, which are initiated in the two arms of LumiCal by the scattered particles. The amount of energy in each arm relative to the beam energy is also constrained, and the reconstructed position of each shower must lie within the fiducial volume (acceptance region) of the detector [4, 5, 6].

Several factors, such as the energy resolution and the bias in the reconstruction of the position of showers, induce an error in the luminosity measurement. The error manifests as miss-counting of the number of expected Bhabha scattering events

within the fiducial volume. It is convenient to define the relative bias in counting as

$$\delta\mathcal{N} = \frac{N_{rec} - N_{gen}}{N_{gen}} \left| \frac{\theta_{max}^f}{\theta_{min}^f} \right|, \quad (2)$$

where N_{rec} and N_{gen} are respectively the number of reconstructed and generated Bhabha events, and θ_{min}^f and θ_{max}^f are the respective low and high bounds on the fiducial volume of LumiCal. Accordingly, the relative error of the integrated luminosity, \mathcal{L} , comes down to

$$\Delta\mathcal{L}/\mathcal{L} = \delta\mathcal{N} \quad (3)$$

SIMULATION OF THE DETECTOR RESPONSE

In the current detector layout [2, 7], LumiCal is placed 2,27 m from the interaction point (IP). LumiCal is a tungsten-silicon sandwich calorimeter. The inner radius of LumiCal is 80 mm, and its outer radius is 190 mm, resulting in a polar angular coverage of 35 to 84 mrad. The longitudinal part of the detector consists of layers, each composed of 3:5 mm of tungsten, which is equivalent to 1 radiation length thickness. Behind each tungsten layer there is a 0,6 mm ceramic support, a 0,3 mm silicon sensors plane, and a 0,1 mm gap for electronics. As a result, the Molière radius² of LumiCal, R_M , is 14 mm. LumiCal is comprised of 30 longitudinal layers. The transverse plane is subdivided in the radial and azimuthal directions. The number of radial divisions is 64, and the number of azimuthal divisions is 48. The fiducial volume of LumiCal is defined by $\theta_{min}^f = 0,41 \text{ mrad}$

² The Molière radius is the distance around the center of an EM shower, in which, on average, 90% of the energy of the shower may be found.

and $\theta_{\max}^f = 0,69 \text{ mrad}$. Figure 1 presents the segmentation scheme of a LumiCal sensor plane.

The response of LumiCal to the passage of particles was simulated using MOKKA, version 06-05- p02 [8]. MOKKA is an application of a general purpose detector simulation package, GEANT4, of which version 9.0.p01 was used [9].

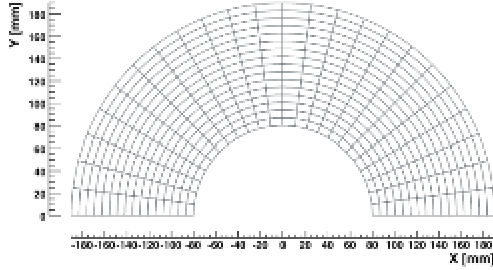


Figure 1. Half plane of LumiCal silicon sensors (every fourth radial segment is drawn).

PHYSICS SAMPLE

The physics sample which was investigated consisted of 10^6 Bhabha scattering events with center-of-mass energy $\sqrt{s} = 500 \text{ GeV}$. The events were generated using BHWIDE, version 1.04 [10]. BHWIDE is a wide angle Bhabha MC, which contains the electroweak contributions, which are important for the high energy e^+e^- interactions considered here. The sample contains only events in which the leptons are scattered within $35 < \theta < 84 \text{ mrad}$, which is the physical polar angular range of LumiCal.

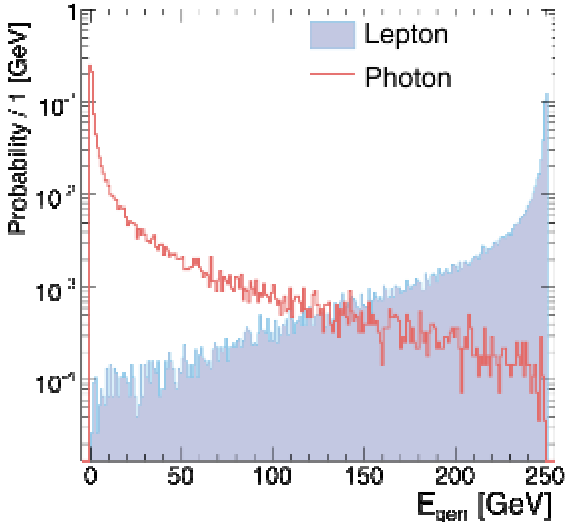


Figure 2. Distributions of the production energy, E_{gen} , of leptons and of photons, as denoted in the figure.

Figure 2 shows the energy spectrum of the scattered leptons and radiative photons. The lepton distribution peaks at 250 GeV, as expected, and has a long tail of lower energies, accounting for the energy which was carried away by the photons.

Figure 3 shows the polar production angle of scattered leptons and radiative photons³. The distribution of the polar angle is cut according to the fiducial volume of LumiCal.

Since most initial state radiative photons travel through the beampipe and are undetected, only final state photons are considered. Conservation of momentum dictates that the more energy these photons take from the lepton, the smaller the angular separation between the two. This is confirmed in Fig. 4, which shows the correlation between the photon energy and its separation from the accompanying lepton.

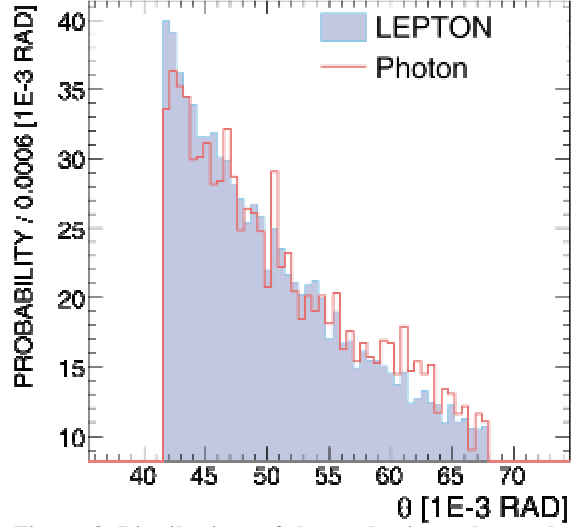


Figure 3. Distributions of the production polar angle, θ , of leptons and of photons, as denoted in the figure.

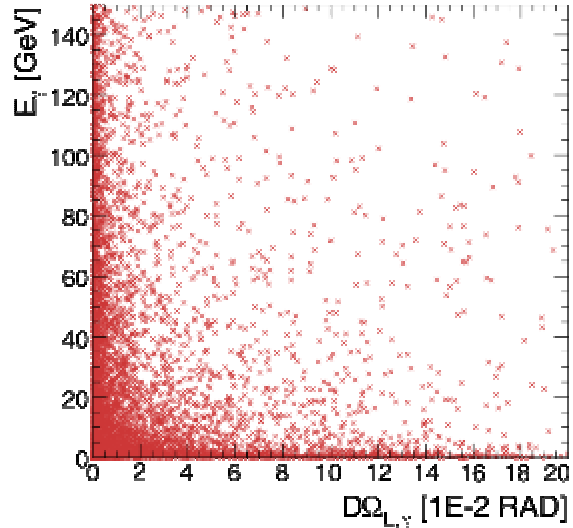


Figure 4. Correlation between the angular separation between leptons and radiative photons, $\Delta\Omega_{l,\gamma}$ and the photon energy, E_γ .

³ Naturally the electron and the positron have polar angles of opposite signs, but as the distributions of the production angles are equivalent for either one, this sign will be ignored throughout the following.

BHABHA SELECTION STRATEGY

Each particle that enters LumiCal initiates an EM shower. It is apparent from Fig. 4 that the vast majority of radiative photons is of low energy, and enters LumiCal in close proximity to the lepton. The multitude of showers, therefore, tends to be highly inter-mixed, and so the typical signature of Bhabha scattering events is the presence of two showers, back to back in the detector.

Since LumiCal has a finite spatial resolution, the first step in the Bhabha selection process is the clustering of showers in each arm of the detector. It has been shown [2] that for the current design of LumiCal, it is possible to separate a pair of showers, provided that

$$d_{pair} \geq R_M \text{ and } E_{sh} \geq 20 \text{ GeV}, \quad (4)$$

where d_{pair} is the distance between the centers of the two showers, and E_{sh} is the energy of each of the showers.

In the present design of LumiCal there is no way to distinguish between EM showers initiated by leptons and those started by photons. One may, therefore, consider instead the cluster which has the highest energy in each arm, and impose on it the Bhabha selection cuts. Only clusters which are fully contained within LumiCal are considered. The set of selection cuts used in the following study [5] are

$$\frac{|E_r - E_l|}{\min\{E_r, E_l\}} \leq 10\%, \quad E_r, E_l \geq E_{beam} \cdot 80\%,$$

$$|\theta_r - \theta_l| \leq 1 \text{ mrad} \quad \text{and}$$

$$\theta_{\min}^f \leq \theta_r, \theta_l \leq \theta_{\max}^f \quad (5)$$

where E_r and E_l (θ_r and θ_l) are, respectively, the energy (polar angle) of the highest-energy cluster in the right and left arms of LumiCal.

The application of the Bhabha selection cuts reduces the counting rate of Bhabha events. In order to measure the luminosity, one must know the exact value of the selection efficiency. The efficiency is defined as

$$\varepsilon_{Bh} = \frac{N_{Bh}(cut)}{N_{Bh}(all)}, \quad (6)$$

where $N_{Bh}(all)$ is the number of Bhabha events which are analyzed, and $N_{Bh}(cut)$ is the number of events which pass the selection cuts.

THE SHAPE OF THE BEAMPIPE

In the current detector layout the beampipe, which is made of Beryllium, has a so called conical shape. The inner radius close to the IP ($Z = 0$) is small, so as to accommodate the vertex detector. At larger distances from the IP, up to the first layer of LumiCal ($Z = 2,27 \text{ m}$), the radius increases, as illustrated in Fig. 5.

This design has the benefit that particles which enter LumiCal do not pass through any

material beforehand. On the other hand, this configuration has several deficiencies. For one, it is difficult to maintain the vacuum inside the beampipe around the edges of LumiCal, where the radius of the beampipe is large. Another difficulty lies in the power-loss as a result of high order EM modes [11]. In addition, the conical shape of the beampipe may cause disturbances of the magnetic field around LumiCal.



Figure 5. Schematic design of the conical shape of the beampipe in the current detector design. LumiCal is denoted in the figure.

In order to prevent these problems an alternative, so called parallel, shape of the beampipe is proposed. In this case the Beryllium beampipe has uniform inner and outer radii of 5.5 and 6 cm respectively. The design of the parallel shape is illustrated in Fig. 6.



Figure 6: Schematic design of the proposed parallel shape of the beampipe. LumiCal is denoted in the figure.

The downside of the parallel configuration is the fact that particles which enter LumiCal may preshower, as a result of the passage through the material of the beampipe. Since particles which enter LumiCal traverse the beampipe at $Z > 65 \text{ cm}$, the structure of the beampipe near the IP does not affect the luminosity measurement. One may, therefore, choose a different design at low Z in order to clear space for the vertex detector. The current configuration was chosen for its simplicity.

Figure 7 shows the correlation between the position relative to the IP of the creation of particles, Z_0 , and the energy of the created particle. Both the conical and the parallel configurations were simulated, using 10^4 Bhabha events. For the conical configuration no particles are created between the IP ($Z = 0$) and the first plane of LumiCal ($Z = 2,27 \text{ m}$), while for the parallel design, this is not the case. The rate of particle creation as a function of the distance from the IP is in accordance with the polar angular dependence of the Bhabha scattering cross section (see Eq. (1) and Fig. 3).

We shall refer to particles which were generated according to the Bhabha cross section at the IP, as primary particles. Particles which were created in the simulation due to pre-showering in the material of the beampipe ($Z_0 > 0$) will be referred to as secondary particles. A primary parent of a given secondary particle is defined as the

primary particle that initiated the shower, in which the secondary was created.

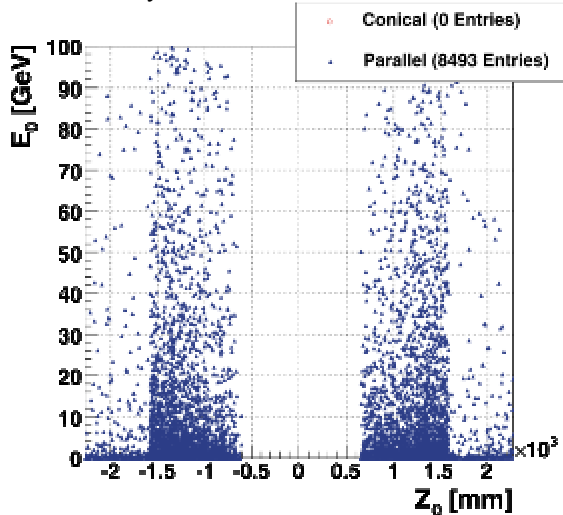


Figure 7. Correlation between the position relative to the IP of the creation of particles, Z_0 , and the energy of the created particle, E_0 . Both the conical and the parallel configurations were simulated, as indicated in the Figure, using 10^4 Bhabha events.

Figure 8 shows the correlation between the polar angle of particles which enter LumiCal and the energy of the particles. Both the conical and the parallel configurations were simulated, using 100 Bhabha events. Each sample is divided into groups of primary and secondary particles. One can observe two differences between the parallel and conical configurations. For one, secondary particles are created only in the parallel configuration. In addition, the polar angle of primary particles changes on occasion, due to momentum transfer to the secondary particles.

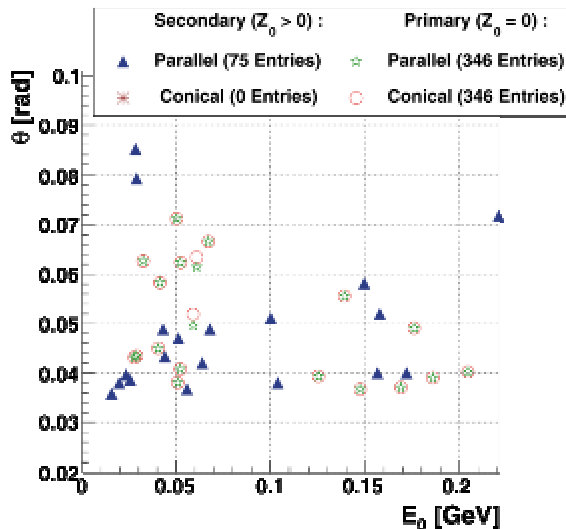


Figure 8: Correlation between the polar angle of particles which enter LumiCal, θ , and the energy of the particles, E_0 , for a data sample of 100 Bhabha events. Both the conical and the parallel configurations were simulated, as indicated in the Figure. Each sample is divided into groups of primary ($Z_0 = 0$) and secondary ($Z_0 > 0$) particles.

COMPARISON BETWEEN THE TWO DESIGNS OF THE BEAMPIPE

In order to estimate the effect on the luminosity measurement of changing the shape of the beampipe, it is necessary to know the change in the counting rate of Bhabha events between the two designs. The relative bias in the measurement would then be given by Eqs. (2) and (3), with

$$N_{gen} \rightarrow N_{con} \text{ and } N_{rec} \rightarrow N_{par} \quad (7)$$

where N_{con} and N_{par} are, respectively, the number of Bhabha events in the conical and parallel configurations.

It is helpful to begin by performing a case-by-case comparison of the two configurations. For any given event, either the two designs yield the same result (success or failure of the cuts), or in one configuration the event passes the cuts while in the other it does not. Possible differences between the two designs for a hypothetical sample of five Bhabha events are given in Table 1. In this example, the final selection efficiency, ϵ_{Bh} , is 60% for the conical design, and 40% for the parallel design. Subsequently, the relative bias in luminosity between the two configurations is $\Delta\mathcal{L}/\mathcal{L} = 33\%$.

Table 1: Success (\checkmark) or failure (\times) of the Bhabha selection cuts for the conical and parallel designs, using a hypothetical sample of five Bhabha events.

Event index	Success/failure of selection cuts	
	Conical	Parallel
1	\checkmark	\checkmark
2	\times	\times
3	\checkmark	\times
4	\times	\checkmark
5	\checkmark	\times

It should be noticed that despite the fact that there is a miss-match between the two configurations in three cases out of five, two of the mismatches cancel out, and the final difference is one case out of five. This example reflects the results which were obtained for the generated sample of 10^6 Bhabha events. The entire sample was divided into groups of 10^3 events. For each event, clustering was performed in each arm, and the clusters were subjected to the selection cuts.

It is convenient to define the variable $N_{par}^{(\checkmark)}$, which counts the number of events out of a single group of 10^3 events, in which the Bhabha selection cuts passed in the parallel configuration, but not in the conical. Similarly, $N_{par}^{(\times)}$ counts the number of individual failures of the selection cuts in the parallel configuration.

Figure 9 shows the correlation between $N_{par}^{(\vee)}$ and $N_{par}^{(\times)}$ for the entire sample of 103 groups of 10^3 events. For many of the event groups $N_{par}^{(\vee)} = N_{par}^{(\times)}$. This means that even though there are mismatches in the selection efficiency on a case-by-case basis, the total efficiency for the entire group of 10^3 events is the same for both configurations. For bins with $N_{par}^{(\vee)} \neq N_{par}^{(\times)}$ there is an accumulated mismatch. This produces a bias in the selection efficiency, since the total number of events which passed the cuts in the two configurations is not the same.

In Fig. 10 is shown the distribution of the relative bias in the Bhabha counting rate,

$$\delta\mathcal{N} = (N_{par} - N_{con})/N_{con},$$

for each event group. The values of the mean and of the root-mean-square of the distribution are $(1 \pm 2) \cdot 10^{-4}$ and $(6.6 \pm 0.2) \cdot 10^{-3}$ respectively⁴.

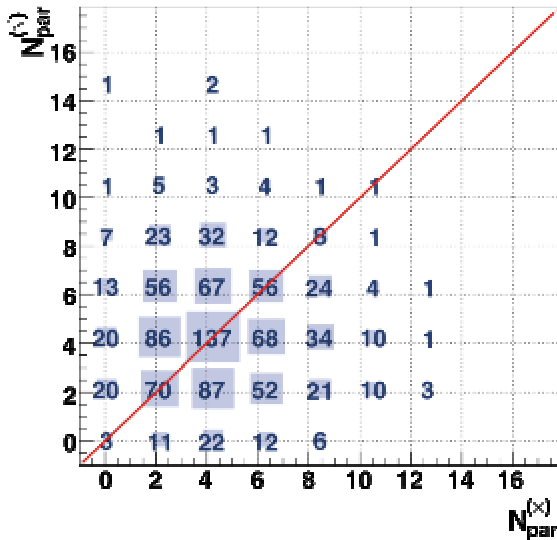


Figure 9: Correlation between the number of individual success, $N_{par}^{(\vee)}$, and the number of individual failures, $N_{par}^{(\times)}$, of the Bhabha selection cuts in the parallel configuration, out of groups of 10^3 Bhabha events. In total 10^3 such event groups were considered.

The small bias in the counting rates is accounted for by the fact that for large data samples, the event-by-event differences in ε_{Bh} tend to cancel out. As explained above, the difference between the two configurations is the addition of secondary particles, which are created due to passage of the primary particles through the beampipe. The fact that clustering is employed serves to lessen the divergences of the parallel configuration from the conical. This is due to the fact that most of the secondary particles are of low energy, and enter LumiCal in close proximity to

their respective primary parents. As such, the showers of the secondary particles are often clustered into those of their primary parents.

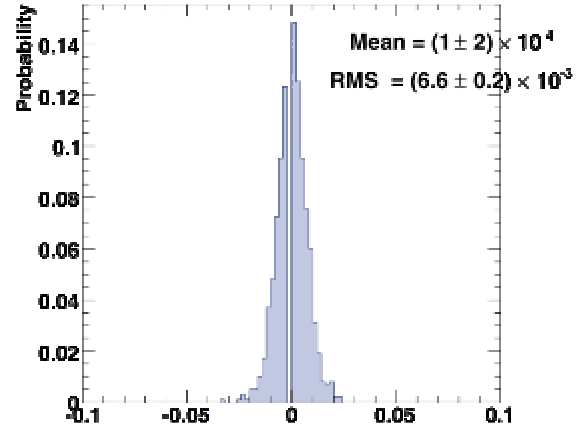


Figure 10. Distribution of the relative bias in the Bhabha counting rate, $\delta\mathcal{N}$, as a result of the change in the design of the beampipe. Each entry represents the value of $\delta\mathcal{N}$ for a group of 10^3 Bhabha events.

The main effect, therefore, comes down to a small change in the reconstructed position of clusters, relative to the respective clusters, which would have been reconstructed in the conical configuration. The secondary particles either increase or decrease the reconstructed polar angle of the highest energy clusters with equal probability. This effect, therefore, sometimes serves to increase and sometimes to decrease the value of $|\theta_r - \theta_l|$. Clusters are also pushed into or out of the fiducial volume of LumiCal in the same frequency.

Differences in the energy of clusters between the two configurations may also occur, as on occasion the shower initiated by a secondary particle is clustered along with a shower which was not a product of the respective primary parent. Another factor that should be considered is the loss or gain of energy in each arm of LumiCal. This may happen when a particle enters the fiducial volume of LumiCal in one configuration, but not in the other. Since the selection cut on energy is relatively loose, these effects are less significant than the changes in polar angle.

SUMMARY

In order to resolve problems relating to the magnetic field and to the vacuum system, an alternative design of the beampipe has been suggested. In the new configuration, particles which enter the luminosity calorimeter traverse the material of the beampipe beforehand. As a result secondary particles are created due to pre-showering.

The amount and characteristics of pre-showering is determined by the thickness and composition of the beampipe. It has been shown

⁴ The errors on the fit results are determined by statistics, and may be reduced by considering a larger data sample.

that, for the proposed design, this effect induces a relative bias of $O(10^{-4})$ in the efficiency of the Bhabha selection process. This, in turn, produces a relative bias of the same order in the luminosity measurement.

The conclusion, therefore, is that the error in the luminosity measurement due to the bias can be controlled. In order to accomplish this, the study which was described here would have to be repeated with a much larger data sample. In this way the error on the fit of the mean value of δN may be reduced to an acceptable level. Further study is also needed in order to determine the dependence of the bias on the choice of Bhabha selection cuts and on the effectiveness of the clustering procedure.

ACKNOWLEDGMENTS

This work is partly supported by the Commission of the European Communities under the 6th Framework Programme “Structuring the European Research Area”, contract number RII3-026126, and by the Israeli Science Foundation.

REFERENCES

- [1] Moenig K., Physics Needs for the Forward Region, Talk given at the Zeuthen FCAL meeting, Aug. 2004.
- [2] Sadeh I., Luminosity Measurement at the International Linear Collider, URL: http://alzt.tau.ac.il/~sadeh/mscThesis/iftachSadeh_mscThesis.pdf, 2008
- [3] Caffo M. et al., Bhabha Scattering, Z Physics at LEP1, CERN Report 89-08, 1, 1989. URL: http://documents.cern.ch/cgi-bin/setlink?base=cernrep&categ=Yellow_Report&id=89-08_v1.
- [4] Stahl A., Luminosity Measurement via Bhabha Scattering: Precision Requirements for the Luminosity Calorimeter, LC-DET-2005-004, 2005. URL: <http://www-flc.desy.de/lnotes/notes/LC-DET-2005-004.ps.gz>.
- [5] Ingbir R., A Luminosity Detector for the International Linear Collider, URL: <http://alzt.tau.ac.il/~ronen/>, 2006.
- [6] Abramowicz H. et al., A Luminosity Detector for the International Linear Collider, LC-DET-2007-006, 2007. URL: <http://www-flc.desy.de/lnotes/notes/LC-DET-2007-006.pdf>.

[7] Abramowicz H. et al., Redefinition of the Geometry of the Luminosity Calorimeter, EUDET-Memo-2008-09, 2008. URL: <http://www.eudet.org>

[8] MOKKA - a detailed GEANT4 detector simulation for the Future Linear Collider, URL: <http://polywww.in2p3.fr/geant4/tesla/www/mokka/mokka.html>.

SILICON SENSORS FOR LUMICAL

Status Report

By

Wojciech WIERBA,
J. BŁOCKI, W. DANILUK, A. GALAS, E. KIELAR, J. KOTUŁA, A. MOSZCZYŃSKI, K.
OLIWA, B. PAWLIK, L. SUSZYCKI¹, L. ZAWIEJSKI

Institute of Nuclear Physics PAN, Cracow, Poland
(1) AGH University of Sciences and Technology, Cracow, Poland

Two calorimeters, called for short LumiCal, located in very forward region of the future detector at the International Linear Collider, are proposed for the precise luminosity measurements based on the Bhabha scattering process. For this purpose, the precise measurement of the scattering polar angles is crucial. A silicon–tungsten sandwich calorimeter with fine–segmented silicon sensors has been designed. This paper describes current design of silicon sensors for the LumiCal prototype based on available silicon technologies and status of sensors manufacturing.

Key words: silicon sensors, pad, strip, bias voltage, dark current, leakage current, fan out, Kapton.

INTRODUCTION

In the future detector for the International Linear Collider ILC [1], the very forward region is a particularly challenging area for instrumentation. The LumiCal detector [2] is expected to give the required precision of 10^{-4} luminosity measurement and to extend calorimetric coverage of small angles from ~ 40 to ~ 80 mrad. The luminosity measurement will be based on detection of Bhabha event rate. The precise measurement of the scattering polar angles [3] requires fine segmented silicon sensors and an ultimate precision in detector mechanical construction and metrology [4].

SILICON SENSORS

The proposed LumiCal detector will consist of 30 layers of tungsten of 1 radiation length thickness and $320 \mu\text{m}$ silicon sensors layers. The sensitive region extends from 80 mm to 195.2 mm in radius. Each such layer will include 48 azimuthal sectors. The sector will be segmented into 64 radial pads with a constant pitch of 1.8 mm. The sensor plane will be built from a few tiles because the current technology is based on 6-inch wafers. One silicon sensors half plane is shown in Fig. 1. The tiles of the silicon sensors will be glued to a thin Kapton foil placed directly on a tungsten surface for electrical insulation. Reference marks are foreseen on the detector surface for precision positioning. The layout of the sensors and the mechanical design of the calorimeter does not allow sensor to overlap. To reduce the impact of the gaps odd and even

planes are rotated by 3.75° . The silicon diodes will be usual planar high resistive silicon sensors. Figure 2. shows one silicon detector of the proposed structure of 4 sectors and 64 pads in radius. To cover one full plane of the LumiCal 12 silicon tiles with 3072 pads are needed.

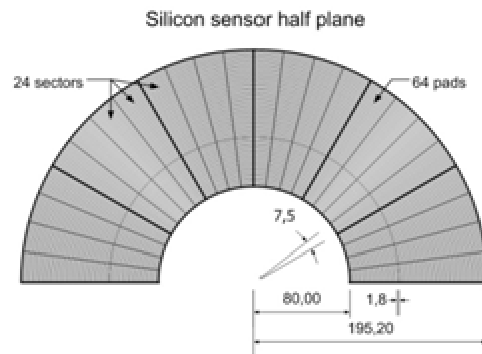


Fig. 1. Silicon sensors half plane

The mechanical gap (clearance) between every two tiles is foreseen to be 0.1 mm as shown in Fig. 3. Counting also the guard rings of 0.6 mm wide and roughly 0.6 mm clearance for wafer cutting, the inactive gap between the tiles has a width of ~ 2.5 mm. This gap width has to be taken into account in the MC simulations. The azimuthal gaps are staggered by rotation for odd and even layers of the detector.

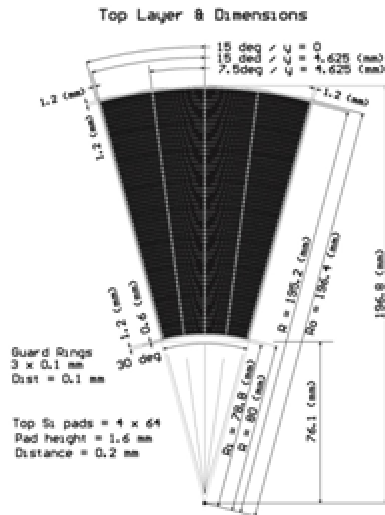


Fig. 2. The proposed segmentation of the silicon sensor.

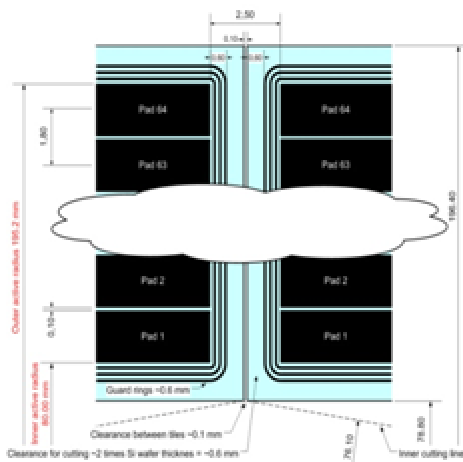


Fig. 3. Detailed drawing of the gap between tiles.

In collaboration with Hamamatsu firma the set of masks has been designed, produced and already paid. In Figs. 4 and 5 the more detailed drawings of the design are presented.

The basic parameters for silicon sensors are:

- N-type silicon, p⁺ strips, n⁺ backplane,
- Crystal orientation <100>
- 320 μm thickness ± 15 μm
- Strip pitch 1.8 mm
- Strip p⁺ width 1.6 mm
- Strip Al metallization width 1.7 mm.

Hamamatsu needs roughly 3 month to manufacture sensors, the order is in preparation.

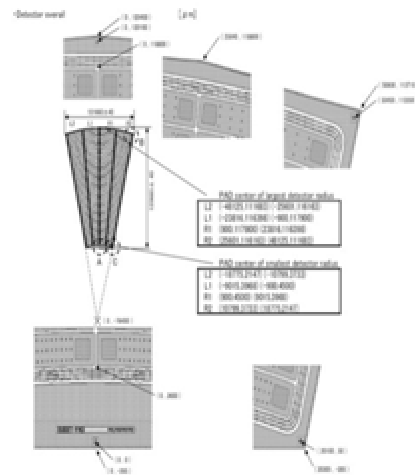


Fig. 4. Detailed drawing of the Silicon Sensors for LumiCal design.

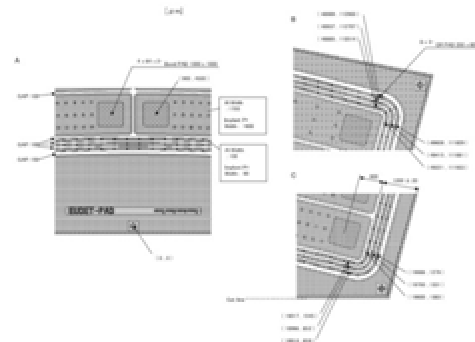


Fig. 5. Details of the design.

FAN OUT

To feed out the charge signals from detector pads we have designed the fan out on 50 μm Kapton foil. Fan out, presented in Fig. 6. covers 4 sectors of detector (one tile) and in present stage has two different traces layout to test the cross talks.

The major problem is to connect electrically fan out traces on Kapton foil with pads of silicon detector. We can not use wire bonding because there is no space in height for it. One solution is bump bonding – quite complicated and expensive technology. We try to solve this problem using electrically conductive glue as shown in Fig. 7.

To be able to play with different glues not using expensive silicon sensors, we have designed ‘dummy’ sensor – pads in silicon sensor shape on standard PCB shown in Fig. 8 left. The fan out glued to the ‘dummy’ sensor is presented in Fig. 8 right.

Fanout
 Pad = 0.1 x 0.16 mm
 Pitch = 0.33 mm
 Trace = 0.050 mm
 Minimum distance = 0.080 mm
 (when GND Trace between Pads)

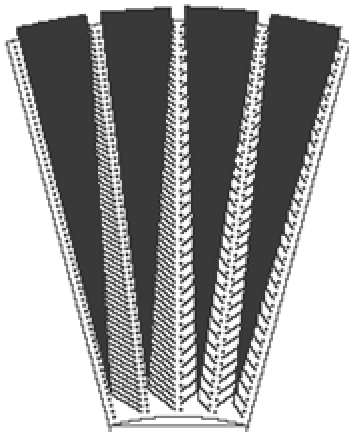


Fig. 6. Fan out.

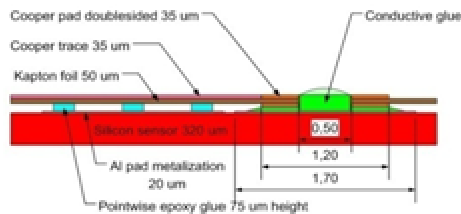


Fig. 7. Cross section of the fan out electrically conductive gluing to sensor pad.

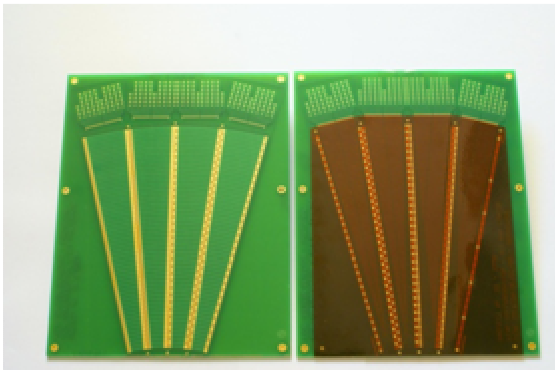


Fig. 8. 'Dummy' sensor on PCB (left), fan out glued to the 'dummy' sensor (right).

CONCLUSIONS

Sensors prototypes hopefully will be ready by the end of this year or in first weeks of 2009.

We are not satisfied with quality of the fan out on Kapton foil produced in one local firm and we have to find and test other PCB manufacturer.

Searching for the proper electrically conductive glue and test it is now a main task. We are in contact with experts from different collaborations trying to use their experience.

REFERENCES

- [1] International Linear Collider:
<http://www.linearcollider.org/cms>;
 Reference Design Report, ILC-REPORT-2007-001.
- [2] TESLA Technical Design Report, DESY 2001-011, ECFA 2001-209, March 2001; H. Abramowicz et al., IEEE Transactions of Nuclear Science, 51 (2004) 2983; R&D for ILC – Detector, Instrumentation of the Very Forward Region, The Forward Calorimetry (FCAL) Group, DESY PRC R&D Report 02/01, April, 2006; Large Detector Concept, LDC outline document: <http://www.ilclde.org/documents>.
- [3] A. Stahl, *Luminosity Measurement via Bhabha Scattering: Precision Requirements for the Luminosity Calorimeter*, LC-DET-2005-004, Apr 2005.
- [4] J. Błocki et al., *Laser measurement of the LumiCal detector displacement*, Report No. [1985/PH](#), 2006, IFJ PAN, Cracow, Poland.

STATUS OF LUMICAL READOUT ELECTRONICS

By

Marek IDZIK¹, Krzysztof SWIENTEK¹, Szymon KULIS¹

(1) AGH University of Science and Technology, Cracow, Poland

The design and measurements of the prototype components (front-end and ADC) of readout electronics for the luminosity detector (LumiCal) at ILC are presented. The prototype were designed and fabricated in 0.35 μm CMOS technology. The proposed architecture comprising switched-gain preamplifier, pole-zero cancellation circuit (PZC) and switched-gain shaper is described. The preamplifier works for a wide range of input capacitance values up to 100 pF. The input charge dynamic range is 0.4 fC to 10 pC and covers more than 4 orders of magnitude. The circuit has to be fast with a peaking time of about 70 ns. The results of measurements on gain and noise are presented. The prototype ADC is 10 bit pipeline with 1.5-stage architecture. The motivation for the chosen architecture is presented and followed by the description of core blocks. Wide spectrum of measurements of static (INL, DNL) and dynamic (SNHR, SINAD, THD) parameters are presented.

Key words: LumiCal, front-end, ADC, readout electronics

INTRODUCTION

In the future International Linear Collider (ILC) the luminosity measurement will be done by LumiCal detector detector which will constitute important part of the Forward Calorimetry region [1]. The project of LumiCal readout electronics depends on several assumptions concerning the

detector architecture. At present development stage it is assumed that the LumiCal detector is built of 30 layers of 300 μm thick DC-coupled silicon sensors and each layer is divided into azimuthal sectors which are segmented into radial strips with a constant pitch. These strips will be connected to the multichannel front-end ASICs. In total about 200,000 channels will need to be readout.

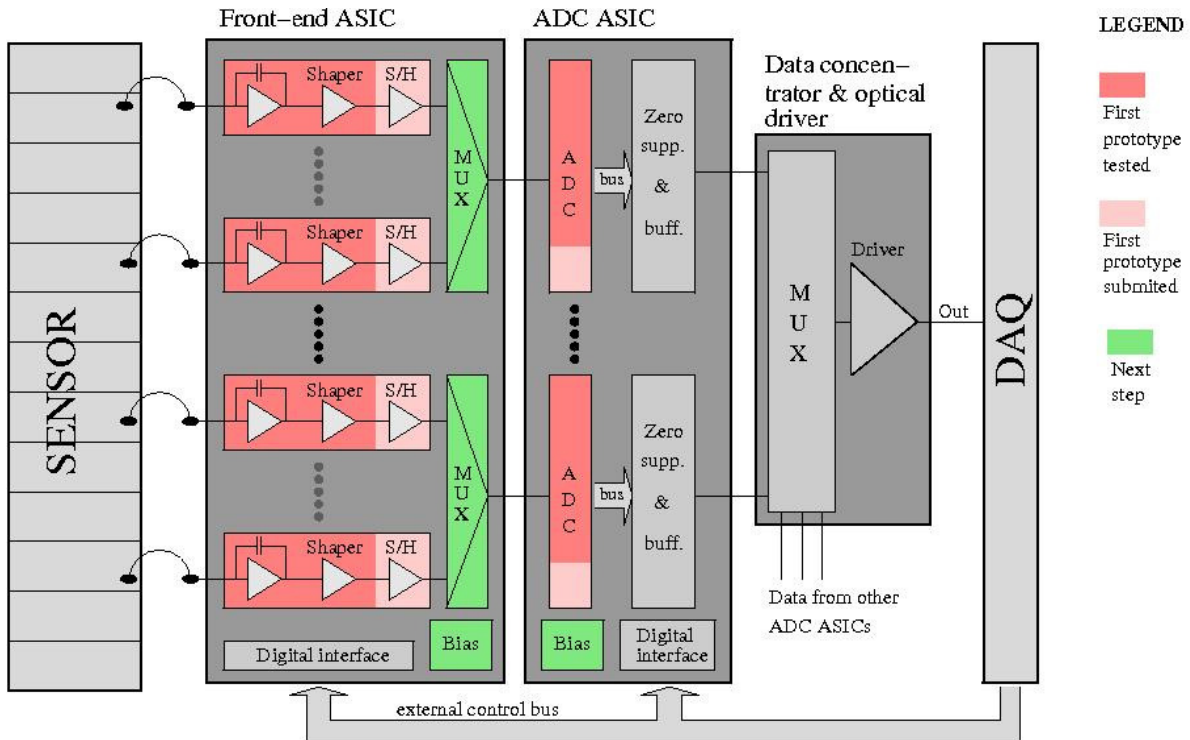


Fig 1. Block diagram of the LumiCal readout electronic

The LumiCal should work in two modes: the physics mode and the test mode. In physics mode the detector should be sensitive to electromagnetic showers with high energy deposition (up to about 15 pC of charge) in a single sensor. In test mode it should detect the signals from relativistic muons, i.e. it should be able to register the minimum ionizing particles (1MIP~4fC). Because of very high expected occupancy the front-end electronics should resolve signals from particles in subsequent beam bunches i.e. within a time distance of about 360 ns. The requirements on power dissipation of front-end electronics can be strongly relaxed if a total or partial power supply switching off will be applied in the periods between the bunch trains.

From the above specifications the general concept of the readout electronics was outlined as shown in fig. 1. The main blocks of the signal chain are: front-end electronics, A/D conversion plus zero suppression and data concentrator with optical driver.

In the following the designs of front-end and ADC are discussed and measurements results are presented. The discussed ASICs were produced in the AMS 0.35 μm four-metal, two-poly CMOS technology through the Europractice service.

FRONT-END ELECTRONICS

To fulfill all the requirements the front-end electronics comprising the charge sensitive amplifier, the pole-zero cancellation circuit (PZC) and CR-RC shaper with peaking time $T_{\text{peak}}=C_i R_i$ were designed, as shown in fig. 2. The “mode” switch changes effective values of R_f , C_f , R_i and C_i components and so changes the front-end gain.

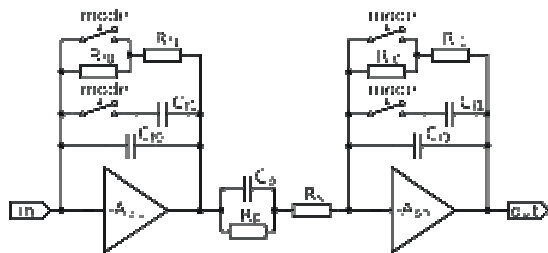


Fig 1. Block diagram of front-end channel

The low gain (large C_f) is used for the physics mode when the front-end processes signals with large charge depositions in a sensor, while the high gain (small C_f) is used in the calibration mode when a MIP sensitivity is needed. Regarding the noise a main requirement was to obtain in calibration mode the signal to noise ratio (S/N) of about 10 even for largest sensor capacitances.

Both of the amplifying stages (A_{pre} , A_{sh}) were designed as folded cascades [2] with active loads and followed by source followers.

FRONT-END MEASUREMENTS

The dimensions of each channel in the ASIC layout are 630 μm x 100 μm . There are 8 front-end channels in the prototype ASIC. Three prototype ASICs were bonded on dedicated PCB boards to test the front-end functionality and to measure their electrical parameters. The power consumption of about 8.9 mW/channel was measured what confirms well the simulations.

In the first measurements the front-end channel response to charge injected through the input test capacitance was observed. These measurements were performed for different values of input capacitance (C_{det}) within the interesting range. The sensor capacitance was simulated with an external capacitor.

In fig. 3 the pulses observed in physics mode for different input capacitances are presented. It is seen that both the amplitude and the peaking time (~70 ns) are not sensitive to the value of input capacitance in this case.

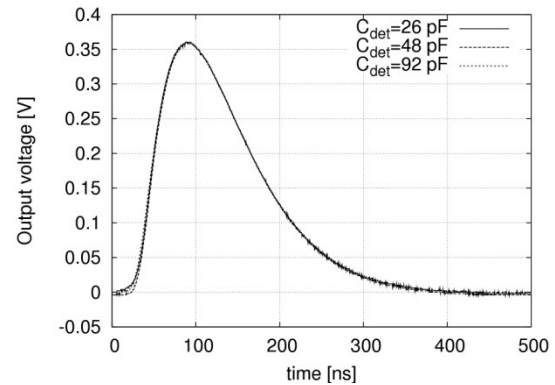


Fig 2. Output pulses from front-end in physics mode

Systematic measurements of charge gain covering full input signal dynamic range were done for a number of channels.

The results are shown in fig. 4 for the physics mode. In that mode the measurements were performed injecting the charge through an external capacitance. This was done because, with the limited voltage step possible to apply (to not damage the ASIC); it was not possible to cover the whole input dynamic range using internal test capacitance (0.5 pF) only. The measurements were done for charge injections up to 15 pC, as seen in fig. 4 for the front-end with active feedback. It is seen that the circuit is linear up to almost 10 pC and saturates for higher charges injected. As expected the channel response is not sensitive to input capacitance value. The measurements are in good agreement with the simulation results which are shown in the same plot.

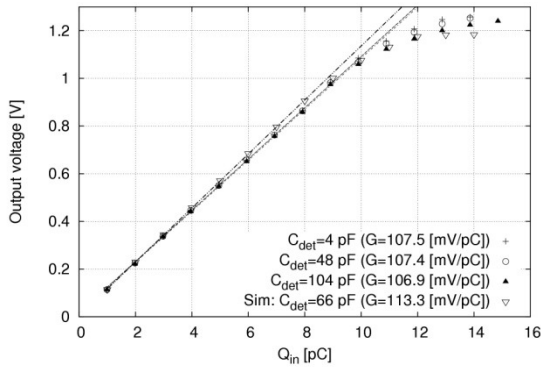


Fig 3. Gain measured in physics mode

Preliminary noise measurements were performed using the HP3400 true RMS meter. The equivalent noise charge (ENC) as a function of input capacitance for both front-end types including physics and calibration mode is shown in fig. 5.

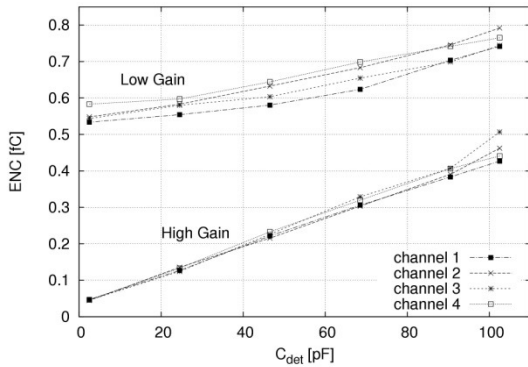


Fig 4. Noise ENC obtained with true RMS meter in physics (low gain) and calibration (high gain) mode

Since the HP3400 bandwidth is only 10 Hz—10 MHz the numbers may be underestimated by about 20%. The ENC vs. C_{det} behavior and the measured values are generally in agreement with simulations. In particular the signal to noise ratio of 10 is maintained up to almost 100 pF. For few points an additional noise measurement was performed by integrating the noise spectra with HP4195A spectrum analyzer. The results of such measurements are added in fig. 5. They agree within about 20% with the HP3400 RMS measurements. For a final confirmation of noise performance measurements with particles impinging a sensor are needed and will be performed as soon as a right sensor is available.

ANALOG TO DIGITAL CONVERTER

Pipeline ADC is built of several serially connected stages as shown in fig. 6. In the proposed solution a 1.5-bit stage architecture was chosen because of its simplicity and immunity to the offsets in the comparator and amplifier circuits. Since single stage generates only three different values coded on 2 bits it is called 1.5-bit stage.

Each stage from fig. 6 generates 2 bits which are sent to digital correction block. In the correction block 18 output bits from 9 stages are combined together resulting in 10 bits of ADC output.

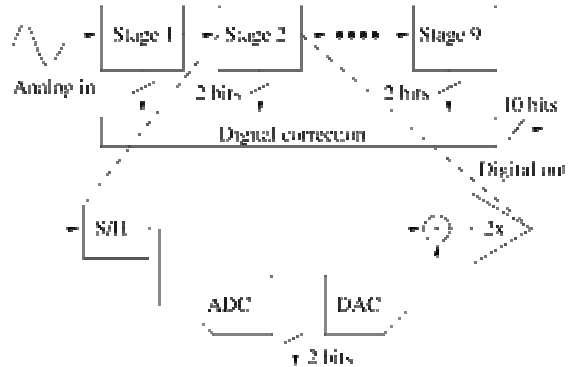


Fig 5. Pipeline ADC architecture

Each 1.5-bit stage was designed in fully differential architecture to improve the ADC immunity to digital crosstalks and other disturbances. It consists of two dynamic latch comparators, two pairs of sampling and feedback capacitors, an fully differential operational transconductance amplifier, several switches and small digital logic circuit.

In the present design only the main core i.e. the eight 1.5-bit stages were implemented. The eight designed pipeline stages are almost identical with the only difference in the values of sampling and feedback capacitances and the current drawn by the amplifiers in the following stages.

ADC MEASUREMENTS

The dimensions of the ASIC are 1.1 x 1.2 mm. The power consumption of the whole analog part was measured to 48 mW independently of sampling frequency. In first tests, the basic functionality was studied with DC input signal. Then the essential static (INL, DNL, missing codes) and dynamic (SNHR, SINAD, THD) parameters were measured.

The Integral Nonlinearity (INL) and the Differential Nonlinearity (DNL) results showed in fig. 7 were measured statically with the ADC sampling frequency of 10 Mhz. These parameters were obtained with histogramming method. The integral nonlinearity was measured to be within ± 3 LSB. The Effective Number of Bits (ENOB) of 6.65 was calculated from the measured INL curve.

Differential nonlinearity stays mostly within ± 0.5 LSB, but there are some codes with larger DNL. Six of the codes with DNL less than -0.9 were identified as missing codes [3]. These 6 missing codes (about 1% of the total) and quite high INL are the main issues to resolve in the present ADC version.

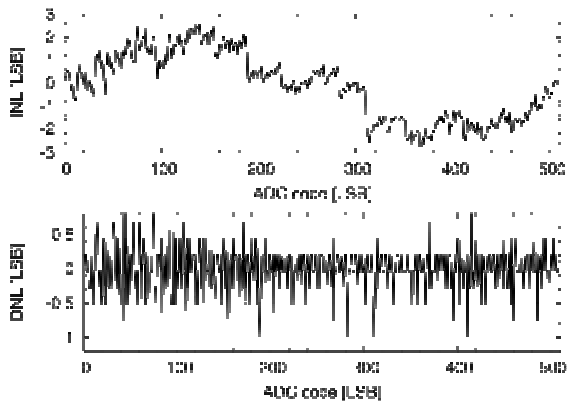


Fig 6. INL and DNL measured statically

To estimate dynamic circuit performance measurements with pure sinusoidal wave (modeled with step signal because of lack of S/H) input were performed [3]. Fast Fourier Transformation (FFT) was used to calculate output signal spectrum. To estimate pure noise level in a circuit Signal to Non Harmonic Ratio (SNHR) is used. The ratio of signal amplitude to all harmonics is called the Total Harmonic Distortion (THD). To determine the overall ADC performance the Signal to Noise and Distortion Ratio (SINAD) is used. Its value is calculated as a ratio of the signal at the input signal frequency to the integral over all frequencies.

The dependence of all discussed above metrics on ADC sampling frequency was also investigated. The results of these measurements are shown in fig. 8.

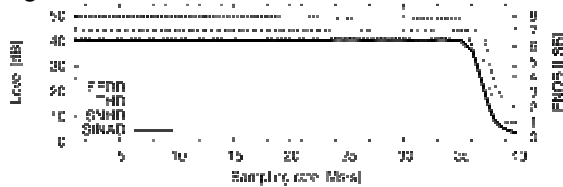


Fig 7. ADC performance as a function of sampling rate

One may conclude that the ADC works stable in a wide frequency range up to 36 Mhz. Above this frequency all the metrics fall due to bandwidth limit of stage amplifier. Below 36 Mhz the SINAD of 40.4 dB is obtained. It is dominated by the harmonic distortions (THD) which is equal to 40.9 dB. It is too low for 8 bit ADC (in the ideal 8 bit case it should be 49.9 dB). Detailed studies showed that such behavior is due to stage gain mismatch (stage gain is lower than 2 which is the expected value). It will be improved in the next version. The SNHR of 49.1 dB was obtained and it is quite promising because it shows that the pure noise level is equivalent to the ideal 8 bit ADC. The effective number of bits (ENOB) calculated from SINAD equals 6.4 which is in good agreement with the results obtained from static measurements.

Digital calibration procedure was also investigated (or rather its mathematical equivalence because of lack of appropriate circuitry in ADC).

Using this procedure missing codes can be eliminated with simultaneous increase of static ENOB to 7.8 LSB.

CONCLUSIONS

The first prototypes of the front-end electronics and critical analog blocks of a pipeline ADC for the LumiCal detector were designed, fabricated and tested. Tests confirm expected functionality of both LumiCal readout electronic parts.

Front-end quantitative measurements regarding gain, noise and peaking time are in agreement with Hspice simulations. In order to fully verify the performance of the prototypes further measurements in realistic conditions, i.e. with sensors and impinging particles, are needed.

Key static (INL, DNL) and dynamic (SNHR, THD, SINAD) ADC parameters were measured. The proper ADC functionality for sampling frequency up to 36 MHz was verified. The measured noise represented by the SNHR shows expected 50 dB performance for 8 stages. Work is still needed to improve the linearity (THD, INL, DNL).

REFERENCES

- [1] H. Abramowicz et al., "Instrumentation of the very forward region of a linear collider detector", *IEEE Trans. Nucl. Sci.*, vol. 51, pp. 2983-2989, Dec. 2004.
- [2] E. Gatti, P. F. Manfredi, "Processing the Signals from Solid-State Detectors in Elementary-Particle Physics", *Revista Del Nuovo Cimento*, vol 9, 1986, 1-146.
- [3] "IEEE standard for terminology and test methods for analog-to-digital converters", IEEE-STD-1241, 2000.

Beam Calorimeter and pair monitoring

DEVELOPMENT OF CHARGED PARTICLE DETECTORS ON THE BASE OF MONOCRYSTALLINE DIAMOND OF MINSK PRODUCTION

By

Konstantin AFANACIEV, Igor EMELIANTCHIK, Alexandr IGNATENKO, Alexander LITOMIN, Vitaly SHEVTSOV

National Center of Particle and High Energy Physics, Minsk, Belarus

HPHT (high pressure high temperature) diamond is successfully tested as particle detector material. Thermobaric processing of the diamond is shown to improve its detector quality. Selection of the crystals with help of optic spectrometry and photoconductivity spectra is discussed. Preliminary tests of nitrogenless HPHT diamond are described.

Key words: HPHT diamond, CVD diamond, International Linear Collider, ATLAS

INTRODUCTION

Diamond is still a very attractive detector material due to its extremely high radiation hardness. It is planned to be used not only in the International Linear Collider. A possibility of developing of diamond version of ATLAS central tracker is being considered currently because the current tracker will not endure the whole time of ATLAS use. Except of particle physics diamond detectors are needed in medicine, nuclear power production, space research.

Unique strength of atomic binding in the crystal and no necessity to form a backward-biased p-n-junction provide diamond with maximal radiation hardness of all known detector materials. Tests confirmed ability of diamond detectors to endure irradiation doses up to 10MGy [1, 2, 3] without significant degradation of detector quality.

Three types of diamonds are being studied currently as possible detector materials, CVD-poly, CVD-mono and HPHT (high pressure high temperature) differ strongly from one another in many parameters. The main advantage of polycrystalline CVD plates is big area, but the presence of the intercrystalline borders causes strong dependence of response amplitude on the place of particle hit, thus decreasing the energy resolution significantly. Moreover, intercrystallite boundaries are areas of high density of structural defects whose properties change significantly with dose accumulation which results in distortion of proportionality between consumed energy and response amplitude, which is very undesirable in case of calorimetric application. CVD-mono combines advantages of the CVD process (a possibility to provide very high purity, because purification of initial gas mixture presents no problems) and absence of intercrystallite boundaries. Detector properties of such material are

very high. But it is too expensive currently. HPHT is a compromise – a monocrystal for reasonable money. It is impossible to reach the high purity of CVD-mono here, but HPHT is an industrial technology already, and the price of such crystals is hundred times less than that of CVD-mono.

Necessity of diamond detectors exists in many fields of science and technology. In particle physics it is caused by the need of registration of complete interaction picture, including particles and jets going at small angles in relation to beam, where radiation load is extremely high. In accelerator technology detectors are needed for beam monitoring systems able to work for a long time being located very close to the beam. For medicine the other diamond property is important – tissue equivalence and biocompatibility [4, 5, 6]. Chemical inertness and ability to work at high temperatures make diamond attractive for monitoring and processing of radioactive waste [7]. Possibility of space applications is also being studied now [8, 9].

Efforts of researchers are mainly concentrated at CVD-diamond currently. However, HPHT diamond also attracts attention as a possible detector material [10, 11]. These articles describe a possibility of medical use of diamond detectors made with HPHT technology.

HPHT technology developed in the middle of last century initially was using large presses which made diamond synthesis expensive and inefficient. However, a method of diamond synthesis with multianvil high pressure “split-sphere” apparatus, compact, economic and efficient, has been developed later [12 – 14]. Exactly this method is implemented at Minsk plant “Adamas.

GENERAL PRINCIPLES AND APPROACHES IN DIAMOND DETECTOR DEVELOPMENT

Wide bandgap of the diamond guarantees small leakage current (a fraction of picoampere) at usual detector dimensions without special techniques typical for silicon technologies (reverse biased p-n-junctions, guard rings etc.). An ideal diamond detector functions like a solid state ionization chamber, constituting a parallel-sided plate with metal electrodes to create electric field. The real situation is more complicated because impurity atoms, inevitably present in diamond, are limiting the lifetime of free charge carriers, defective surface layer (produced during diamond slicing into plates) causes creation of undesirable space charge (which modifies the applied electric field), and metal-semiconductor contact constitutes Shottky diode in general case, which also leads to irregular field distribution inside the diamond plate. So the next conditions (at least) should be satisfied for creation of effective diamond detector: a) minimization of defects and impurities which reduce life time of free charge carriers; b) thorough surface processing to guarantee removal of defective layer and absence of microcracks; c) special metallization procedure which provides creation of nonrectifying ohmic contact.

Main impurities of the diamond synthesized with temperature gradient method are nitrogen and the metal used as a melted catalyst. Concentration of these impurities depends on the choice of the certain system of metals- catalysts, because both solubility of the metal in crystal and solubility of the nitrogen in metal vary widely for different metals. Furthermore, "gettering" is possible, that is binding of the nitrogen with special additives to reduce its final concentration in the crystal. Melted iron-nickel or iron-cobalt environments are mainly used at "Adamas" plant for the catalytic diamond synthesis. Nickel and cobalt have different solubilities in diamond. Moreover, they form impurity sites of the Me - X type, which have carbide or nitride nature, and differently influence the life time of free charge carriers. So the optimal choice of catalytic environment is one of the most important factors defining the final quality parameter of diamond detector - charge collection distance.

Surface processing of the diamond plate before metallization requires special techniques. Standard silicon processing techniques (chemical-mechanical polishing in etching water solutions, for example) are impossible here due to extraordinary hardness of the diamond. One of rather simple methods of the chemical polishing of the diamond plates is etching in the melted nitre at 700°C. This method allows

etching several tens of nanometers, having thus removed rough defects. Thermochemical processing is a more sophisticated technology which consists of contact dilution of surface diamond layer in transition metals (Fe, Ni, Co etc.) at 700...1200 °C and subsequent gasification of the carbon in hydrogen atmosphere. This method allows to reduce surface roughness down to $R_z = 0.025\mu\text{m}$.

Deposition of carbide-forming metal sublayer is obligatory at metallization stage because it allows to resolve two problems at once: to provide good adhesion (because carbon for the carbide formation is taken out of the diamond bulk) and ohmic contact. Very important also is to prevent partial graphitization (carbidization is performed at high temperature) of crystal edges, otherwise large leakage currents can occur.

MONOCRYSTALLINE PARTICLE DETECTORS BASED ON THE MINSK SYNTHETIC DIAMOND

Diamond crystals are synthesized at "Adamas" plant with temperature gradient method in the environment of melted metal- catalyst (Fig. 1). Multianvil "split-sphere" apparatuses are used to create high pressure at high temperature. Fe-Ni catalytic environment is usually used. The pressure is 5.5 – 5.8 GPa, the temperature is 1550 – 1650 °C.



Figure 1. Typical diamond crystal synthesized with temperature gradient method at "Adamas" plant.

Crystals are cut into 5x5 mm² plates are readily available now, so a 1cm² detector can be made out of 4 such plates. Typical plate thickness is 500μm, but thinner plates (down to 200μm) are available.

Plates are metallized then by thermal sputtering of titanium and gold with subsequent annealing for carbidization (Fig. 2). Detector depicted at Fig. 2 has been tested with β-particles of ⁹⁰Sr radioactive source.

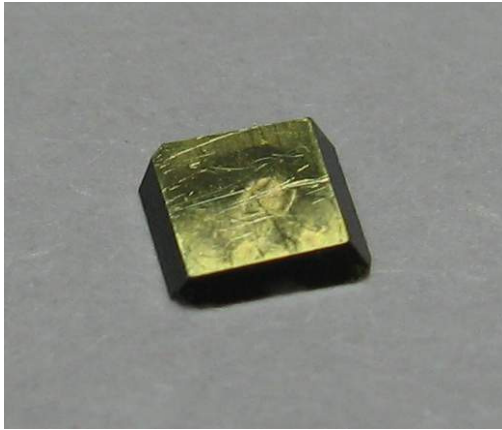


Figure 2. Metallized diamond plate ready to be tested as particle detector.

DETECTOR BASED ON THE THERMOBARICALLY PROCESSED DIAMOND

The main defects limiting life time of free charge carriers are impurity atoms. The main impurity in diamond is nitrogen. Majority of synthetic diamonds have nitrogen in replacing position (C-defect) thus belonging to type Ib.

The most commonly used method of modification of diamond monocrystal defect structure is thermobaric processing, performed at conditions providing diamond stability. It's shown in [15-17] that conversion of C-form of impurity nitrogen into A-form is going on during annealing of Ib diamond at $P = 6.0 \div 6.5$ GPa and $T = 1700 \div 2100$ °C.

So we have performed thermobaric processing of our samples using the same high pressure apparatus, which had been used for the synthesis. Stabilizing pressure was 6.7GPa, temperature 1800°C, duration 4 hours.

Five annealed samples behaved differently, the most pronounced positive effect has been demonstrated by the sample 219. Its response to β -particles before and after annealing is shown at Fig.3.

CRYSTAL SELECTION BASED ON THE OPTICAL ABSORPTION SPECTRA

Nitrogen concentration in diamond can be evaluated by the position of absorption edge at the violet area of optical absorption spectrum. The more to the lower wavelengths stretches the absorption edge (to higher wavelength for transition edge), the less is nitrogen content. So we have assembled an optical spectrometric stand for assessment of transition spectra of diamond crystals (Fig. 4).

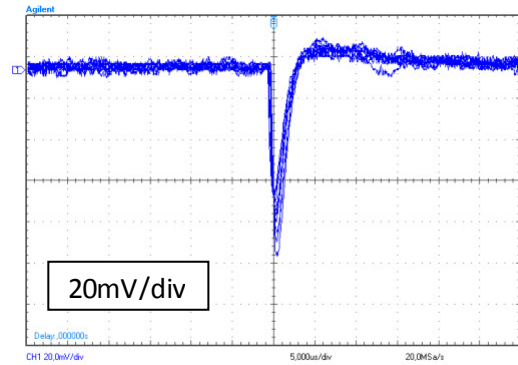
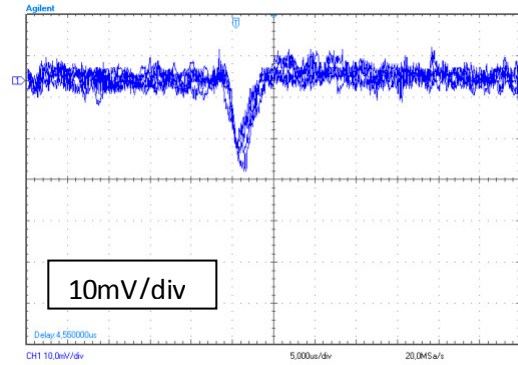


Figure 3. Response to β -particle of diamond detector (sample 219) before (top) and after thermobaric processing.

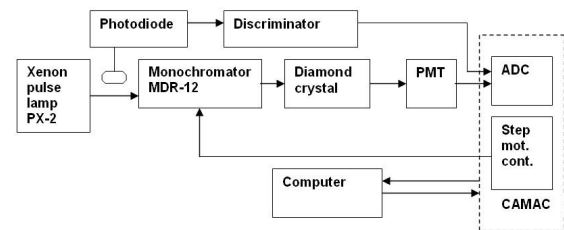


Figure 4. Optical stand for evaluation of nitrogen content in diamond crystals.

Then we have taken 8 diamond crystals and measured absorption spectra (Fig. 5). It is seen that crystals are really differing from one another by the position of absorption edge. We have taken the best crystal (#3726) and made a detector out of it. It worked a bit better than detectors made without crystal selection. So the method seems to be promising.

There is no photoconductivity in ideal diamond if the energy of incoming photon is less than the bandgap (5.5eV). However, in the real case, there are always impurity atoms and structural defects which are energy levels inside the bandgap. So photoconductivity can be induced even by photons with smaller (than 5.5eV) energy. It is reasonable to suppose that it is possible to make some conclusions about detector quality of a certain diamond with help of its photoconductivity spectrum. So we have transformed a bit our optical stand having used the diamond itself (with a charge

sensitive amplifier) as a photosensor. Then we took two diamond plates, #2243 and #3485, and measured their photoconductivity spectra (Fig. 6).

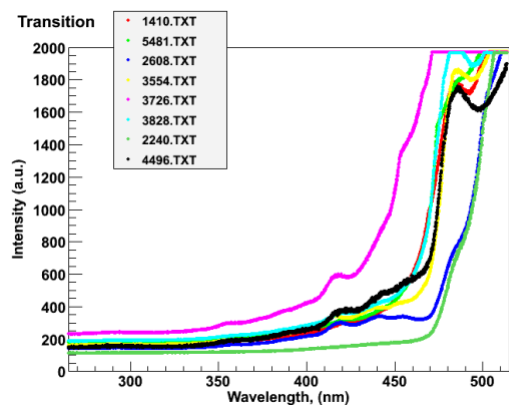


Figure 5. Optical transparency spectra of eight diamond crystals.

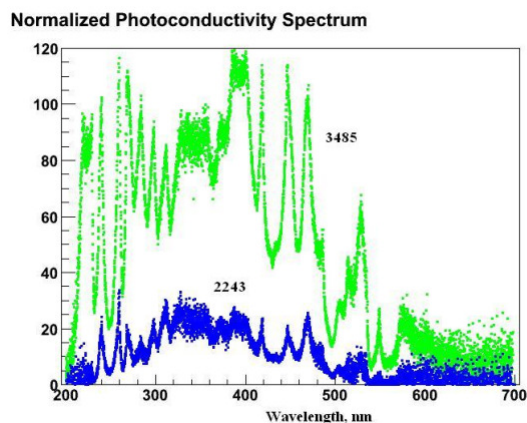


Figure 6. Photoconductivity spectra of the samples #2243 and #3485 taken at the same conditions.

The sample #2243 worked as a detector, the sample #3485 did not. The photoconductivity of #3485 is significantly larger, which means it contains more impurities. So it is quite logical that this sample is less suitable for detector applications. We hope such an approach can help with selection of suitable crystals.

WHITE (NITROGENLESS) DIAMONDS

There is no standard technology of nitrogenless diamonds production at “Adamas” plant. However, experiments have been performed in this area.

We have measured absorption spectrum at shortwave edge of the visual range of one of these diamonds and compared it with a similar spectrum of a typical diamond. Spectra are given at Fig. 7.

As the position of the shortwave edge of absorption spectrum is determined by the nitrogen content, it is seen that the experimental sample does really contain much less nitrogen, than the typical

one. “Adamas” specialists evaluate it to be about 10^{17} atom/cm³. Unfortunately, we were unable to test white diamonds as detectors because of large conductivity caused, most probably, by noncompensated boron impurity. Recently experimentation with white diamonds was renewed at “Adamas” (at our request), so we hope to test it as a detector in the nearest future.

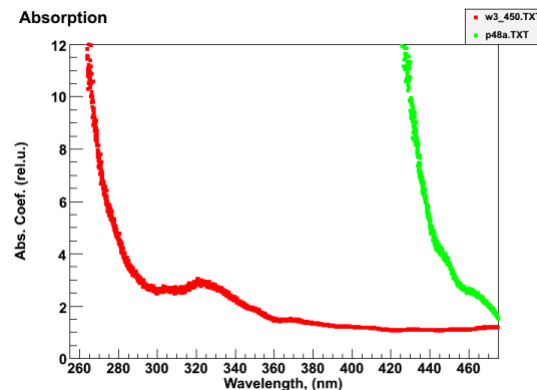


Figure 7. Absorption spectra of white (in red) and typical yellow (in green) diamonds.

CONCLUSIONS

Test samples of particle detectors on the base of HPHT synthetic diamond confirmed applicability of this material as a detector medium. Additional thermobaric processing is able to improve detector quality of the diamond. Crystal selection with help of optic spectrometry can help to choose the most suitable diamonds. Correlation between diamond photoconductivity and detector performance can also be used for crystal selection. Work with white (nitrogenless) diamond is started, which can lead to even better detector material.

REFERENCES

- [1] Behnke T., Doucet M., Ghodbane N., Imhof. A. *Radiation hardness and linearity studies for a diamond luminosity calorimeter LC-DET-2002-001*.
- [2] Bauer C et al. *Radiation hardness studies of CVD diamond detectors*. Nucl Instrum. Methods A 1995 367 207-11.
- [3] Zoeller M M et al. *Performance of CVD diamond microstrip detectors under particle irradiation*. IEEE Trans. Nucl. Sci. 1997 V44 1705-7.
- [4] C.M. Buttar et al. *A study of radiotherapy dosimeters based on diamond grown by chemical*

vapour deposition. Diamond and Related Materials 9 (2000) 965–969.

[5] A.J.Whitehead et al. *CVD diamond for medical dosimetry applications*. Nuclear Instruments and Methods in Physics Research A 460 (2001) 20 – 26.

[6] C.Manfredotti et al. *CVD diamond microdosimeters*. Nuclear Instruments and Methods in Physics Research A 458 (2001) 360 – 364.

[7] A.Brambilla et al. *CVD diamond gamma dose rate monitor for harsh environment*. Nuclear Instruments and Methods in Physics Research A 458 (2001) 220-226.

[8] E.Pace, A. De Sio. *Diamond detectors for space applications*. Nuclear Instruments and Methods in Physics Research A 514 (2003) 93 -99.

[9] J.-F. Hochedez et al. *Diamond UV detectors for future solar physics missions*. Diamond and Related Materials 10 2001 673 – 680.

[10] B.Marczewska et al. *Synthetic diamonds as active detectors of ionising radiation*. Diamond and Related Materials, 13 (2004) 918-922.

[11] B.Marczewska et al. *A study of radiation dosimeters based on synthetic HPHT diamond*. Diamond and Related Materials, 16 (2007) 191-195.

[12] Yu.Pal'yanov, I.Malinovski, Yu.Bordzov et.al. *Growing of large diamond crystals with pressless "split-sphere" apparatuses*. Reports of USSR Academy of Science, 1990, V.315, No.5, p.1221 – 1224.

[13] I.Malinovski, Ya Shurin, Yu.Pal'yanov, N.Sobolev. *Pressless "split-sphere" apparatuses (BARS) for monocrystalline diamond growing*. Proceedings of III International Conference "Crystals: growth, properties, real structure, application". Alexandrov city, 1997. V.1. p.283 – 291.

[14] Yu.Bordzov, A.Sokol, Yu.Pal'yanov, A.Hohryakov, N.Sobolev. *Growing of synthetic diamond monocrystals with mass up to 6 carat and*

perspectives of it's application. Reports of Russian Academy of Sciences 2000. V.374, No.1, p.91-93.

[15] Chrenko R.M., Tuft R.E., Strong H.M.//Nature. 1977. V.270. P.141.

[16] Evans T., Qi Z.//Proc.R.Soc.Lond.A. 1982. V.381. P.150.

[17] Klyuev Y.A., Naletov A.M., Nepsha V.I. et al. *Journal of Physical Chemistry*. 1982. V56, N3, p.524.

CHARACTERIZATION OF GaAs Cr DOPED SENSOR SAMPLES

By

Konstantin AFANACIEV¹, Alexandr IGNATENKO¹, Martin OHLERICH², Wolfgang LANGE², Wolfgang LOHMANN²

(1) National Center of Particle and High Energy Physics, Minsk, Belarus

(2) DESY, Zeuthen, Germany

GaAs is a candidate for radiation hard sensor material for the BeamCal of the International Linear Collider (ILC). Before the radiation tolerance tests the characterization of GaAs sensors doped with Sn and Cr has been performed to measure initial leakage currents as well as charge collection efficiencies. The dependence of the leakage current on temperature and on concentration of the deep acceptor (Cr) is shown. A comparison of the signal size for the sensors with different Cr concentrations is given.

Key words: LEC, SI-GaAs, charge collection efficiency (CCE)

INTRODUCTION

One of the challenging topics in the design of the ILC detector is the instrumentation of the very forward region of the detector. This region is particularly important for searches for new particles like dark matter candidates. On the other hand, the region near the beam-pipe is hit by many low energy particles resulting from the so-called beamstrahlung, a new phenomenon at high energy and high luminosity colliders. Beamstrahlung generates a large amount of electron-positron pairs scattered into detectors at small polar angles, summing up to a dose of up to 10 MGy per year of operation. Detectors in this area must be based on radiation hard sensors. Due to their high radiation hardness and large signals sensors made of GaAs are considered as an option for the very forward calorimeters at a linear collider detector. In this paper we report the results of investigation of detector parameters of such sensors.

MATERIAL

The material is produced by the Siberian Institute of Technology, Tomsk, by means of liquid encapsulated Czochralski (LEC) method. It contains two different types of dopants: Sn (shallow donor) and Cr (deep acceptor) and is semi-insulating GaAs (SI-GaAs). The processing is done in several different technological steps which results in different Cr concentrations and dopant distribution over the sensor thickness. Three batches of sensors were produced, their properties (as given by manufacturer) are listed in Table 1. Six pre-prototype sensors (two from each individual batch) have been delivered to DESY-Zeuthen. The sensors are from 151 μm to 197 μm thick and have 2-layer metallization from both sides (30nm of V and 1nm of Au). The bottom side

is glued to a metal contact, the top side is segmented into 4 5x5 mm² pads (Fig.1).

Table 1. Neutron flux obtained from different target materials

Batch #	Cr concentration, cm ⁻³	Notes
1	(1-1.5)*10 ¹⁷	non uniform over the thickness
2	(5-6) *10 ¹⁷	uniform
3	(1-3)*10 ¹⁶	uniform

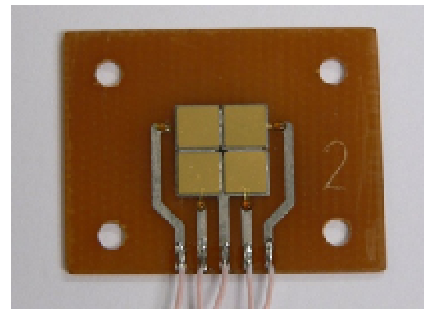


Figure 1. View to GaAs sensor

I-V CHARACTERISTICS

To measure the current-voltage characteristic, the sensor was placed into a light tight screened box. Keithley 487 was used as voltage source and as current meter. We used the following measurement procedure: set bias voltage, wait 30 seconds, measure the current within 10 seconds (one reading per second), average the readings. This average value gave one point at the plot.

Figure 2 shows the I-V characteristics (linear part) of sensors from different batches taken at a temperature of 24-25°C. The higher the Cr concentration is the lower the leakage current measured as it is clearly seen on the plot. As it was expected, the leakage currents depend on the temperature (Fig.3).

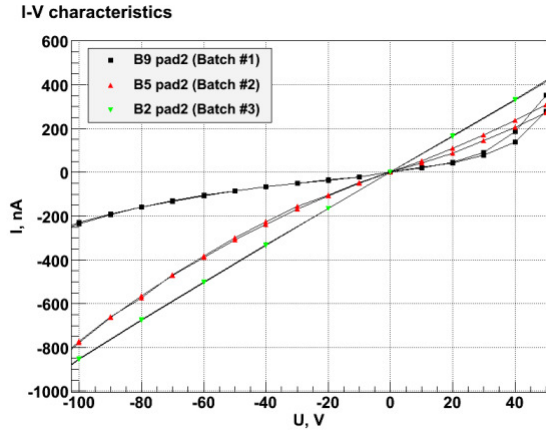


Figure 2. I-V characteristics for the sensors with different Cr concentration (linear part)

C-V MEASUREMENTS

The capacitance over voltage dependence has been measured for each pad of all the sensors. The typical C-V curve for the sensors is shown in Fig. 4. It is not constant with bias voltage. Although the change of the capacitance is within 5% such a behavior is unexpected and to be understood in future.

I-V B9 pad2

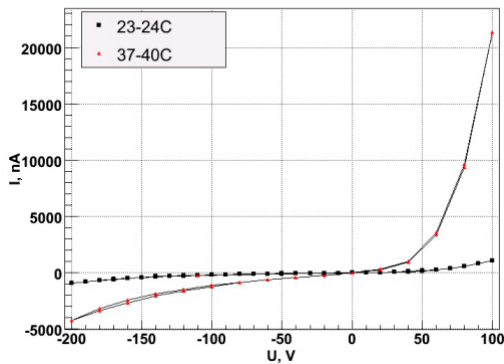


Figure 3. I-V characteristic for a sensor pad at different temperatures

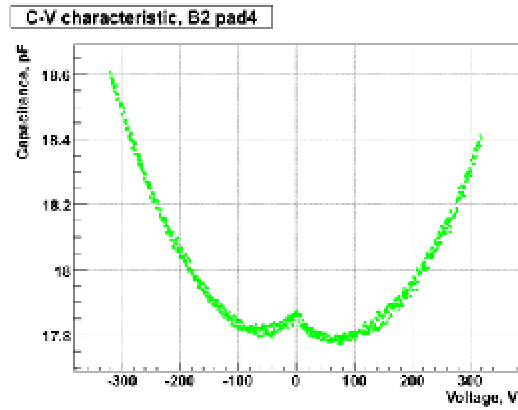


Figure 4. Typical C-V characteristic

CCE MEASUREMENTS

The charge collection efficiency (CCE) is another important characteristic of the sensor. It was measured using a setup schematically shown in Fig. 5. The sensor was operated as a solid state ionization chamber. The collimated electrons from a Sr-90 source pass through the sensor causing ionization. In the electric field provided by bias voltage (voltage source: Keithley 4687) to the electrodes of the sensor the charge carriers start to drift. Finally the signal charge is collected at the electrodes and registered with a charge sensitive preamplifier based on Amptek A250 chip. The signal is then shaped and amplified and fed into the input of charge integrating ADC. Electrons from the high energetic edge of the ⁹⁰Sr spectrum are minimal ionizing particles. They penetrate the sensor and hit the two scintillators below. Each scintillator is read-out by a photomultiplier. The coincidence of the signals from them gives a trigger for the ADC. The registered signals are digitized and stored.

An usual CCE spectrum is shown in Fig. 6. The CCE was determined with the following formula:

$$CCE = \frac{(MPV_S - Mean_p) \times k}{N_{e-h} \times d} \times 100\% \quad (1)$$

where MPV_S - most probable value of the signal peak, $Mean_p$ - mean value of pedestal, k - electronics calibration factor, N_{e-h} - average number of electron-hole pairs, created by a MIP in $1 \mu\text{m}$ of GaAs, d - sensor thickness.

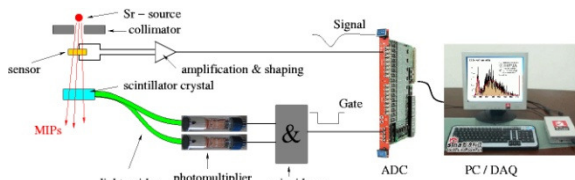


Figure 5. Schematic view of the CCE setup

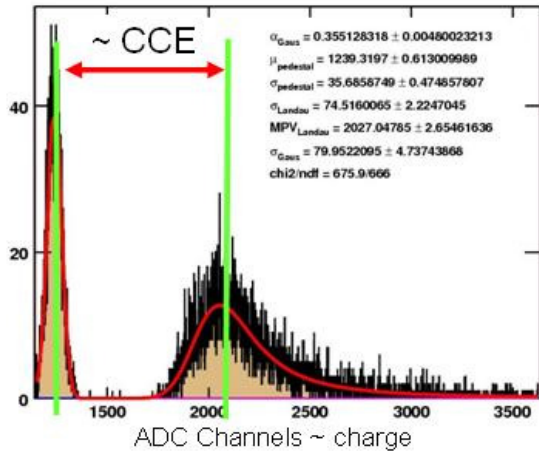


Figure 6. Spectrum of a GaAs sensor response to MIPs

The CCE as a function of the bias voltage has been measured for each pad of all the sensors. As it was expected, the higher the Cr concentration of the material the lower the CCE has been measured (Fig. 7).

The radiation tolerance of GaAs sensors doped with Cr is believed to depend on its concentration. The laboratory tests of the sensors will be followed by an exposure to high doses (of the order of a few MGy) of electromagnetic irradiation.

Two sensors made from GaAs with Cr concentration $(5-6) \cdot 10^{17} \text{ cm}^{-3}$ (which is similar to the material of the sensors from batch#2) have already been exposed up to 1.5 MGy. The results were promising: charge collection of the sensors after the irradiation was still acceptable; its degradation with the dose was similar for both sensors [6].

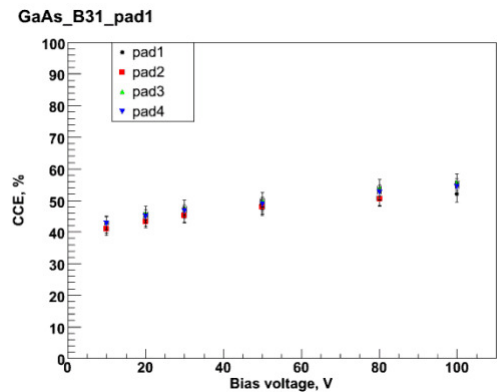
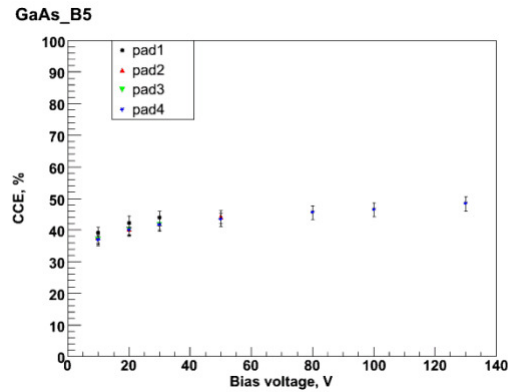
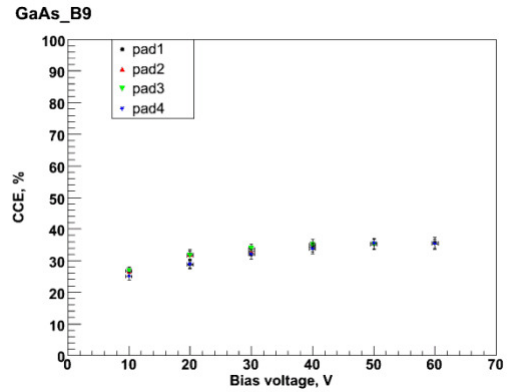


Figure 7. CCE vs bias voltage for the GaAs sensors with different Cr concentrations (batch #1 – the top plot – the highest concentration, batch #2 – the middle plot, batch #3 – the bottom plot – the lowest concentration).

REFERENCES

- [1] G. I. Ayzenshtat et al., GaAs structures for X-ray imaging detectors, Nuclear Instruments and Methods in Physics Research Section A: Accelerators, Spectrometers, Detectors and Associated Equipment, Volume 466, Issue 1, 21 June 2001, Pages 25-32
- [2] G. I. Ayzenshtat et al., GaAs resistor structures for X-ray imaging detectors, Nuclear Instruments and Methods in Physics Research Section A: Accelerators, Spectrometers, Detectors and Associated Equipment, Volume 487, Issues 1-2, 11 July 2002, Pages 96-101

- [3] G. I. Ayzenshtat et al., GaAs as a material for particle detectors, Nuclear Instruments and Methods in Physics Research Section A: Accelerators, Spectrometers, Detectors and Associated Equipment, Volume 494, Issues 1-3, 21 November 2002, Pages 120-127
- [4] A. V. Tyazhev et al., GaAs radiation imaging detectors with an active layer thickness up to 1 mm, Nuclear Instruments and Methods in Physics Research Section A: Accelerators, Spectrometers, Detectors and Associated Equipment, Volume 509, Issues 1-3, 21 August 2003, Pages 34-39
- [5] G. I. Ayzenshtat et al., GaAs detector material made from 3-inch wafers, Nuclear Instruments and Methods in Physics Research Section A: Accelerators, Spectrometers, Detectors and Associated Equipment, Volume 531, Issues 1-2, 21 September 2004, Pages 121-124
- [6] Ch. Grah et al., Radiation hard sensors for the Beam Calorimeter of the ILC, Nuclear Science Symposium Conference Record, 2007. Volume 3, Oct. 26 2007-Nov. 3 2007 Page(s):2281 – 2284

SEARCH FOR NEW BEAMCAL SENSOR MATERIALS

By

Sergej SCHUWALOW

DESY Deutsches Elektronen Synchrotron, Zeuthen, Germany

The aim of this investigation is to ascertain whether sapphire and quartz might be used as detector materials for the BeamCal of ILC. Both materials were found to show potential. When a voltage was applied the corresponding current registered an increase when the sample has been subjected to radiation. Sapphire displayed a larger increase in current than quartz. However both exhibited very low detection efficiencies, 2.1% for sapphire and 1.2% for quartz. The samples also did not appear to be uniform in their detection ability, possibly due to the large impurities within the crystals.

Key words: ILC BeamCal, Sensor, Radiation Hardness, Charge Collection

INTRODUCTION

The International Linear Collider (ILC) will require the most state-of-the-art detectors possible in order to fully exploit its potential. The Beam Calorimeter (BeamCal) of the ILC will be a compact highly segmented sandwich calorimeter adjacent to the beam pipe and will be subject to extremely high levels of radiation up to 10 MGy per year [1]. Most detectors used in calorimeters are incapable of withstanding such high levels of radiation and would either be completely destroyed or severely impaired over the period of use. For this reason radiation hard alternatives need to be investigated.

It is also preferable that these alternatives do not require additional cooling so as to keep the size of the BeamCal down. One possible option considered is CVD diamond which has already been well tested and characterized. However it is very expensive to produce and only small samples can be created with a quality high enough for use in the BeamCal. For these reasons more practical options are being investigated. Two possible options are Sapphire (Al_2O_3) and Quartz (SiO_2) which are both investigated here.

MOTIVATION OF THE MATERIAL CHOICE

Since the smallest possible Moliere radius of BeamCal media is necessary to fulfill the physics goals, the sandwich structure with dense tungsten absorber and thin solid state detector as a sensor was chosen. Requirements of high radiation resistance and small leakage current at room temperature suggest the usage of materials having a relatively large bandgap and stable lattice structure.

Fast and effective charge collection is visible only if the lattice has regular structure and the amount of impurities is minimal. All together these demands lead to the class of high purity single crystal materials having high resistivity and

hardness. Known example of such a material is artificially grown single crystal (sc) CVD diamond which has been intensively studied earlier [2]. In this paper we report about the preliminary studies of sapphire and quartz single crystal samples. Firstly it was necessary to ascertain whether or not the materials were capable of detecting charged particles at all. Then the materials were measured carefully to determine whether they were a viable alternative and how they functioned in comparison to diamond.

Three of each of the samples were provided by Crystal GmbH [3], chosen for its proximity to DESY at Zeuthen. Crystal GmbH performed a detailed impurity analysis on the crystal from which the samples were cut the results of which are detailed in Tables 3 and 5.

CHARACTERISTICS OF DIAMOND, SAPPHIRE AND QUARTZ

Diamond:

Table 1. Properties of Diamond.

Property	Value
Density	3.52 g cm^{-3}
Dielectric constant	5.7
Breakdown field	10^7 V cm^{-1}
Resistivity	$>10^{11} \Omega \text{ cm}$
Band Gap	5.5 eV
Electron mobility	$4500 (1800) \text{ cm}^2 \text{ V}^{-1} \text{ s}^{-1}$
Hole mobility	$3800 (1200) \text{ cm}^2 \text{ V}^{-1} \text{ s}^{-1}$
Energy to create e-h pair	13.1 eV
Average signal created	$36 \text{ e } \mu\text{m}^{-1}$

The single crystal diamond sensor used in this study as a reference detector, was created using Chemical Vapor Deposition process. The sample

obtained from Element-6 company [4] has a size of $5 \times 5 \times 0.32 \text{ mm}^3$ and round metalization of 3 mm diameter on both sides. Properties of diamond are listed in the Table 1, where the mobilities of free charge carriers shown in parentheses refer to the polycrystalline form.

Sapphire:

The sapphire crystal was created using the Czochralski process. A seed crystal on a rod is placed just above a crucible containing a molten sample of the material. The phase front between the liquid and the crystal is held just above the level of the molten material. The rod containing the crystal is then slowly lifted and rotated to create one long crystal by drawing up more of the melt as the crystal cools. The process is carried out within an inert atmosphere to prevent impurities. As the process must be carried out at 2325 K in order to melt the Al_2O_3 there are frequently high levels of impurities due to the crucible walls melting.

Table 2. Properties of Sapphire.

Property	Value
Density	3.98 g cm^{-3}
Dielectric constant	9.3 - 11.5
Breakdown field	$\sim 10^6 \text{ V cm}^{-1}$
Resistivity	$> 10^{14} \Omega \text{ cm}$
Band Gap	9.9 eV
Electron/hole mobility	UNKNOWN
Energy to create e-h pair	$\sim 29 \text{ eV}$
Average signal created	$22 \text{ e } \mu\text{m}^{-1}$

Table 3. Impurities of Sapphire.

Imp	Na	Si	Fe	Ca	Mg	Ni	Ti	Mn	Cu	Zr	Y
ppm	8	2	5	5	1	<3	<1	3	<3	2	2

Quartz:

The quartz was produced through hydrothermal synthesis [5] in a pressurized steel autoclave, separated into two halves by a metal plate. In the bottom half a supply of quartz is placed and the autoclave is then filled to a specific amount with either an alkali metal hydroxide or carbonate in aqueous solution in order to increase the solubility of quartz by forming soluble silica complexes. The temperature and pressure are then manipulated, causing the quartz to dissolve. The warm solution rises up into the cooler top chamber resulting in the supersaturation of the solution

which then precipitates onto the seed crystal.

Table 4. Properties of Quartz.

Property	Value
Density	2.6 g cm^{-3}
Dielectric constant	4.3
Breakdown field	$\sim 10^6 \text{ V cm}^{-1}$
Resistivity	$> 10^{12} \Omega \text{ cm}$
Band Gap	8.4 eV
Electron/hole mobility	UNKNOWN
Energy to create e-h pair	$\sim 18 \text{ eV}$
Average signal created	$22 \text{ e } \mu\text{m}^{-1}$

Table 5. Impurities of Quartz.

Impurity	Na^+	Li^+	Al^{+3}	Fe^{+3}	OH
ppm	<10	<3	<30	<10	<100

MEASUREMENTS

The samples provided were all 10 mm square and $500 \mu\text{m}$ thick. Onto each sample four 4 mm square pads were bonded to one side, and one large 8 mm square pad on the reverse. Each of the three samples of each material utilized a different metalization (a combination of Al, Ti and Au layers). These detectors were then placed into holders with metal contacts connected to the pad by a wire ultrasonically soldered onto both as shown in Fig 1.

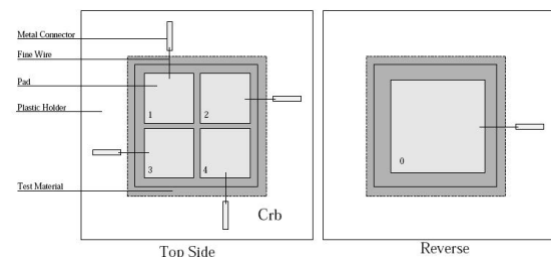


Figure 1. Structure of samples under test.

The first measurement necessary was to ascertain whether or not the samples were usable as detectors. The samples were fastened into a metal shielding box with aluminum foil windows. The detectors were connected to a Keithley 487 picoammeter/voltage source, capable of measuring current down to a level of 1 pA. The box was then flushed with nitrogen to prevent surface currents. The set up can be seen in Fig 2.

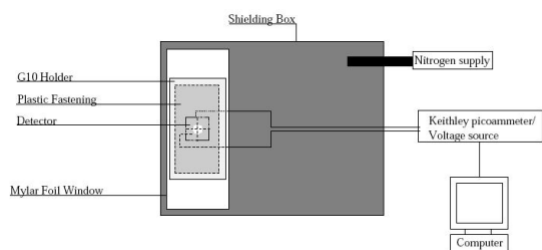


Figure 2: Set up for the measurement of current and voltage for the various detectors.

A voltage was then applied across the material up to a maximum of 500V in steps of 50V, then down to -500V and back up to 0V, recording the current. At each voltage a period of time was allowed for the current to settle. This was adjustable but usually set to 40s. Each set of readings was taken three times to ensure that the readings were repeatable and consistent. This was then repeated with a ^{90}Sr source placed above the sample at a consistent height.

This process was also done for a diamond sample in order to perform a comparison.

RESULTS AND ANALYSIS

Without the source the samples were found to be repeatable with only a variance of a few percent between successive readings. There was a great deal of variance between different samples and even between different pads on the same sample with the current at 500 V ranging from 1 pA to 10 pA. This appeared to have no relation to the material or to the condition of the pad. However, as even the largest readings without the source were no more than 10% of the current of those taken with it this was deemed acceptable within the scope of this investigation. There was a variance of those readings taken with a source of between 30 pA to 110 pA between samples and pads but again each individual pad was repeatable to within a few percent. It would appear that SiO_2 yields a current 50-80% that of Al_2O_3 . It was observed however that SiO_2 required a shorter settling time than that of Al_2O_3 . The mean values of every reading across every pad per detector is shown in Fig 3.

The diamond sensor was used as a baseline with which to compare the two test materials to. The diamond sensor was assumed to be a perfect sensor and so detects all particles that crosses it. The current was used to estimate the equivalent number of MIPs (Minimum Ionizing Particles) that crossed it and so also crossed the test materials per second. Knowing that the mean value for the current for diamond at 500 V is 1.56 nA ($1.56 \times 10^{-9} \text{C s}^{-1}$) and that this current corresponds to the creation of 9.8×10^9 electron-hole pairs per second being generated in the crystal, one can estimate the flux of MIPs to be

$$\Phi = 1.2 \times 10^5 \text{ MIPs s}^{-1} \text{ mm}^{-2}$$

Using this flux, geometry of the detector and properties of crystals listed in the Tables 2 and 4, one can calculate the expected current for the particular sample and thus the charge collection efficiency when compared to the measured one.

This produces an average efficiency for the two materials of 1.2% for SiO_2 and 2.1% for Al_2O_3 . It should be noted that this is only a rough estimate, not taking into account a realistic ^{90}Sr electron spectrum.

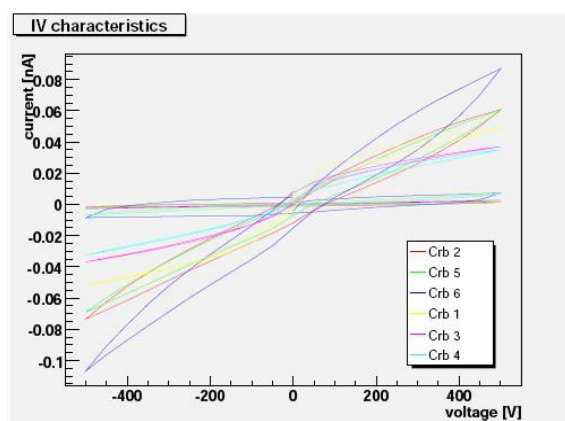


Figure 3: The average current vs voltage plots for all six samples both with and without the source. Crb2,5,6 – sapphire samples, Crb1,3,4 – quartz. All measurements without the source show the current below 10 pA.

CONCLUSIONS

The current from the samples measured without ^{90}Sr source was found to be between 2-10% of that with the source showing that the materials are capable of detecting radiation and are worth further study.

Each individual measurement was repeatable to a level of 1-2%, though the variance of 5-8% was observed across the samples between pads. There is also a large difference in the maximum observed current for each sample of the same material.

The mean charge collection efficiency of the tested detectors is 1.2% for SiO_2 and 2.1% for Al_2O_3 samples which is not yet sufficient for the usage as BeamCal sensors.

Both nonuniformity of the response and low charge collection efficiency point out to the insufficient purity of the crystals investigated.

FUTURE WORK

The next step is to irradiate the samples to see if SiO_2 or Al_2O_3 have a high enough radiation hardness to withstand the extreme conditions of the BeamCal. If they prove so then it would be then necessary to increase the efficiency of the detectors before they became a viable alternative. If a purer

sample can be found then this may provide a solution.

REFERENCES

- [1] The Forward Calorimetry Collaboration (FCAL).
Report for the ILC Detector R&D Panel Instrumentation
of the Very Forward Region. ILC Detector R & D Panel
Report, May 20, 2007.
- [2] Radiation Hard Sensors for the BeamCal of the ILC
C. Grah for the FCAL Collaboration, IEEE-2007
- [3] Crystal GmbH
Ostendstasse 25, Haus 4, D-12459 Berlin.
- [4] Element 6 Ltd. Isle of Man Freeport, PO Box 6,
Ballasalla, Isle of Man, IM996AQ, British Isles
- [5] 'Hydrothermal Synthesis of Crystals'
R.A. Laudise Chemical And Engineering News, Vol.65
(39), 30, 1987

BEAMCAL MECHANICS

By

Sergej SCHUWALOW

DESY Deutsches Elektronen Synchrotron, Zeuthen, Germany

This document gives an overview of the BeamCal mechanical design for the ILD concept. In addition BeamCal support structure and installation procedure issues are addressed.

Key words: ILC BeamCal, Mechanics, Support, Installation.

INTRODUCTION

The Beam Calorimeter (BeamCal) was shown to be an important subdetector to identify two photon events when an electron or positron has an energy near to the beam energy and a small production angle. Such events constitute the largest background for many SUSY search channels at ILC with the signature of missing energy/momentum. The rejection of such events with high efficiency is needed down to about 5 mrad of polar angle where a significant flux of beamstrahlung pairs is expected.

In addition the BeamCal could be used for the fast beam diagnostic purposes, if it will be able to provide immediate bunch-to-bunch information about the beamstrahlung pairs energy and spatial distributions.

OVERALL DESIGN REQUIREMENTS

Following the preliminary design of the ILD detector, the BeamCal will be positioned at a distance of approximately 3.3m from the interaction point. It should fit into the 6-m length support tube which includes some final focus elements of the machine and carries the weight of the low-angle detector components like LumiCal and LHCal.

The construction of BeamCal strongly depends on the beam crossing angle scheme. For large crossing angles ($14\text{-}20 \text{ mrad}$) 2 separate beam pipes for the incoming and for the outgoing beams are foreseen at the BeamCal location.

As it was shown by simulations, BeamCal itself should be preferably centered around the outgoing beampipe and thus be displaced from the ILD detector axis. In this paper we will present the possible mechanical design of BeamCal for the large crossing angle scenario. The main parameters of the calorimeter taken from the present simulation studies are as follows:

- BeamCal is a sampling calorimeter $30 X_0$ depth.
- Tungsten absorber is used to minimize Moliere radius.

- The shower is sampled every X_0 (3.5mm absorber plate thickness).
- The sensor plane thickness should not exceed 0.5mm to keep the Moliere radius small.
- The outer sensitive BeamCal radius is 150 mm.
- The incoming beam cutout radius is 15 mm.
- The outgoing beam cutout radius is 20 mm.
- The total length of the BeamCal is about 15 cm, weight is about 160 kg.

It should be specially emphasized that at the moment there is no good solution for the BeamCal sensors found. The challenge is extremely severe radiation conditions at the innermost calorimeter region where annual doses up to 10 MGy are expected. So the final design of the sensor plane will depend on the results of ongoing R&D studies and therefore details of it will not be considered in this paper.

The assumption is that the sensor plane will consist out of 8 sectors each covering 45° of azimuthal angle. Each (out of two) BeamCal will consist of two parts - upper and lower halves in order to allow its installation and disassembly without cutting the beampipes. In turn it requires the possibility to open the support tube or some special installation cutout should be foreseen (see Fig 1).

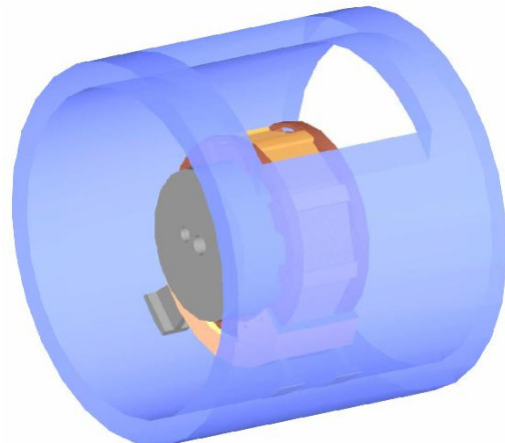


Fig 1. BeamCal inside the support tube. An installation cutout in the support tube will be needed.

HALF-LAYER MECHANICS

Each half-layer will be made out of two parts - the tungsten plate of 3mm thickness and the frame part (total thickness - 4mm) made of brass. In total each BeamCal requires 60 pieces of each type. Parts of the half-layer are glued together at the precise flat surface, for one of the BeamCal halves the tungsten plate is turned upside-down to provide a mirror symmetry (see Fig.2).

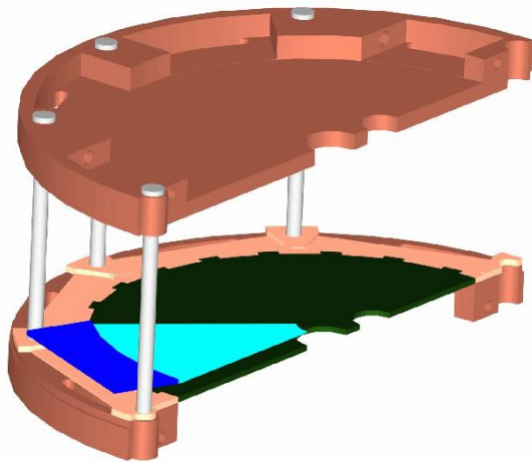


Fig.2 Mechanical structure of the BeamCal half. Hybrid sensor sector (sensor+R/O electronics) is shown in cyan/blue colors. The stack of layers together with front/back support frames are kept together with rods.

Four pits in the frame serve for the readout electronics housing. Two more frames of half-ring shape are added - the first one at the front and the second one at the end of BeamCal. They are needed for installation of the assembled calorimeter onto the support structure, to join together the halves of BeamCal, to provide the crane hooks fixing and to house extra electronics (at the backside frame) for collecting together the signals from all layers and transmitting the resulting information to the DAQ and FONT systems.

Assembled stack will be kept together by means of rods, shown in the Fig 3 in gray. In case if extra cooling of the BeamCal will be needed, these rods could be made hollow and used as water pipes.

The outermost rings of the frames after calorimeter assembly finally will form a cylinder of 200~mm radius.

SENSOR AND HYBRID CONSTRUCTION

As it was already mentioned above, the real sensor design will strongly depend upon the results of ongoing R&D, so here we discuss only some possible features of it. Each sensor sector covers a quarter of the half-layer and consists of the sensor itself (subdivided into the necessary number of

pads) and a Readout Electronics PCB at the peripheral part of the sector. The parts are connected together via a thin foil-like PCB carrying all connecting traces, forming the common piece that could be called R/O Hybrid. Connectors for Hybrid powering and data transmission will be placed at the outermost edge and after assembly necessary connections will be made by flat cables.

For the precise positioning of the Hybrids some lugs at the frame should be foreseen.

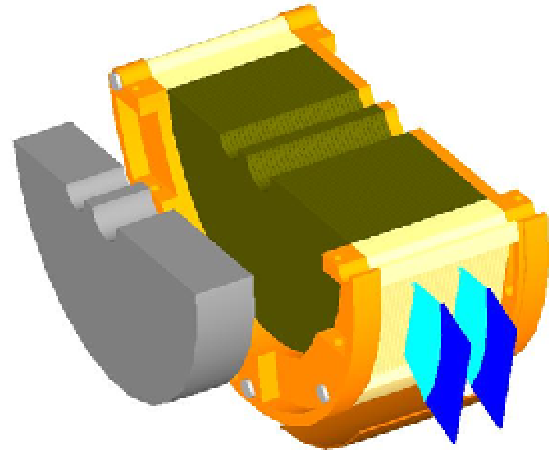


Fig 3. BeamCal half assembled. Graphite absorber in front of BeamCal is shown in gray.

SUPPORT STRUCTURE & INSTALLATION

The proposed support structure could be seen in the Fig 4. It consists of the static frame which is fixed to the support tube and two sets of rolls carrying the BeamCal itself.

The rolls have a lug that together with a facet at the edge BeamCal frames prevents it from the longitudinal movement. With such a support BeamCal could be easily rotated around its axis, the final position is fixed using the screws.

The BeamCal installation scenario is based on the assumption that both beampipes will be already in place and the BeamCal itself could be installed or dismantled without touching them. For that some dummy half of the BeamCal should be placed onto the support before beampipes installation. This dummy half should have the same torque as the real BeamCal half, but with some larger inner cutout that allows its free rotation around both beam pipes (see Fig 4) After beampipes installation the dummy part is fixed at some angle that allows for bottom BeamCal part installation on top of it (in upside-down position). After screwing parts together (Fig 5) the fixture of dummy part is released and the assembly is rotated clockwise until the bottom BeamCal will turn out at the correct position (see Fig 6). Now this part is screwed to the support and the dummy part is replaced by the upper BeamCal half. At the end two parts will be fixed together.

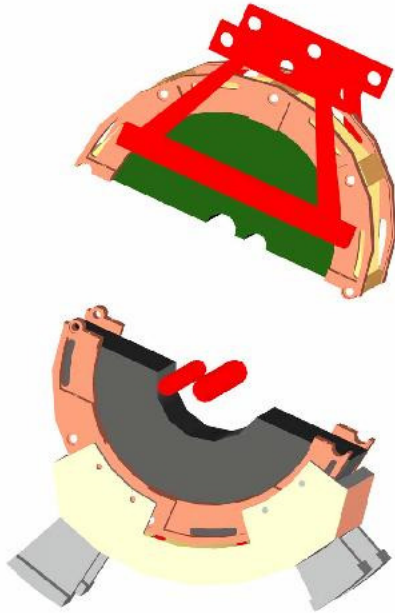


Fig 4. BeamCal installation scheme. Phase 1: *Dummy half is on the support, bottom part of the BeamCal is mounted on top of it.*



Fig 5. BeamCal installation scheme. Phase 2: *Parts are fixed together and rotated clockwise.*

INTEGRATION ISSUES

There are several issues that should be taken into account:

- (1) In order not to spoil the BeamCal performance, the amount of the material between the IP and calorimeter should be kept as small as possible. No pumps should be installed in front of the BeamCal.
- (2) Presently the possibility of Beam Pair Monitor installation right in front of BeamCal is discussed. The mechanical support design for it as well as installation procedure should be developed.
- (3) The amount of cables and optical transmission lines needed for BeamCal and Beam

Pair Monitor should be defined and communicated with MDI group.

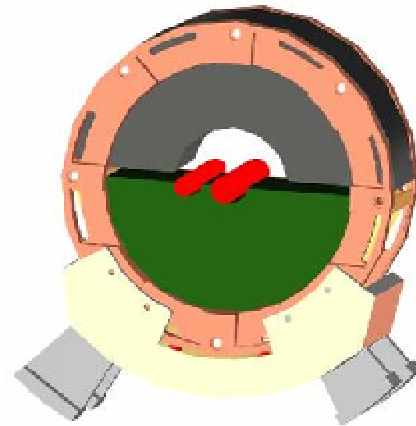


Fig 6. BeamCal installation scheme. Phase 3: *Now the dummy half could be replaced by the upper part of BeamCal. To complete installation, parts are screwed together and BeamCal cabling is performed.*

SUMMARY

In this paper we had presented a preliminary mechanical design of the BeamCal. Main geometrical parameters are chosen as follows:

- The thickness of the BeamCal itself is 15cm. In addition some space for low-Z mask (graphite) and Beam Pair Monitor installation should be foreseen in front of BeamCal.
- Additional space (about 10 cm in Z-direction) for the service purposes should be foreseen before and after the BeamCal.
- The Outer instrumented BeamCal radius is 150 mm.
- The full outer BeamCal radius is 200 mm.
- The total BeamCal weight is about 160 kg.
- The BeamCal consists of two halves (top and bottom).
- The upper part of the support tube (at least 35 cm above the BeamCal) should be open or made removable for the installation purposes.
- The crane operation will be needed for the installation.

DEVELOPMENT OF PAIR MONITOR

By

Yosuke TAKUBO

Department of Physics, Tohoku university, Sendai, Japan

The pair monitor is a beam profile monitor at interaction point (IP) for the international linear collider (ILC). We design and develop the pair monitor as a silicon pixel sensor which is located at about 400 cm from IP. As the first step to develop the pair monitor, the readout ASIC was developed. Although there was a problem in the MIM capacitor, response of all the circuit components was confirmed. In this paper, test results of the readout ASIC and the future plan are reported.

Key words: pair monitor, ILC, readout ASIC, beam profile monitor, CMOS, SOI

INTRODUCTION

The pair monitor is used to check the beam profile at the interaction point (IP), measuring the distribution of the e^+e^- pairs generated during the beam crossing [1]. The particles of concern have the same charge as that of the oncoming beam, and are hereafter called “same-charge” particles. Most of them are deflected at larger angles than their inherent scattering angles by a strong electromagnetic force due to the oncoming beam, while the “opposite-charge” particles must oscillate inside the oncoming beam because of a focusing force between them; they are deflected with small angles. They can be well described by a scattering process of $e^-(e^+)$ in a two-dimensional Coulomb potential that is Lorentz boosted to the rest frame of the oncoming beam. Since this potential is produced by the intense electric charge of the oncoming beam, it is a function of the transverse size (σ_x, σ_y) and intensity of the beam. Therefore, the deflected particles should carry this information, especially in their angular distribution. The pair monitor uses this principle to extract information of the beam profile at IP. In our previous studies, the pair monitor has performance to measure the beam size with $\sim 10\%$ accuracy [2].

We have studied design of the pair monitor and developed the prototype of the readout ASIC. In this paper, development status of the pair monitor is reported. At first the design concept of the pair monitor as the ILC beam profile monitor is described. Then, development of the readout ASIC and results of its response test will be described. Finally, a plan to develop the pair monitor with SOI technology will be shown.

DESIGN CONCEPT OF PAIR MONITOR

There are some requirements to the pair monitor to be used for the beam profile monitor at ILC. The pair monitor is required to measure the

beam profile at the interaction point, and the measurement results must be feedback to the next train to keep the high luminosity. Therefore, the pair monitor must measure the hit distributions for train by train, and the data should be readout within the inter-train time (~ 200 ms). Since the pair monitor will be put at about 400 cm from IP and close to the beam pipe, the radiation dose on the pair monitor becomes large. For example, the radiation dose was estimated as ~ 10 Mrad/year at the radius of 10 cm from the extraction beam pipe in the GLD geometry [3]. Although the radiation dose decreases rapidly for the larger radius, the radiation tolerance must be above 1 Mrad/year.

To achieve these requirements, the design concept of the pair monitor was considered. The sensor is assumed as a silicon pixel sensor whose pixel size is $400 \times 400 \mu\text{m}^2$ and thickness is $200 \sim 300 \mu\text{m}$. The size of the sensor layer is 10 cm radius. In the sensor layer, two holes for the injection and extraction beam pipes will be prepared, whose radius is 1.0 cm and 1.8 cm, respectively. The total readout channel will be about 200,000. The readout ASIC will be bump-bonded to the sensor, and measures the hit counts on the detector to obtain the hit distributions of the pair backgrounds. At that time, it is not necessary to obtain the information of the energy deposit. Based on this design concept, development of the pair monitor was started.

DEVELOPMENT OF READOUT ASIC

We have developed the readout ASIC for the pair monitor. It is designed to count a number of the hit to obtain the hit distribution on the detector. The statistics for about 150 bunches is enough to extract the beam information on the detector. Therefore, the number of the hit is counted for 16 timing parts in one train, which corresponds to $167 (= 2670/16)$ bunches in the current nominal ILC design. The hit counts for each timing parts are read within the

inter-train time (200 ms). A silicon pixel sensor with the thickness of about 200 μm is assumed as a detector candidate, whose signal level is about 15,000 electrons. The readout ASIC is designed to satisfy these requirements.

The readout ASIC consists of the distributor of the operation signals, shift register to specify a readout cell, data transfer to the output line, and 36 readout cells. A readout cell consists of the amplifier, comparator, 8-bit counter, and 16 count registers as shown in Fig. 1. They are aligned to 6 x 6 for the X and Y directions.

The prototype ASIC was produced with 0.25 μm TSMC process as shown in Fig. 2. Its layout was made by Digian Technology, Inc. [4], and the production was done by the MOSIS Service [5]. The chip size is 4 x 4 mm^2 , and the readout cell size is 400 x 400 μm^2 . In the readout cells, bonding pads are prepared to attach the sensors by bump-bonding. For the response test of the readout ASIC, the chip is covered with a PGA144 package.

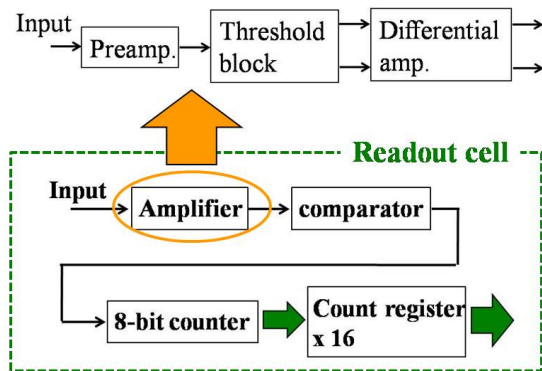


Fig. 1: A schematic logic in the readout cell which consists of the amplifier, comparator, 8-bit counter, and 16 count registers. In the amplifier blocks, there are a pre-amplifier, threshold block, and differential amplifier.

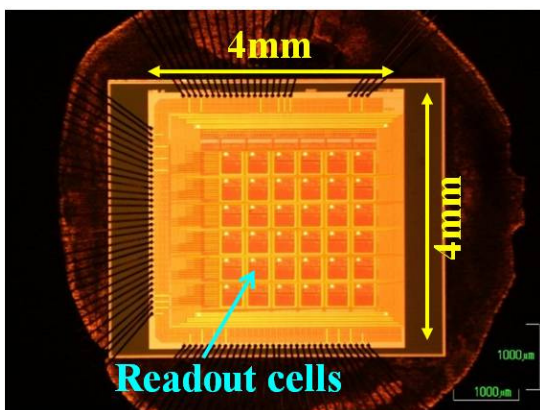


Fig. 2: A picture of the readout ASIC

RESPONSE TEST OF THE PROTOTYPE ASIC

For the response test of the readout ASIC, the test system was constructed, based on the VME system. A VME-GPIO module was used for the

operation and data readout, which was developed as the KEK-VME 6U module. The readout ASIC is attached on the test-board, and connected to the VME-GPIO module. Since a FPGA is equipped on the GPIO module, any logic can be realized by changing the program implemented into a FPGA. To readout all the hit counts from 16 count registers in each pixel (36 pixels), we prepared a FIFO in the FPGA. All the hit counts are stored in it, then, they are sent to a computer.

At first, the response of the amplifier block was checked. The amplifier block consists of the pre-amplifier, threshold block, and differential amplifier as shown in Fig. 1. Fig. 3 shows an output signal from the pre-amplifier. Inputting the test-pulse to the sensor input, output signals were observed from the pre-amplifier as expected by the SPICE simulation. Therefore, it was confirmed that the pre-amplifier works correctly.

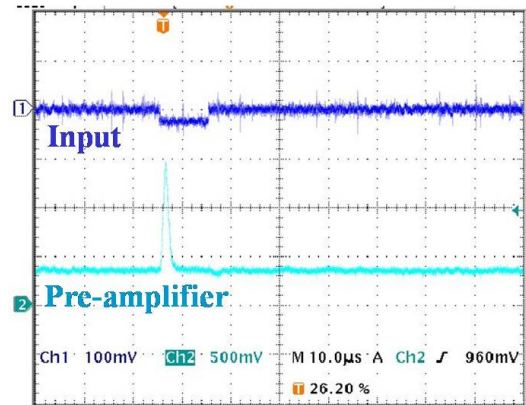


Fig. 3: An output signal from the pre-amplifier, which was observed at the timing of the test-pulse.

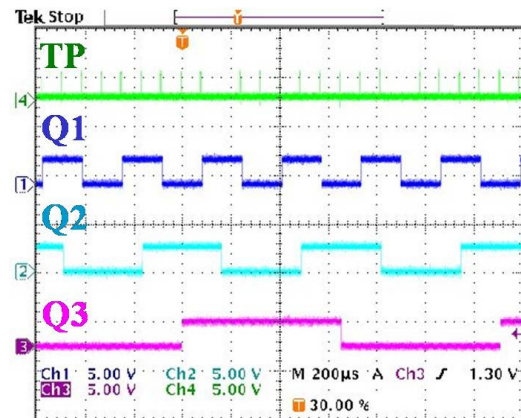


Fig. 4: Output signals from the counter block. TP shows the test-pulse, and Q1, Q2, and Q3 show the counter bit. The hit count is output with Gray code.

Then, we investigated response of the differential amplifier, which can be checked by using two input lines of the test-pulse. One is prepared at the threshold block. The other is a sensor input which was used to check the pre-amplifier. The output signal was observed from the differential amplifier, by using the test-pulse input

at the threshold block. Therefore, the differential amplifier seems to work correctly. However, the signal was not output by using the sensor input. From this result, there was some problem between the pre-amplifier and threshold block.

Since the test-pulse input at the threshold block can be used, the response test was continued. For the next step, a function of the counter block was checked. Fig. 4 shows the output signals from the counter block, which was designed to use Gray code. Since a number of the hits was output correctly, the hit count was read from the count registers by a computer. Fig. 5 shows the relation between a number of the input pulse and that of the hit counts read from one of the count registers, which was obtained with about 10 kHz operation. It was confirmed that there is no bit lost in the data. From these test results, we can conclude that all the circuit block works correctly without the snapping between the pre-amplifier and threshold block.

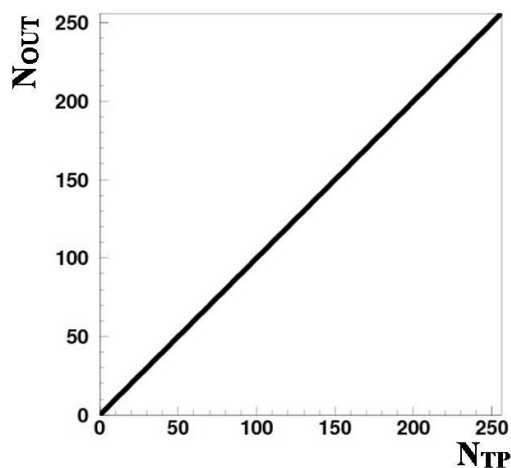


Fig. 5: The relation between a number of the input pulse (N_{TP}) and that of the hit counts read from one of the count registers (N_{OUT}), which was obtained with about 10 kHz operation. No bit lost was observed in the data.

We investigated the reason of the snapping between the pre-amplifier and threshold block. Checking the ASIC layout, we found that the MIM (Metal Insulator Metal) capacitor was not prepared in the layout mask, which was used at the threshold block. Since the circuit was insulated at the MIM capacitor, the signal from the pre-amplifier did not reach the differential amplifier. We modified the ASIC layout and ordered the production of the readout ASIC to the company. The new ASIC was delivered in Oct., 2008. It works correctly without any problem.

PAIR MONITOR WITH SOI TECHNOLOGY

For the next step, we plan to develop the pair monitor with SOI (Silicon On Insulator) technology. The SOI technology is the technique to

electrically separate the transistors from Si layer. It realizes to prepare the sensor and readout ASIC on the same wafer without bump-bonding. Since we already developed the readout ASIC with usual CMOS technology, its design can be used for the readout circuit. In addition, the devices are fabricated using a very thin (40 nm) silicon layer, therefore, high-radiation tolerance is expected. This project was already started as collaboration with KEK and Tohoku university. The first prototype will be developed in 2009.

CONCLUSIONS

We developed the pair monitor for the beam profile monitor at ILC. The readout ASIC was developed in 2006. Although the MIM capacitor in the threshold block was not prepared in the layout design, we confirmed that all the circuit block works correctly. We modified the ASIC layout to implement the MIM capacitor, and the new ASIC was delivered. It works correctly without any problem. For the next step, we plan to develop the pair monitor with SOI technology. The first prototype will be developed in 2009.

ACKNOWLEDGEMENT

This study is supported in part by the Creative Scientific Research Grant No. 18GS0202 of the Japan Society for Promotion of Science.

REFERENCES

- [1] T. Tauchi and K. Yokoya, Phys. Rev. E 51, 6119, 1995.
- [2] Y. Takubo, Proceedings of LCWS 2007, http://www-zeuthen.desy.de/ILC/lcws07/pdf/MDI/takubo_yosuke.pdf
- [3] GLD Detector Outline Document, arXiv:physics/0607154.
- [4] <http://www.digian.co.jp> in Japanese.
- [5] <http://www.mosis.com>.

PERFORMANCE STUDY OF PAIR MONITOR

By

Kazutoshi ITO¹

(2) Department of Physics, Tohoku University, Sendai, Japan

(3)

The pair monitor is the beam profile monitor at interaction point for the International Linear Collider (ILC). Simulation study was done to estimate the performance of the pair monitor. In this paper, the method of the reconstruction and the expected errors on the beam size are reported. The measurement accuracy of 2% and 3% was obtained for the horizontal beam size (σ_x) and the vertical beam size (σ_y), respectively, using the Taylor expansion up to the second order.

Key words: ILC, diagnostics, beam profile, pair monitor, simulation

INTRODUCTION

In the ILC, measurement of the beam size is important to keep the high luminosity because the luminosity critically depends on beam sizes as [2]:

$$\mathcal{L} = \frac{1}{4\pi} \frac{f_{rep} n_b N^2}{\sigma_x \sigma_y} \times H_D, \quad (1)$$

where

- f_{rep} : pulse rate,
- n_b : the number of bunches per pulse,
- N : the number of particles per bunch,
- σ_x (σ_y): the horizontal (vertical) beam size,
- H_D : the disruption enhancement factor (typically $H_D \approx 2$).

The beam size at the interaction point (IP) is 639 nm (width) \times 5.7 nm (height) \times 300 μ m (length) to achieve a luminosity of $2 \times 10^{34} \text{ cm}^{-2} \text{ s}^{-1}$. In particular, the height must be monitored with 1 nm accuracy ($\sim 10\%$ accuracy). Although some candidates of the beam profile monitor already exist, none of them achieves measurement accuracy with 10% level at IP except for the pair monitor [3].

Since the beam energy and density of the particles in the bunches are very high, a large number of e^+e^- pairs are created during crossing of the beam bunches by the three incoherent processes; the Breit-Wheeler process ($\gamma\gamma \rightarrow e^-e^+$), the Bethe-Heitler process ($\gamma+e \rightarrow e+e^-e^+$) and the Landau-Lifshitz process ($e+e \rightarrow e+e^-e^+$), where γ is a beamstrahlung photon [2]. The generated e^\pm pairs are called pair backgrounds. The particles which have the same charge with respect to the oncoming beam are scattered with large angle due to the electromagnetic field generated by the beam bunches (Figure 1). The scattered particles have beam information at IP because the field strength depends on the beam shape [3,5].

The pair monitor measures the beam profile by using the azimuthal distributions of the scattered e^+e^- pairs. In our previous study, the pair monitor

was confirmed to have acceptable performance as a beam profile monitor for ILC [8].

In this paper, we report a reconstruction of the beam size using the Taylor matrixes and the expected errors.

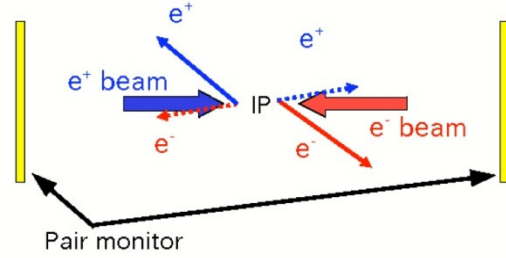


Figure 1. Pair backgrounds are created during crossing of the beam bunch by the incoherent processes. The same charges with respect to the oncoming beam are scattered with large angle. The pair monitor measures the beam profile at IP using distribution of the pair backgrounds.

SIMULATION SETUP

In this study, CAIN [4] and Jupiter [9] were used for pair background generator and tracking emulator, respectively. The pair monitor was located at 400 cm from IP (Figure 2).

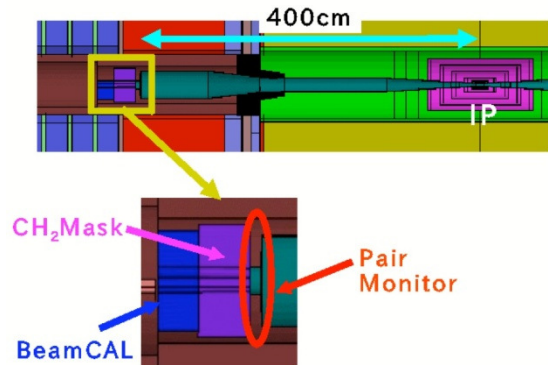


Figure 2. The detector geometry and location of the pair monitor.

Solenoid filed (3T) with anti-DID [1] was used for the magnetic field. The nominal beam parameters for ILC are given in Table 1 [1]. The shape of the pair monitor is a disk, which has 10 cm radius. There are two holes which radius is 1.8 cm and 1.0 cm for the extraction and injection beam pipe, respectively.

Table 1. The nominal beam parameters at ILC.

Parameter	Unit	
Center of mass energy	GeV	500
Number of particle per bunch	$\times 10^{10}$	2.05
Number of bunches per pulse		2625
Pulse rate	Hz	5
Horizontal beam size at IP	nm	639
Vertical beam size at IP	nm	5.7
Longitudinal beam size at IP	μm	300
Crossing angle	mrad	14

THE RECONSTRUCTION METHOD OF THE BEAM SIZE

We measure the beam size by using the measurement variables derived from the hit distribution of the pair backgrounds (for example, the total number of the hits, etc.). Since the measurement variables (m_i , $i = 1, 2, \dots, n$) should depend on the horizontal and vertical beam size (σ_x , σ_y), they can be expanded around the nominal beam size σ_x^0 , σ_y^0 by the Taylor expansion as follows.

$$\begin{aligned}
m_i(\sigma_x, \sigma_y) - m_i(\sigma_x^0, \sigma_y^0) &= \frac{\partial m_i}{\partial \sigma_x} (\sigma_x - \sigma_x^0) + \frac{\partial m_i}{\partial \sigma_y} (\sigma_y - \sigma_y^0) \\
&\quad + \frac{1}{2} \frac{\partial^2 m_i}{\partial \sigma_x^2} (\sigma_x - \sigma_x^0)^2 \\
&\quad + \frac{\partial^2 m_i}{\partial \sigma_x \partial \sigma_y} (\sigma_x - \sigma_x^0)(\sigma_y - \sigma_y^0) \\
&\quad + \frac{1}{2} \frac{\partial^2 m_i}{\partial \sigma_y^2} (\sigma_y - \sigma_y^0)^2 + \dots \\
\Delta m_i &= \frac{\partial m_i}{\partial \sigma_\alpha} \Delta \sigma_\alpha + \frac{1}{2} \Delta \sigma_\beta \frac{\partial^2 m_i}{\partial \sigma_\alpha \partial \sigma_\beta} \Delta \sigma_\alpha + \dots \\
&= \left[\frac{\partial m_i}{\partial \sigma_\alpha} + \frac{1}{2} \Delta \sigma_\beta \frac{\partial^2 m_i}{\partial \sigma_\alpha \partial \sigma_\beta} + \dots \right] \cdot \Delta \sigma_\alpha, \quad (2)
\end{aligned}$$

expressed using vectors and matrices as

$$\Delta \mathbf{m} = [A_1 + \mathbf{x}^T \cdot A_2 + \dots] \cdot \mathbf{x}, \quad (3)$$

where $\Delta \mathbf{m} = (\Delta m_1, \Delta m_2, \dots, \Delta m_n)$, $\mathbf{x} = (\Delta \sigma_x, \Delta \sigma_y)$ and A_1 is the $n \times 2$ matrix of the first order term of Taylor expansion and A_2 is a tensor of the second derivative term. The beam size is reconstructed by multiplying the inverted matrix of coefficient of \mathbf{x} in Equation (3) as follows.

$$\mathbf{x} = (A_1 + \mathbf{x}^T \cdot A_2 + \dots)^+ \cdot \Delta \mathbf{m}, \quad (4)$$

where the superscript “+” indicates the Moore Penrose inversion which gives the inverse matrix of a non-square matrix A as $A^+ = (A^T A)^{-1} A^T$ [6,7].

THE MEASUREMENT VARIABLES

We searched for optimal measurement variables that depend on the beam size. First, we

focused on the radial hit distribution on the pair monitor. The scattered angle of the pair backgrounds depends on the strength of the electromagnetic field around the beam bunch, i.e., the particle density in the beam bunch. Therefore, the size of the radial hit distribution is inversely proportional to the horizontal beam size. Since the vertical beam size is much smaller than the horizontal beam size, it would be independent of the vertical beam size [3]. To evaluate the size of the radial hit distribution, the maximum radius (R_{\max}) is defined as radius to contain 99.8% of all the hits. Figure 3 shows R_{\max} versus the horizontal beam size. As expected, this plot shows that R_{\max} decreases for larger horizontal beam size independent of the vertical beam size.

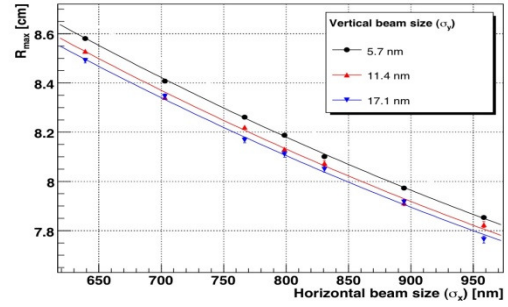


Figure 3: R_{\max} vs. σ_x , where R_{\max} is defined as the radius to contain 99.8% of all hits. R_{\max} decreases for larger σ_x independent of σ_y .

The azimuthal distribution of the hit density on the pair monitor would change according to the transverse aspect ratio of the bunch. We studied the distribution of the hit density as a function of the radius from the extraction beam pipe (R) and the angle around it (ϕ) as shown in Figure 4. To derive the beam information, we compared the number of hits in $-\pi < \phi < 1.2$ and $2.7 < \phi < \pi$ for $0.5R_{\max} < R < 0.8R_{\max}$ (N_0) and the total number of hits (N_{all}) [8].

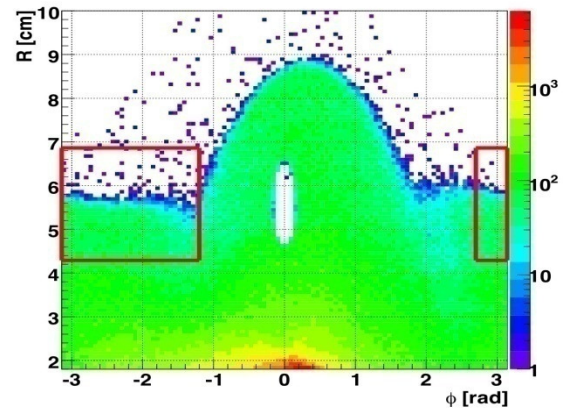


Figure 4: Hit distribution on R - ϕ coordinates. The region for calculation of ratio is shown as red line box. $-\pi < \phi < 1.2$ and $2.7 < \phi < \pi$ for $0.5R_{\max} < R < 0.8R_{\max}$.

Figure 5 shows N_0/N_{all} as a function of the vertical beam size for each horizontal beam size. It is seen that N_0/N_{all} depends on the horizontal and vertical beam sizes.

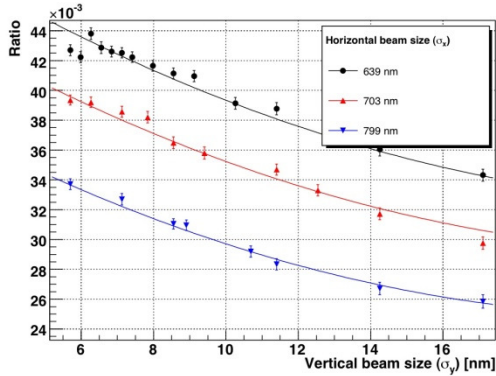


Figure 5: N_0/N_{all} vs. σ_y , where N_0 is the number of hits in the region.

The total number of hits on the pair monitor, N_{all} , reflects the luminosity which depends on the beam size as shown in Equation (1) [2]. Figure 6 shows $1/N_{all}$ as a function of the vertical beam size for several horizontal beam size. Since N_{all} becomes smaller for larger beam size, $1/N_{all}$ increases as a function of the beam sizes.

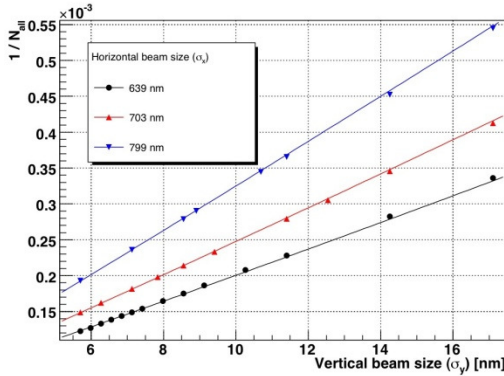


Figure 6: $1/N_{all}$ vs. σ_y . The value of $1/N_{all}$ depends on both horizontal and vertical beam size.

RECONSTRUCTION OF BEAM SIZE

To reconstruct the beam size, three measurement variables (R_{max} , N_0/N_{all} , $1/N_{all}$) were used in this analysis. The derivatives of measurement variables with respect to the beam size were obtained by fitting Figure 3, 4, and 5 with the second-order polynomials. Then, they were substituted for Equation (3) as follows,

$$\begin{pmatrix} \Delta R_{max} \\ \Delta Ratio \\ \Delta N_{all}^{-1} \end{pmatrix} = \begin{pmatrix} \frac{\partial R_{max}}{\partial \sigma_x} & \frac{\partial R_{max}}{\partial \sigma_y} \\ \frac{\partial Ratio}{\partial \sigma_x} & \frac{\partial Ratio}{\partial \sigma_y} \\ \frac{\partial N_{all}^{-1}}{\partial \sigma_x} & \frac{\partial N_{all}^{-1}}{\partial \sigma_y} \end{pmatrix} \cdot \begin{pmatrix} \Delta \sigma_x \\ \Delta \sigma_y \end{pmatrix} + \begin{pmatrix} \Delta \sigma_x \\ \Delta \sigma_y \end{pmatrix}^T \cdot (O(2)) \cdot \begin{pmatrix} \Delta \sigma_x \\ \Delta \sigma_y \end{pmatrix}. \quad (5)$$

The normalization of each measurement variable was chosen such that the measurement errors of all the variables numerically equal. Hereafter, the

beam size at the interaction point is reconstructed by the inverse matrix method. In order to improve the accuracy and stability of the procedure, we considered up to second order in Equation (4):

$$\mathbf{x} = (\mathbf{A}_1 + \mathbf{x}^T \cdot \mathbf{A}_2)^+ \cdot \Delta \mathbf{m}. \quad (6)$$

This can be solved iteratively as follows [7]:

$$(0) \mathbf{x}_0 = \mathbf{A}_1^+ \cdot \mathbf{m}$$

$$(1) \mathbf{x}_1 = [\mathbf{A}_1 + \mathbf{x}_0^T \mathbf{A}_2]^+ \cdot \mathbf{m}$$

...

$$(n) \mathbf{x}_n = [\mathbf{A}_1 + \mathbf{x}_{n-1}^T \mathbf{A}_2]^+ \cdot \mathbf{m}$$

The iteration was repeated until consecutive iterations satisfy $(x_n - x_{n-1})/x_n < 1\%$. Usually, a number of the iteration was 3 to 8.

Figure 7 and Figure 8 show the measurement accuracies of the horizontal and vertical beam size, respectively. From these results, the horizontal and vertical beam size can be measured with 2% (14 nm) and 3% (0.2 nm) accuracy, respectively. When the reconstruction was done by using only the first order term of the Taylor expansion, the accuracies of the horizontal and vertical beam sizes were considerably worse at 5% and 15%, respectively. This was because some measurement variables (N_0/N_{all} and $1/N_{all}$) cannot be fitted well with only the first polynomial functions.

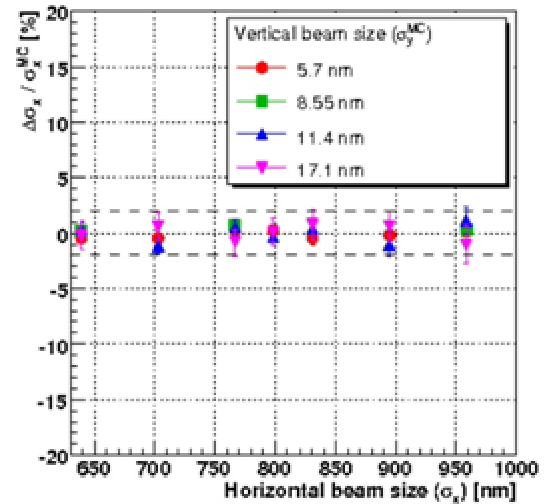


Figure 7: Measurement accuracy of the horizontal beam size (σ_x). The measurement accuracy of the horizontal beam size is 2%.

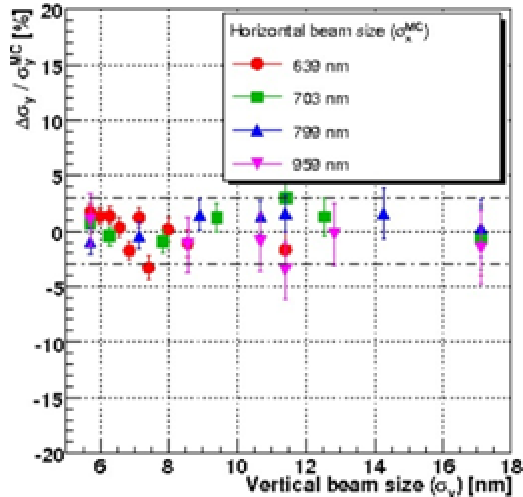


Figure 8: Measurement accuracy of the vertical beam size (σ_y). The measurement accuracy of the vertical beam size is 3%.

CONCLUSIONS

The pair monitor is the beam profile monitor for ILC and measures the beam profile at the interaction point using pair backgrounds created by the beam-strahlung.

The reconstruction of the beam size was performed using the Taylor coefficient matrix up to the second order. Three measurement variables (R_{\max} , N_0/N_{all} , $1/N_{\text{all}}$) were used in this analysis, and the matrix components were obtained by fitting with the second polynomial functions of the beam size.

The measurement accuracy of the horizontal and vertical beam size was 2% and 3%, respectively, using the second order matrix of the Taylor expansion. This result confirms that the pair monitor has enough performance to measure the beam size at IP for ILC.

REFERENCES

- [1] ILC Global Design Effort and World Wide Study, International linear collider Reference Design Report.
- [2] D. Schulte, Study of Electromagnetic and Hadronic Background in the Interaction Region of the TESLA Collider.
- [3] T. Tauchi and K. Yokoya. Nanometer Beam-Size Measurement during Collisions at Linear Colliders, KEK preprint 94-122.
- [4] CAIN web-page:
<http://lcdev.kek.jp/~yokoya/CAIN/cain235/>
- [5] T. Tauchi, K. Yokoya and P. Chen, Pair creation from beam-beam interaction in linear colliders, Particle Accelerator 41, 29 (1993).

[6] A. Stahl, Diagnostics of Colliding Bunches from Pair Production and Beam-Strahlung at the IP, LC-DET-2005-003.

[7] M. Ternick, Fast Beam Diagnostics through Beamstrahlung at TESLA.

[8] Y. Takubo, Proceedings of LCWS 2007, http://www-zeuthen.desy.de/ILC/lcws07/pdf/MDI/takubo_yosuke.pdf

[9] Jupiter web-page:

<http://acfahep.kek.jp/subg/sim/simtools/>

STUDY OF PAIR-MONITOR FOR ILD

By

Yutaro SATO

Department of Physics of Tohoku University, Sendai, Japan

The pair-monitor is the beam profile monitor at interaction point using the distribution of e^+e^- pair generated via beam-beam collisions. We plan to put the pair-monitor in front of BeamCal and study performance of the pair monitor at that position. In this paper, the radiation dose and influence of the backgrounds scattered from the BeamCal were reported.

Key words: Pair-monitor, beam profile, radiation dose

INTRODUCTION

The pair-monitor measures the beam profile at interaction point by using e^+e^- pair generated via beam-beam collisions [1, 2]. The electrons and positrons are influenced by the strong electromagnetic force of the oncoming beam. The particles with the opposite charge with respect to the oncoming beam are focused around the oncoming beam and are not scattered so much. Therefore, most of them pass in the beam pipe. However, the particles with the same charge as that of the oncoming beam are deflected with large angle. These particles carry information of the beam profile. The pair-monitor extracts the information of the beam profile by using the distribution of such largely scattered particles. The purpose of the pair-monitor is to measure the beam size with 10% accuracy. In addition, it will measure the relative displacement and transverse rotation of the two colliding beams [3].

We plan to install the pair-monitor in front of the BeamCal. In this paper, capability to use the pair monitor in that position is reported. At first, the radiation dose on the pair-monitor is shown. Then, the amount of scattered particles from the BeamCal will be discussed. Finally, the effect of the backgrounds to the beam profile measurement will be shown.

SIMULATION SETUP

In the simulation study, the simulator based on Geant4 is used and e^+e^- pairs are generated by CAIN. The standard beam size is defined as $(\sigma_x, \sigma_y, \sigma_z) = (639 \text{ nm}, 5.7 \text{ nm}, 300 \text{ }\mu\text{m})$. The solenoid magnetic field is set to 3.5 T with anti-DID [4]. The pair-monitor is located in front of the BeamCal (Figure 1). A silicon pixel sensor of 10 cm radius and 200 μm thickness is considered as a sensor candidate of the pair-monitor and two holes for the injection and extraction beam pipe were prepared

on it, whose radius is 1.0 cm and 1.8 cm, respectively.

ESTIMATION OF RADIATION DOSE

Since the pair-monitor will be put close to the beam pipe, the radiation dose on it must be considered. The maximum radiation dose in 5 x 5 mm^2 region was estimated for the pair-monitor and the BeamCal. Figure 2 shows the maximum radiation doses on the pair-monitor and BeamCal in one full year operation.



Figure 1: The simulation setup.

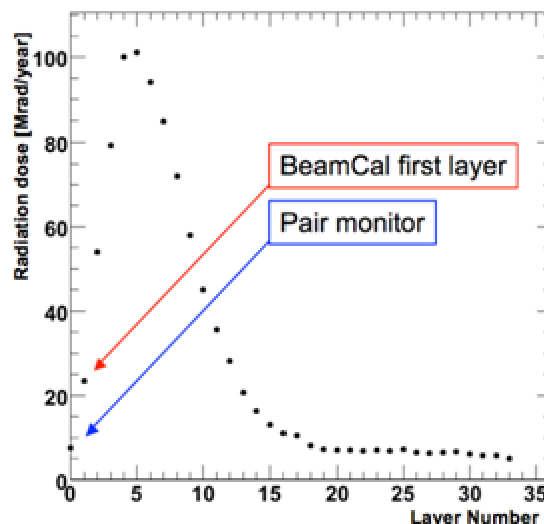


Figure 2: The maximum radiation dose in one full year operation as a function of the layer number of the BeamCal. The radiation dose of the pair-monitor is shown at the 0th layer.

The dose becomes the maximum at the fifth layer of the BeamCal. The maximum radiation dose on the pair-monitor is 7.7 Mrad/year (0.077 MGy/year). The radiation dose rapidly decreases for larger distance from the extraction beam pipe. Therefore, the maximum radiation dose can be below 1 Mrad/year for the pair monitor, adjusting the radius of the holes for the extraction beam pipe on the pair-monitor. From this reason, we can conclude that the radiation dose will not be problem for the pair-monitor.

ESTIMATION OF BACKGROUND CONTAMINATION

The electrons and positrons are scattered by the BeamCal and they will hit the pair-monitor. Such back-scattered particles might worsen the beam profile measurement by the pair monitor. Therefore, we considered inserting the CH₂-mask between the pair-monitor and the BeamCal, which is made of polyethylene.

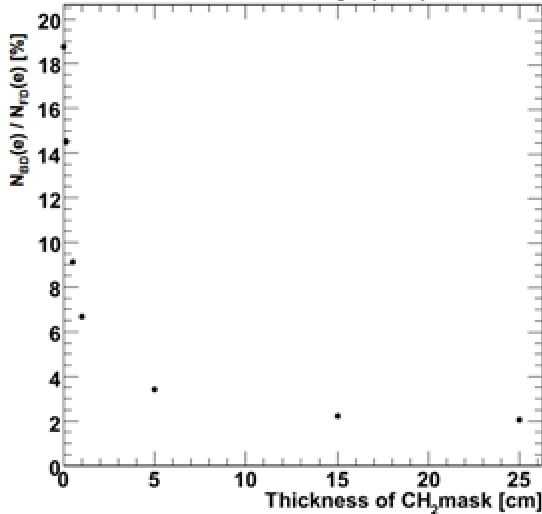


Figure 3: The ratio of $N_{BD}(e)$ to $N_{FD}(e)$ as a function of the thickness of the CH₂-mask.

In this section, the amount of the back-scattered backgrounds was investigated as a function of thickness of the CH₂-mask.

As the first step, we studied the number of electrons and positrons hitting the pair-monitor from forward ($N_{FD}(e)$) and backward directions ($N_{BD}(e)$). Figure 3 shows the ratio of $N_{BD}(e)$ to $N_{FD}(e)$ as a function of the thickness of the CH₂-mask. The contamination of the back-scattered electrons and positrons hitting on the pair-monitor will be about 20% without the CH₂-mask, and it decreases for thicker CH₂-mask. From this result, the CH₂-mask is effective to reject the electrons and positrons back-scattered from the BeamCal. The large number of gammas are created and emitted from interaction of electrons and positrons in the BeamCal. Therefore, a number of the back-scattered gammas hitting the pair-monitor ($N_{BD}(\gamma)$) was checked. Figure 4 shows the ratio of $N_{BD}(\gamma)$ to $N_{FD}(e)$ as a function of the thickness of

the CH₂-mask. $N_{BD}(\gamma)$ increases for thicker CH₂-mask since the energy of the gammas is reduced through the CH₂-mask. The lower energy gammas tend to interact more in the pair monitor with larger cross section, whereas the number of the back-scattered gammas that pass through the pair-monitor does not depend on the thickness of the CH₂-mask. The increase of gammas hitting the pair-monitor, however, is not a problem. Figure 5 shows the number of hits as a function of the energy deposit in the pair-monitor. Since the energy deposit of gammas in the pair-monitor is smaller than that of the electrons and positrons, the gammas can be removed by setting a threshold at about 35 keV. For this reason, the gammas are ignored in the following studies.

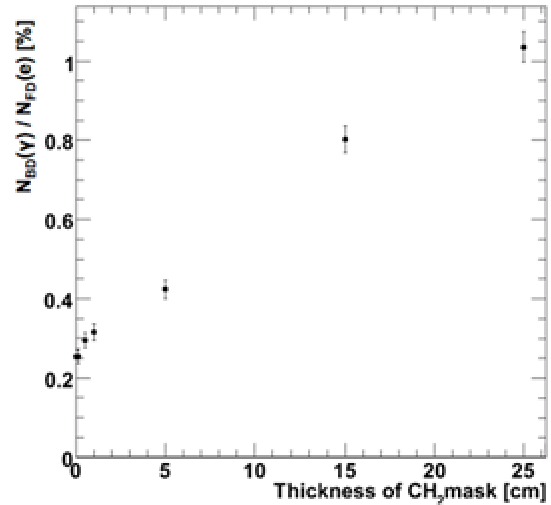


Figure 4: The ratio of $N_{BD}(\gamma)$ to $N_{FD}(e)$ as a function of the thickness of the CH₂-mask. For this plot, data corresponding to 25 bunches is used for each thickness of the CH₂-mask.

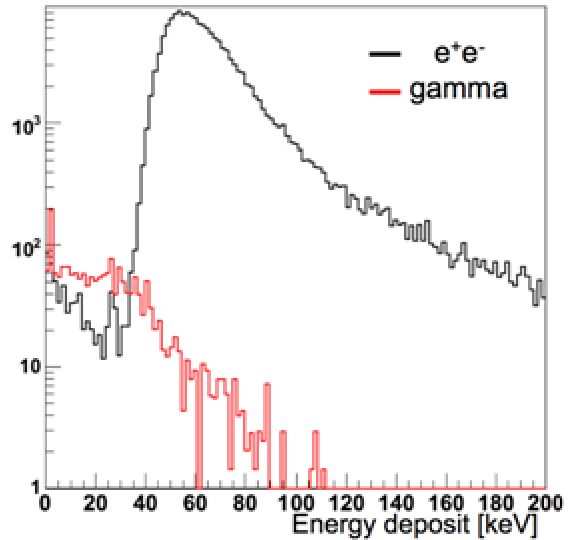


Figure 5: The number of hits as a function of the energy deposit in the pair-monitor. The black line shows electrons and positrons and the red line shows the gammas.

BACKGROUND EFFECT FOR BEAM PROFILE MEASUREMENT

In the previous section, the amount of the backgrounds from the BeamCal was discussed. In this section, influence of such backgrounds on measurement of the beam profile by the pair-monitor was studied.

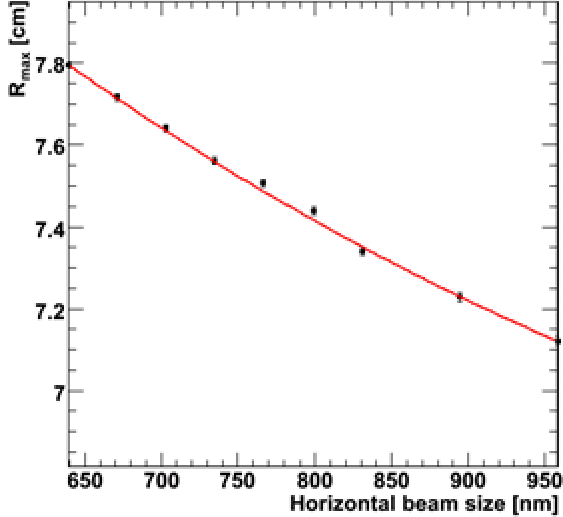


Figure 6: R_{\max} as a function of the horizontal beam size. The statistical error corresponding to 50 bunches is assigned for each point.

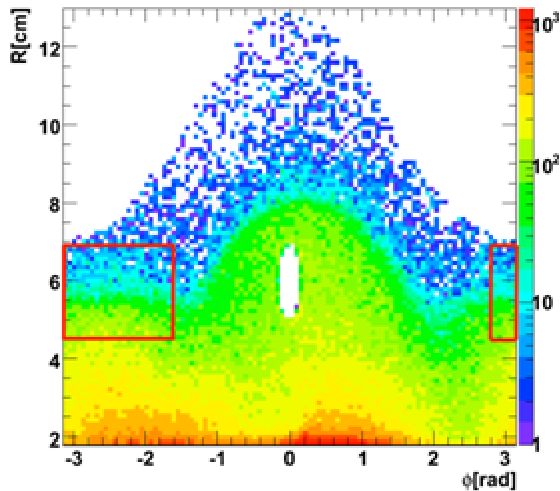


Figure 7: The e^+e^- hit distribution on the pair-monitor, where R is the radius from the center of the extraction beam pipe and ϕ is the angle around it.

There are some measurement variables to derive the information of the beam profile. R_{\max} is used for measurement of the horizontal beam size, where R_{\max} was defined as radius from the center of the extraction beam pipe to contain 99% of all the hits. Figure 6 shows R_{\max} as a function of the horizontal beam size. This figure indicates that R_{\max} depends on the horizontal beam size. The other variable is the hit density distribution on the pair-monitor, which is used to measure the vertical beam size. Figure 7 shows the e^+e^- hit distribution as a function of radius from the center of the extraction

beam pipe (R) and angle around it (ϕ). To evaluate the change of the distribution, we compared the number of the hits in the region ($\phi = -\pi \sim -1.5$ and $\phi = 3.0 \sim \pi$ for $R = 4.5 \sim 6.9$ cm) shown as red boxes in Figure 7 (N_0) and the total number of the hits (N_{all}). Figure 8 shows N_0/N_{all} as a function of the vertical beam size. It can be seen that N_0/N_{all} depends on the vertical beam size.

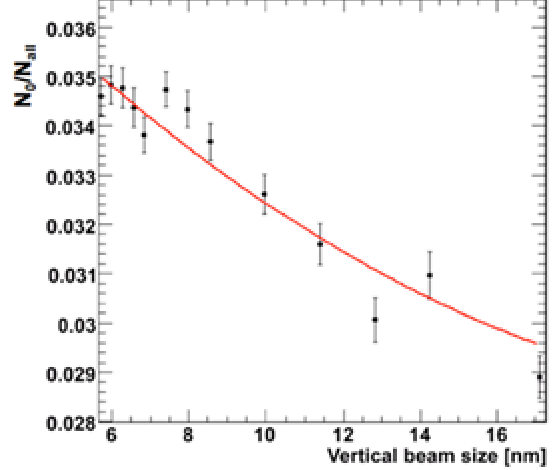


Figure 8: N_0 / N_{all} as a function of the vertical beam size. The statistical error corresponding to 50 bunches is assigned for each point.

To study influence of the backgrounds scattered from the BeamCal, distributions of R_{\max} and N_0/N_{all} were studied. As shown in previous section, CH2-mask located between the pair-monitor and the BeamCal can absorb the backgrounds effectively. Therefore, these distributions were compared with and without CH2-mask of 3 cm thickness to check the background effects.

Figure 9 shows the radial distribution for the standard beam size. From this figure, there is no significant difference in the radial distribution with and without CH2-mask. Since R_{\max} does not change in particular, the backgrounds do not have influence on measurement of the horizontal beam size.

Figure 10 shows the ϕ distributions for the standard beam size for $4.5 < R < 6.9$ cm. From this figure, no significant difference was observed in ϕ distributions with and without the CH2-mask.

Combining with the result of R_{\max} and ϕ distributions, backgrounds from the BeamCal do not have significant influence on the beam profile measurement. In addition, we can conclude that the CH2-mask will not be necessary for beam profile measurement by the pair-monitor whereas it will be important to reject the backgrounds for TPC, etc..

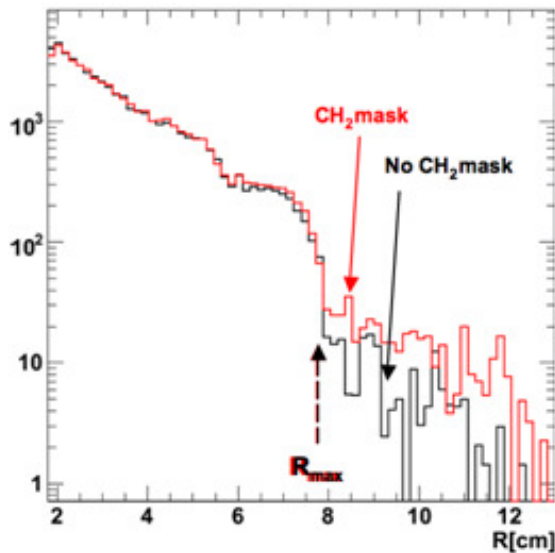


Figure 9: The hit distribution of the radius from the center of the extraction beam pipe with the CH₂-mask (red line) and without the CH₂-mask (black line). For this plot, data for 6 bunches was accumulated.

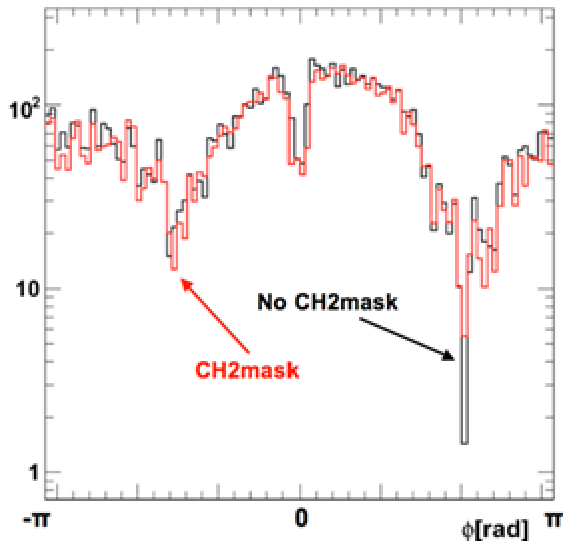


Figure 10: ϕ distributions for $4.5 < R < 6.9$ cm with the CH₂-mask (red line) and without the CH₂-mask (black line). For this plot, data for 6 bunches was accumulated.

CONCLUSIONS

We studied the installation of the pair-monitor in front of the BeamCal. The maximum radiation dose on the pair-monitor was estimated as 7.7 Mrad/year for one full year operation and it will be acceptable. The amount and effect of backgrounds scattered from BeamCal was studied. The CH₂-mask is effective to reject the background, however, it was found that the backgrounds have no significant influence on the measurement of the beam profile without the CH₂-mask.

ACKNOWLEDGEMENTS

This study is supported in part by the Creative Scientific Research Grant No. 18GS0202 of the Japan Society for Promotion of Science.

REFERENCES

- [1] T. Tauchi and K. Yokoya, Phys. Rec. E 51, 6119, 1995
- [2] GLD Detector Outline Document (<http://arxiv.org/pdf/physics/0607154>)
- [3] Y. Takubo, Proceedings of LCWS 2007 (http://www-zeuthen.desy.de/ILC/lcws07/pdf/MDI/takubo_yosuke.pdf)
- [4] ILC Global Design Effort and World Wide Study, International linear collider Reference Design Report.

BEAMCAL FRONT-END ELECTRONICS: DESIGN AND SIMULATION

By

Angel ABUSLEME, Angelo DRAGONE and Gunther HALLER

SLAC National Accelerator Laboratory, Menlo Park, CA – USA

The BeamCal specifications for rate, gain, power dissipation, resolution and occupancy set unique challenges in the front-end and readout electronics design. In order to meet the required signal-to-noise ratio, a quasi-triangular weighting function is implemented using a switched-capacitor filter and a slow reset technique. In this context, this paper describes the front-end design procedure and presents SPICE simulation results.

Key words: Front-End Electronics, Switched-Capacitor Circuits, Weighting Function

INTRODUCTION

The BeamCal detector, a calorimeter for the ILC very forward region, has two main purposes: extend the calorimeter hermeticity to small angles, and to provide a fast feedback signal for beam diagnostics and tuning. Very high occupancy is expected, so the data for all bunch crossing must be recorded (no data sparsification). The required resolution is 10 bits, and the maximum input charge is about 36 pC. Bunch crossings occur every 308 ns during almost 1 ms, followed by 199 event-free milliseconds. This cyclic operation is repeated indefinitely. The circuit must have a high sensitivity mode for sensor calibration purposes, with a gain 50x higher than that for science operation. This combination of specifications makes the front-end (FE) design an interesting challenge, because of the large input dynamic range, different modes of operation, rate and data storage.

The most important decisions in a front-end design are usually driven by noise and power consumption specifications [1]. When the input signal rate is limited, it is possible to implement a time-invariant shaper, which can be easily optimized by means of frequency-domain analyses using standard noise models. When the input signal rate is an issue, a time-variant filter is necessary, and its design requires time-domain calculations [2]. In order to have an appropriate weighting function, necessary for an adequate noise performance, correlated double sampling or slow reset techniques are used in time-variant filters.

Considering the peculiar set of specifications for the BeamCal front-end IC, an unusual approach was used to face the electronics design problem. The most important differences from previous works are: the use of g_m/I_D technique for noise analysis, the use of switched-capacitor circuits for the synthesis of an adequate weighting function to take advantage of the total time available for signal processing, and the use of digital data storage. This

paper shows the front-end design process, from a system-level perspective to circuit-level details.

THE FRONT-END SYSTEM-LEVEL DESIGN

As mentioned earlier, most decisions in FE designs involve noise, and this is also true in this IC for calibration mode. The total noise power budget was set at $2.75 \cdot Q_n^2$, where Q_n is the quantization noise of a 10-bit analog-to-digital converter (ADC). This is equivalent to an RMS noise of 0.48 LSB for the entire signal path. Considering typical noise performances for each block, the $2.75 \cdot Q_n^2$ noise budget was distributed among the signal path components; particularly, the front-end noise due to charge-sensitive amplifier (CSA) and detector was limited to $1 \cdot Q_n^2$, this is, an equivalent of about 70k electrons for science operation, and 1400 electrons for calibration mode.

In order to assess the noise behavior, with design purposes in mind, a precise noise analysis methodology was developed. The methodology is an extension of the g_m/I_D technique [3], based in the fact that all transistors of the same channel length and same current density present the same transconductance efficiency (g_m/I_D), transit frequency (f_T) and capacitances per unit length. The authors found that this methodology, consequence of simple mathematics on transistors in parallel, can also be extended to noise analysis after a simple normalization step: for all noise models considered, including all BSIM3 model equations [4], the transistor input-referred thermal and flicker noise power spectral densities, multiplied by the device current, are only dependent on g_m/I_D , the channel length and, to some extent, to the drain-to-source voltage. Once this normalization step is done, SPICE computes noise – as well as all other small-signal numbers in any transistor – using the most sophisticated models available, which are unsuitable for simple hand analysis; the results, stored in lookup tables and charts, are adequate for design purposes.

Preliminary noise estimations using the methodology mentioned before helped to find an adequate architecture for the IC. A CSA is the front-end spear, connected to the detector through a coupling capacitor. A 0.8-pF feedback capacitor, used for calibration mode, is permanently connected to the charge amplifier, and a 35.2-pF capacitor is added in parallel for science operation. The CSA closed-loop frequency response acts as a first barrier against noise.

Baseline restoration in 308 ns is best achieved if active, gated reset is used on the CSA; therefore, a time-variant front-end is being considered. For this kind of systems, when properly designed, noise is mostly determined by the front-end weighting function. In this case, the g_m/I_D methodology was used to extract information on thermal and flicker noise coefficients for the most relevant transistors in terms of noise; this information was used in design scripts to obtain an adequate front-end. As a result, the CSA input device current was set at 350 μA , and its g_m/I_D at 17mS/mA.

For science operation, it was found that the expected CSA closed-loop bandwidth suffices for reducing the thermal noise to negligible values, whereas the reset action limits the flicker noise components.

For calibration operation, the weighting function must be carefully tailored in order to maintain noise within adequate values. In fact, for the noise coefficients implied by the CSA design, a perfectly triangular weighting function yields about 700 electrons (RMS) of noise – mainly due to series noise, considering the short processing time – and any departure from an isosceles triangle implies more noise, mainly depending upon the weighting function slope.

In this gated-reset system, the weighting function has two slopes: one due to the direct filter action on the input signal (filter slope), and the other due to the reset action (reset slope). In general, the ideal filter slope for a triangular weighting function can be accomplished by using a perfect integrator with an adequate gain, and the reset slope can be synthesized by means of correlated double sampling (CDS). Considering process-voltage-temperature (PVT) variations of current IC technologies, trapezoidal weighting functions [5] represent a more practical solution, as the weighting function slopes cannot be precisely defined when they depend on high tolerance constants such as RC or g_m/C .

In this chip, the short interval between events implies very limited integration time, and therefore, high sensitivity to series noise components. In order to take advantage of the entire time interval, precision switched capacitor (SC) circuits will be used.

Switched capacitor circuits [6] are sampled data, analog circuits; although the output variable is a continuous voltage, it is only valid in discrete

times. As sampling operation is involved, an anti-alias filter is necessary to attenuate out-of-band signals. In SC circuits, resistors are simulated using switched capacitors; therefore, time constants and gains are defined by the ratio of two capacitors and are considerably less sensitive to PVT variations than as RC or g_m/C techniques.

For an adequate synthesis of the weighting function, the filter slope will be defined by the action of a SC integrator; in this case, the CSA closed-loop dominant pole provides the adequate anti-alias filtering action.

The reset slope requires a more careful approach. The CDS technique basically mirrors the filter slope into the reset slope; however, requires additional circuitry to subtract the signal sampled at two different moments. A different approach, based on slowing down the CSA reset action, can be used instead. Specifically, the reset action is engaged as quickly as possible, to allow the CSA to *forget* whatever signal was measured in the previous period; after that, the reset action is slowly released, in order to mitigate the effect of a split doublet. This effectively limits the weighting function's reset slope and also reduces the effect of charge injection, inherent of any MOSFET switch.

In order to achieve a controlled reset-release action, a SC network was designed to gradually reduce the gate-to-source voltage of the reset switch. In other words, the switch transistor's V_{gs} is held by a capacitor during the reset time, and then discharged through a SC resistance during the reset release time. Although this slow reset action produces a weighting function slope far from ideal, it is sufficient for noise filtering.

The switching frequency in a SC circuit is a critical decision in the circuit design. A low switching frequency implies more aliasing and possibly more noise if the anti-alias filter is not well designed; on the other hand, a higher switching frequency requires a faster, power hungry amplifier. A good tradeoff in this design is achieved if the whole period between bunches is sampled a total of 16 times, implying a switching frequency close to 52 MHz. This means 8 periods for integration and 8 periods for reset.

Based on previous considerations, a simplified block diagram for the IC front-end is presented in Fig. 1, where two different signal paths can be found. In normal operation, the ADC reads the voltage directly from the CSA output (lower path), whereas in calibration mode, the switched capacitor integrator is used for filtering purposes (upper path). In this mode, a buffer is required in order to desensitize the CSA operation to large surge currents required by the switched capacitor integrator. In both modes of operation, a slow reset action is implemented for an adequate weighting function. The weighting functions expected from this front-end, considering ideal components, are shown in Figs. 2 and 3.

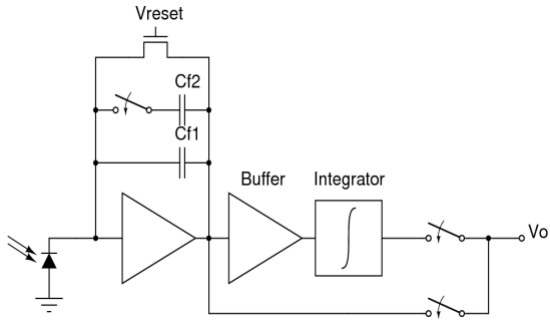


Figure 1. Simplified front-end block diagram, single channel.

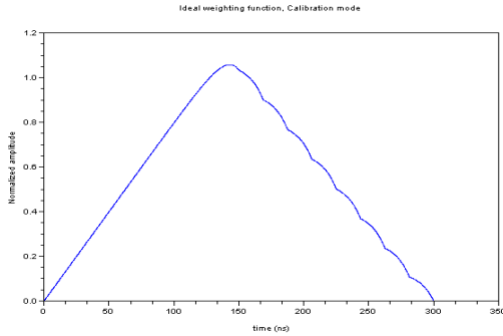


Figure 2. FE weighting function assuming ideal components, calibration mode.

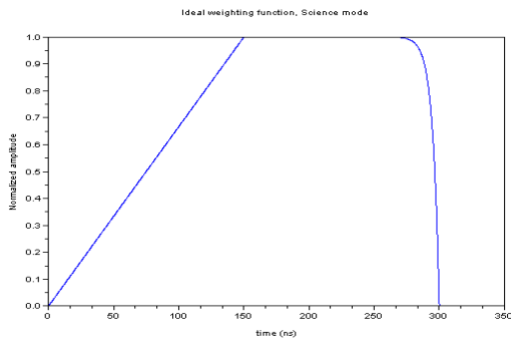


Figure 3. FE weighting function assuming ideal components, science mode.

FRONT-END CIRCUIT IMPLEMENTATION

The circuit presented in previous section consists of a CSA with a built-in slow reset action, a buffer and a switched-capacitor integrator. This section shows the details of each circuit. For PSR and crosstalk considerations, a pseudo-differential architecture is considered in the CSA, followed by fully-differential circuits.

1) Charge-Sensitive Amplifier

A single-ended, folded-cascode topology was chosen due to performance, simplicity and noise considerations (Fig. 4). The polarity is based on NMOS amplifying device (M1), arbitrarily assuming that the detector will consist of common-anode photodiodes; if in the final detector the photodiodes share the cathode terminal instead, the

polarity of the CSA will be updated accordingly in following revisions.

In this topology, when properly designed, the main noise contributors are the input and folding transistors (M1 and M4); in fact, both appear in parallel in noise analyses. As mentioned earlier, from noise and performance considerations, the input transistor current was set at $350 \mu\text{A}$, and its g_m/I_D at 17mS/mA . Higher transconductance efficiency leads to a more power efficient design; however, it would considerably degrade the slew rate performance in the case of science operation, where the total feedback capacitance is 36 pF .

The amplifier's simulated static gain is 82.6dB , and its open-loop bandwidth is 303 kHz ; its input capacitance is 1.1 pF and its output range, arbitrarily defined as the output voltage for less than 40% decrease in static gain, is between 0.22 V and 1.28 V .

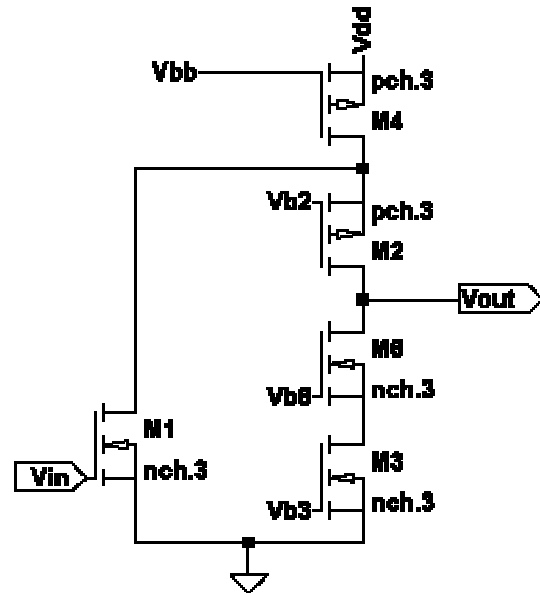


Figure 4. Charge amplifier schematic.

A 0.8-pF feedback capacitor ($Cf1$) is permanently connected to the CSA; the 35.2-pF feedback capacitor for science operation ($Cf2$) is switched in and out by means of an NMOS switch, appropriately sized so that the parasitic zero associated with it is far from the CSA closed-loop bandwidth.

The reset switches are sized to allow a fast reset action. As explained earlier, the gate-to-source voltages in these switches are gradually decreased to achieve the slow reset action, by means of the switched capacitor network shown in Fig. 5. The operation of this network requires a two-phase, non-overlapping clock. During ϕ_1 , C3 shares its initial charge with C4, reducing its voltage by 15%; during ϕ_2 , the charge in C4 is reset, allowing the cycle to start again.

In order to increase the CSA output range in calibration mode, where its behavior is most sensitive to the open loop gain, the CSA output

voltage must remain within the operational output range. A precharge circuit will be used to achieve this purpose, taking advantage of the circuits necessary for electronics calibration (not shown in this paper). The precharge circuit shifts the CSA reset voltage from the NMOS threshold voltage V_t (approximately 0.5V) down to 0.25V, allowing an output swing of 1V out of a 1.8-V supply.

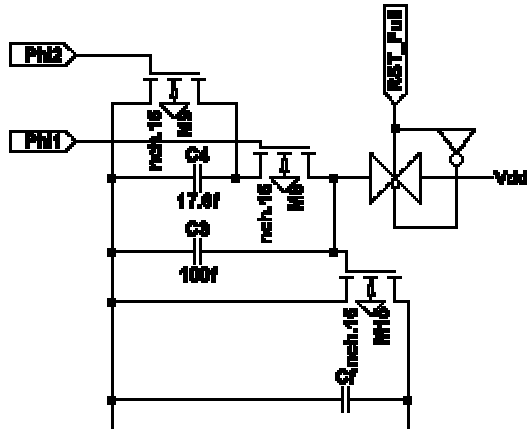


Figure 5. CSA reset circuitry.

2) Buffer

The buffer must replicate the CSA output and desensitize its operation to the rapidly changing capacitive load placed by the switched-capacitor integrator. A practical solution can be found in a source follower (Fig. 6). In this circuit, two important problems must be solved: linearity and input range.

To improve linearity, a PMOS device with body and source tied together (M1) will be used; this configuration is roughly insensitive to body effect. To reduce the current variations that affect linearity, a cascoded current source (M2, M5) is used; to reduce the variations in V_{ds} , a bootstrapping technique [7] is implemented (M3).

The input range of an ideal PMOS-based source follower is between 0 V (actually, less than that if negative voltages are allowed) and $V_{dd} - |V_t|$, approximately 1.3 V in this technology. However, linearity is considerably degraded when operating near the upper limit, thus the performance would benefit from voltage levels lower than those provided by the charge amplifier, even considering precharge. In order to achieve this, a switched

capacitor voltage shifting network is implemented ($C1 +$ transmission gates). The network is controlled by two non-overlapping clock signals, RST and RST_b.

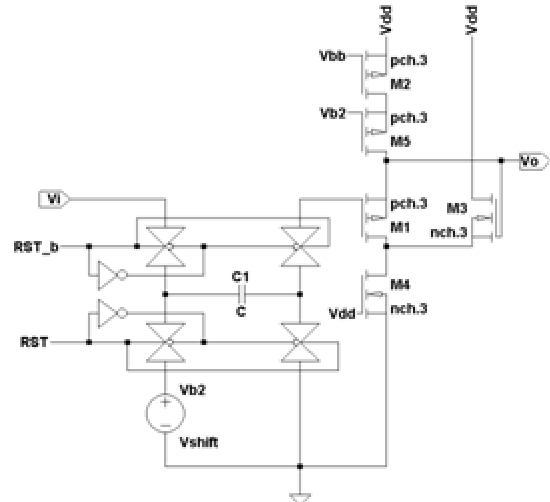


Figure 6. Simplified buffer schematic.

3) Switched-Capacitor Integrator

A simple, fully differential switched-capacitor integrator based on a forward-Euler integration (FEI) algorithm was implemented [6] (Fig. 7). This circuit was preferred over the backward-Euler integration (BEI) due to the fact that represents a lighter load for the driving network.

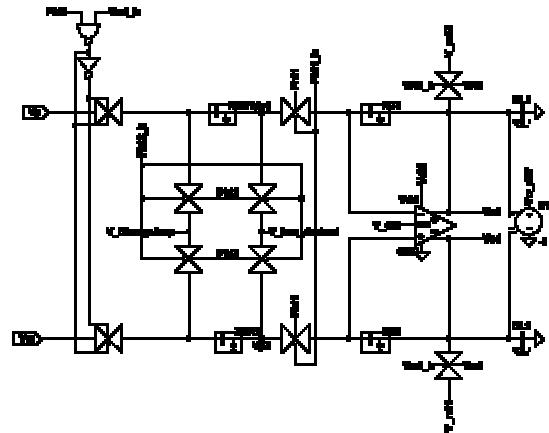


Figure 7. Switched-capacitor integrator schematic.

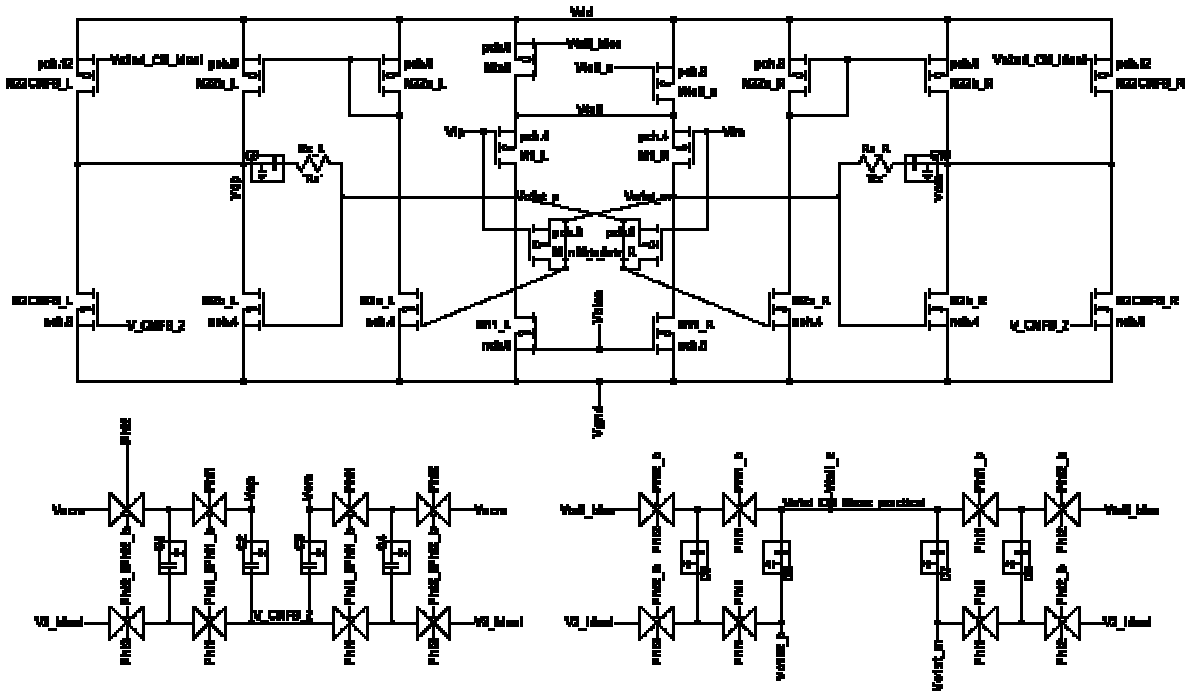


Figure 8. Integrator OTA schematic.

Noise in the integrator comes from two main sources: KT/C noise of all switched capacitors, and amplifier voltage noise. The noise budget allocated for each of these components is $Q_n^2/4$. This figure, along with the switching frequency, sets the lower limit for the integrator capacitor values: 600fF for the feedback capacitors (XC1, XC2), and 150fF for the series, switched capacitors (XCR1, XCR2).

The integrator core is a fully differential, two-stage operational transconductance amplifier (OTA), based in the class A/AB topology presented by Rabbii *et al.* [8] (Fig. 8). Class AB output was chosen for power efficiency considerations and the necessity to drive the integrator and load capacitors. For speed vs. power consumption considerations, the second stage is based on NMOS amplifying devices (M2a_R, M2b_R, M2a_L and M2b_L); for adequate common mode range in the internal nodes, the input stage is based on PMOS devices (M1_R and M1_L). At the input, the reset voltages are appropriately set to allow the PMOS input stage to cope with the buffer output voltage levels. Compensation scheme is based on a Miller approach (C9 and C10) with nulling resistor (RZ_R and RZ_L). Class AB output is achieved in a push-pull configuration (M2b_R + M22b_R and M2b_L + M22b_L), and the second stage's quiescent current is set by the first stage output common mode. Each stage requires a common mode feedback network, and both are implemented using switched capacitor circuits, shown at the bottom of the schematic.

SPICE SIMULATIONS

Fig. 9 shows the CSA open loop frequency response, and Fig. 10 presents the front-end output waveforms for calibration mode, for input signals of different amplitudes. Fig. 11 and 12 show the obtained weighting functions for calibration and science modes, respectively.

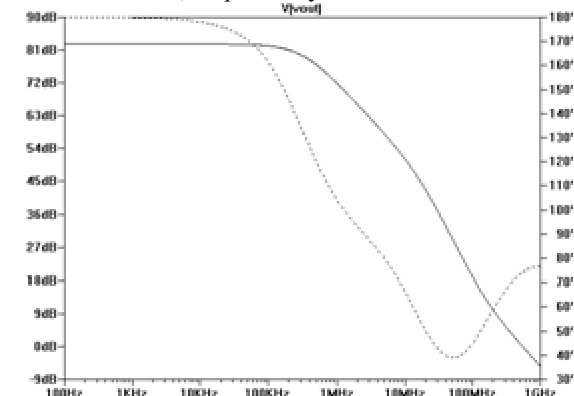


Figure 9. CSA frequency response in magnitude (solid line) and phase (dashed line).

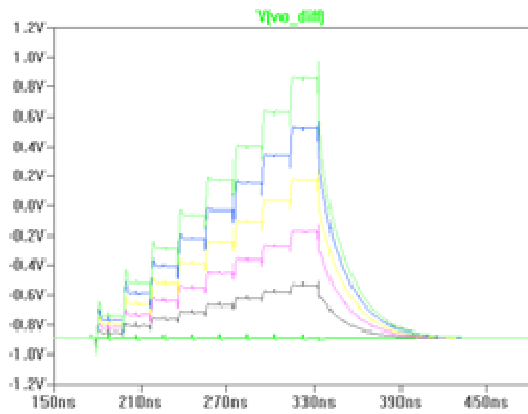


Figure 10. Front-end output waveforms for calibration operation.

Front-end noise computations due to charge amplifier noise yield 6166 electrons for science operation and 1163 electrons for calibration, both below the specified noise budget.

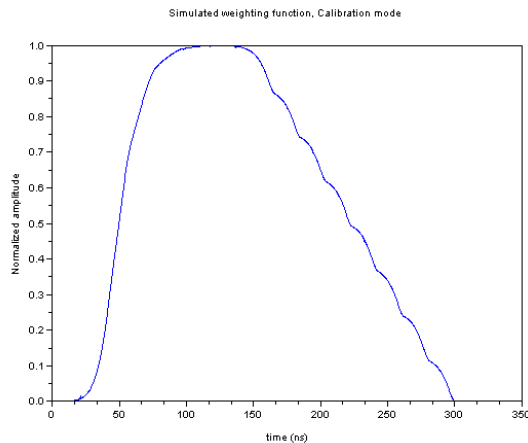


Figure 11. Simulated weighting function for calibration mode.

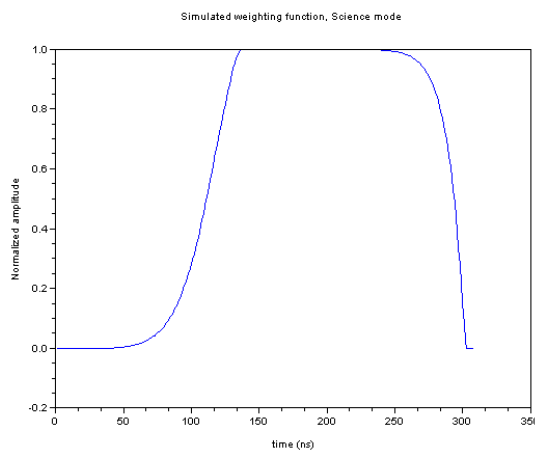


Figure 12. Simulated weighting function for science mode.

CONCLUSION

The circuit-level design process of the BeamCal instrumentation IC's front-end has been presented. A time-variant pulse shaping approach is considered, and the weighting functions are defined

using precision switched-capacitor circuits. The time constants involved in the weighting functions are precisely defined, allowing using the complete 308 ns period for signal processing. The additional noise introduced by the finite switching frequency has been assessed and is tolerable in this application.

ACKNOWLEDGEMENTS

The authors would like to thank Professors Bruce Wooley, Boris Murmann and Martin Breidenbach, and Dr. Dietrich Freytag, for their valuable participation in this research.

REFERENCES

- [1] Spieler, H. *Semiconductor Detector Systems*. Oxford University Press, 2005.
- [2] Goulding, F. S. *Pulse-shaping in low-noise nuclear amplifiers: A physical approach to noise analysis*. Nuclear Instruments and Methods, 100:493–504, 1972.
- [3] Silveira, F. et al. *A g_m/i_D based methodology for the design of CMOS analog circuits and its application to the synthesis of a silicon-on-insulator micropower OTA*. Solid-State Circuits, IEEE Journal of, 31(9):1314–1319, 1996.
- [4] Liu, W. et al. *BSIM3v3.3 MOSFET Model, User's Manual*. Department of Electrical Engineering and Computer Sciences, University of California, Berkeley, CA 94720, 2005.
- [5] Radeka, V. *Trapezoidal Filtering of Signals from Large Germanium Detectors at High Rates*. Nuclear Instruments and Methods, 99:525–539, 1972.
- [6] Gregorian, R. et al., *Switched-Capacitor Circuit Design*, Proceedings of the IEEE, Vol. 71, No. 8, August 1983.
- [7] Razavi, B. *Design of Sample-and-Hold Amplifiers for High-Speed Low-Voltage A/D Converters*. IEEE Custom Integrated Circuits Conference, 1997.
- [8] Rabii, S. *Design of Low-Voltage Low-Power Sigma-Delta Modulators*. Ph.D. Dissertation, Stanford University, 1998.

Conclusion

CONCLUSIONS OF THE WORKSHOP ON FORWARD CALORIMETRY AT THE ILC

By

Wolfgang LOHMANN

DESY, Platanenalle 6, D-15738 Zeuthen

At the beginning of the workshop we heard about the ambitious research program of the Vinča institute, and about the challenges and promises of the physics we expect on the Terascale. During the workshop excellent talks were given on progress in the R&D for FCAL, but also on related topics as the very forward detectors at ATLAS and CMS. First results on design studies of the very forward region of a CLIC detector were presented, and we got an excellent overview about the challenges in physics and for the detector at super-Belle. A distinguished theorist educated us on the role of the Higgs boson mass in a variational approach to QFT.

PROGRESS IN SIMULATIONS

New results were obtained for a robust selection of Bhabha events, based on a given performance of the LumiCal, and on the critical sources of systematics. Also, the expected background from two-photon processes, was treated more in detail.

A new topic was the design of the beam-pipe and a comparison of two basic variants with respect to the performance of the luminosity measurement.

The potential of the pair monitor for beam parameter determination was studied in more detail, demonstrating that a second order Taylor expansion improves the accuracies of beam parameter measurements.

These studies should be finished soon and the results written down to be considered in the LoI preparations.

MECHANICAL DESIGN AND INTEGRATION IN ILC DETECTORS

A big step forward has been made in the mechanical design of BeamCal and LumiCal. Also the installation schemes and the integration into the ILD detector are much more mature now. These results improve our situation to contribute to the LoI. For the EDR, however, things like temperature stabilization, position control, power and signal cabling need more detailed considerations. A crucial role will be played by the laser position monitoring system. A small prototype is available which demonstrates the feasibility for part of the topic. In future, we have to identify the critical issues and start to think about prototyping.

SENSOR R&D

A first design of the sensors for a LumiCal prototype is ready, the Hamamatsu company has been chosen for prototype production, and we solved the funding problem. Before the end of the year the first prototypes will arrive in the laboratories, and a intense test program will start.

For BeamCal new prototypes of GaAs sensors with improved expected radiation hardness are delivered in time and the test in the laboratory are completed. Irradiation tests in the beam are planned in December.

In addition, two additional sensor materials, quartz and sapphire single crystals, are investigated. Signals from ionising particles are seen, however of very small size. The studies will be continued with single crystals of higher purity.

New results for diamond sensors demonstrated the improved understanding of their features.

FE ELECTRONICS

Impressing activity is ongoing for front-end electronics developments for BeamCal, LumiCal and the pair monitor. For LumiCal and the pair monitor prototypes are under test and second submissions with extended functionality are done. For BeamCal detailed design optimizations are ongoing and we expect prototypes next year.

THE NEXT STEPS

FCAL is invited to contribute to the LoI for the ILD detector. I also expect that our American colleagues will work on the very forward design of SiD. The deadline for the LoIs is March 31 2009. In order to prepare the part of the very forward instrumentation working groups should be formed who work out a text about key issues of the very forward instrumentation to be integrated then in a full write up. These working group should start the work soon and deliver a draft end of 2008.

The following working groups were agreed:

- Mechanics and integration: Wojtek, Sergey
- Design optimisation: Iftach, Eliza, Ivan, Ito-san
- Sensors and FE electronics: Wolfgang Lange, Marek, Hans, Takubo-san, Wojtek

The draft texts are supposed to summarize the 'state-of-the' art of the field, and also identify the critical points where further R&D is needed up to 2012, to prepare the EDR.

The prototype sensors will need studies in test-beam. For irradiation tests we will have a test-beam venture end of the year at DALINAC at the TU Darmstadt. For the future we should agree on a test-beam schedule at the DESY test-beam with single electrons of about 5 GeV. Furthermore, after the sensor tests have shown satisfactory performance, the construction and test of a prototype of a sensor plane prototype fully equipped with FE Asics will be the next major step. The anticipated date is 2012.

The laser position monitoring system has demonstrated very good performance at small distances. What is missing are solutions for the control of the inner acceptance radius and the large-distance position monitoring for two LumiCal calorimeters of about 6 m away.

Provided no major difficulties will arise for the funding we agreed to plan prototypes of the calorimeters ready in 2014.

Taking into account that the time schedule of a linear collider is at the moment rather uncertain, attempts to apply the expertise acquired with in FCAL at a mid-term timescale are reasonable. The DESY group contributes to the Beam Condition Monitor of the CMS experiment. As reported here, single crystal diamonds with a fast and radiation hard FE electronics and an optical transmission line are used to measure the beam halo close to the interaction point. This engagement will considerably improve our expertise in long term operation of diamond sensors in a harsh radiation environment.

Super Belle offers the possibility to use sensors developed for LumiCal to instrument the forward regions of the detector. Since Cracow IFJPAN and Tohoku University are members of the Belle collaboration these groups should decide to which extend they want to use this chance.

The activities to design a CLIC detector will be enhanced in the near future. Obvious mid-term contributions from FCAL may be Monte Carlo studies to the luminosity measurement and to radiation loads near the forward region. However, we rely also on personnel support from CLIC.

ACKNOWLEDGEMENTS

At the very end I would like, on behalf of all participants, thank Ivanka, Mila, Snežana, Ivan and all others having been involved in the organisation of the workshop for their excellent work. It was a pleasure to be here, to work under excellent conditions in the Vinča Institute, to enjoy the walk through Belgrade, and, last but not least, the tasty dinners.